RF Cavity Tuning Based on Reflected Power Measurements

by

Ramona Leewe

Dipl. Ing., University of Applied Science Bochum, 2010

Dissertation Submitted in Partial Fulfillment of the
Requirements for the Degree of
Doctor of Philosophy

in the
School of Mechatronic Systems Engineering
Faculty of Applied Science

SIMON FRASER UNIVERSITY
Spring 2017

Approval

Name:	**Ramona Leewe**
Degree:	**Doctor of Philosophy (Applied Science)**
Title:	***RF Cavity Tuning Based on Reflected Power Measurements***
Examining Committee:	**Chair:** Siamak Arzanpour Professor

Mehrdad Moallem
Senior Supervisor
Professor

Ken Fong
Supervisor
Group leader RF Controls
TRIUMF

Ed Park
Supervisor
Professor

Krishna Vijayaraghavan
University Examiner
AssitantProfessor

Ken McIsaac
External Examiner
Associate Professor
Western University

Date Defended: 3 March 2017

Abstract

RF cavities are resonators and the key structures in particle accelerators. An electromagnetic field within the cavities provides the acceleration field. Within linear particle accelerators, particle bunches travel along a beam pipe and through the aligned cavities. A positive electric field along the beam line results in an acceleration *kick* of the particle bunch. The speed of the traveling particle bunches is synchronized with the RF field within the cavities. Hence, tuning of the natural resonance frequency of an RF cavity is essential for accelerator structures to achieve efficient beam acceleration and to reduce power requirements. Operational cavities are typically tuned using phase comparison techniques. Phase measurement is subject to temperature drifts which renders this technique labor and time intensive.

In this thesis, we developed two novel resonance frequency tuning schemes solely depending on the reflected power component of a cavity. The base for control scheme development is a mathematical model of the cavity in terms of the steady state signals. The first control scheme was derived through a Lyapunov analysis and incorporates a gradient estimator of the performance function. The second control scheme is based on sliding mode extremum seeking. Both systems are analyzed in terms of the stability; conditions are provided which guarantee stable system behavior up to twice the cavity bandwidth. A simulation study verifies the derived stability conditions.

An experimental test bench, including a room temperature quarter wave cavity, was built to test the control schemes under various conditions. Although both control schemes show similar tuning results, a higher tuning accuracy is obtained by the sliding mode based control scheme. Hence, the latter was chosen to be implemented on two resonators (DTL tanks) of TRIUMF's ISAC I facility. The system was fully commissioned on both DTL tanks and has been in operation since April 2016. Reflected power, forward power, and tuning position are monitored and analyzed. Long term measurements showed the influence of environmental temperature variations. As the influence of environmental temperature variations can be neglected for reflected power measurements, the reflected power based tuning system provides a higher tuning accuracy compared to the traditional phase based tuning system. The start-up time and the need for human oversight are reduced significantly.

Keywords: RF cavity tuning; extremum seeking; gradient estimation; sliding mode extremum seeking

Dedication

To my always supportive partner Hendrik

Acknowledgements

First and foremost I would like to express my special appreciation and thanks to my advisors Professor Mehrdad Moallem and Dr. Ken Fong, who both have been tremendous mentors for me. I thank both of you for the continuous support of my Ph.D study and related research, for your patience, motivation, and immense knowledge. Your guidance helped me in all the time of research and writing of this thesis.

Then I want to thank my colleagues and friends Glen and Bob who always supported me, especially in the experimental phase of this work. You were always there for me, and helped me out with your knowledge and skills whenever I needed you.

I gratefully acknowledge the funding received towards my Ph.D from TRIUMF, that made my Ph.D work possible.

Last but not least, I want to thank my friends and family. The last 6 years were not always easy and you supported and encouraged me through the entire time, and lived all the high's and low's with me. Thank you.

Table of Contents

List of Tables

List of Figures

Chapter 1

Introduction

1.1 Motivation of the Research

Particle accelerators play an important role in modern physics. Radio frequency (RF) cavities are used in many particle accelerator facilities to accelerate particle beams through an electromagnetic field [1]. Beams of high energy are useful for fundamental and applied research. To achieve efficient beam acceleration in order to obtain a high energy beam, and to reduce power requirements, the RF cavities need to be tuned such that the resonance frequencies are equal to their excitation or operating frequency [1]. The quality of an accelerated beam is directly dependent on the stability of the amplitude and phase of the field developed within the cavity. Various methods can be used to regulate the tune of the cavity. To date, however, all cavity tuning methods in operation measure the input and output phases of the cavity and use this information to adjust the resonance frequency by changing the geometry of the cavity [2].

The phase lag is the difference between the input and the output phase of the cavity. It is then compared to a phase setpoint. The error between the setpoint and the phase lag is then used as controller input. It can be approximated by a linear function in the range of the cavity bandwidth, allowing the use of classical control theory to tune the resonance frequency. As the measured phase lag is only an approximately linear function when the frequency deviation (between operating and resonance frequency) is within the cavity bandwidth, the controllable bandwidth is limited to the cavity bandwidth. However, the high frequency nature of the phase and necessary long coaxial cables or wave guides to transfer the signal to the control station lead to phase drifts caused by environmental temperature changes [3]. As the phase setpoint is fixed, the environmental temperature induced phase measurement drift further leads to an error with respect to the fixed phase setpoint. The temperature change induced error between the measured phase lag and the setpoint causes power reflections. To maintain a constant acceleration field within the cavity, the input power has to be increased to compensate for the reflections, thus, leading to ineffective power consumption. Moreover, phase measurement drifts outside the controllable bandwidth yield frequent manual phase set point adjustments.

Another drawback of this method related to the temperature dependence of the phase is the cavity start-up. Each cavity is started up by coupling a small amount of RF power into the cavity. The temperature of the cavity changes with the amount of power coupled into it. Consequently, the phase set point changes. During the start-up of each cavity the phase set point has to be adjusted to maximize the field within the cavity using a phase shifter. Hence, to reach the desired acceleration field within the cavity, the input power has to be slowly increased while the phase set point is tracked manually. In case of an *ideal* cavity, manual phase set point adjustments are required over tens of minutes. Yet, most cavities are not ideal; the performance of each cavity is influence by the cavity material and its impurities, the vacuum within the cavity or the performance of the coupler transferring the power to the cavity. Depending on the cavity characteristics, the phase set point adjustments can be required over a couple hours of operation until the temperature has settled and does not change anymore. For facilities with many cavities, the human oversight required to start all cavities is immense. For reference, TRIUMF's ISAC I section includes 14 room temperature resonators.

Due to these difficulties regarding phase measurement, it is highly desirable to eliminate the phase measurement all together. The reflected power of the cavity represents the frequency detuning as well [4]. The rectified signal of the cavity, reflected voltage or power, represents an extremum function with a minimum when operating and resonance frequency match. Regarding the phase measurement based tuning system, the measurement inaccuracy is caused by the comparison of the measured phase lag to a fixed setpoint. As the reflected power component of the cavity does not have to be compared to a fixed setpoint, the environmental temperature variation induced measurement error does not affect the tuning accuracy. Hence, a resonance frequency tuning system based on reflected power measurements reduces the power requirements as well as the human oversight significantly.

1.2 Background and Present State of Technology

1.2.1 TRIUMF and the ISAC I Facility

TRIUMF produces negatively charged hydrogen ions (H^-) from an ion source. The heart of the TRIUMF facility is the 1MW, 500MeV cyclotron, which is the first stage of particle acceleration. The cyclotron is a special type of particle accelerator which accelerates particles following a spiral and obtains a particle speed of 0.7 times the speed of light. A high energy H^+ beam is produced by stripping the H^- ions inside the cyclotron. Downstream of the cyclotron is the ISAC (Isotope Separation and ACceleration) facility. It is a linear particle accelerator and is separated into the two parts ISAC-I and ISAC-II, with ISAC-II being the superconducting extension of ISAC-I [5]. The continuous wave (CW) proton beam from the cyclotron is steered towards a target to produce radioactive isotopes. The heavy ion isotope beam is transported in the low-energy beam transport (LEBT) electrostatic beam line and sent via a switchyard to either the low-energy experimental area or to a series of room-temperature accelerating structures, the ISAC-I medium-energy beam transport (MEPT) section. Figure 1.1 shows a drawing of the ISAC-I facility.

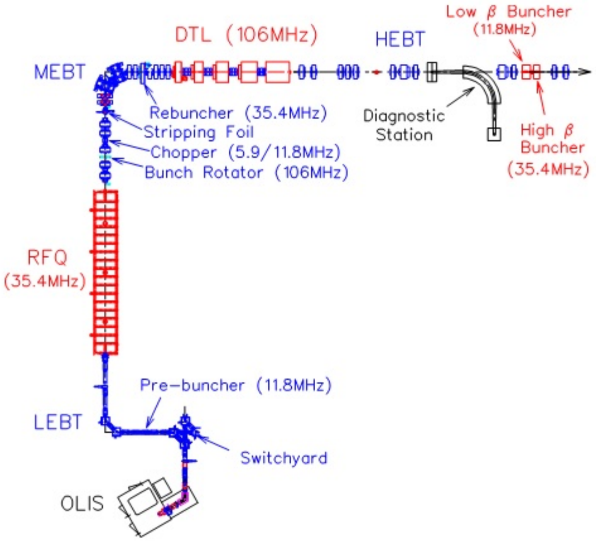

Figure 1.1: Drawing of the ISAC I room temperature linear accelerator.

The beam transport and acceleration after LEBT switches from static to an alternating field within the cavities to achieve higher acceleration field gradients. Due to the alternating field in a high frequency accelerator only particle packages can be accelerated; these are called bunches. Before reaching the first accelerating structure the particles pass the pre-buncher. The conversion of the continuous beam into a bunched beam is done by two buncher cavities in series. After the pre-buncher the beam is bunched at 11.78 MHz, which is the third subharmonic of the following RFQ with a resonant frequency of 35.36MHz. The 30kW RFQ is the first acceleration structure [6]. This structure is composed of 4 electrodes which are symmetrically located around the beam axis while adjacent electrodes have a reversed polarity. This creates an electric quadrupole. The charged ions within the quadrupole field are drawn to the center of the quadrupole due to the alternating reversal of polarity. Other than focusing the beam, the RFQ also accelerates the particles by a sine modulation of the electrodes to generate an electric field in the direction needed for beam acceleration.

The next assembly after the RFQ is the bunch rotator whose function is similar to the function of the pre-buncher. Due to the fact that a bunched beam is necessary for RF acceleration, the beam is compressed. The high quantity of equally charged particles, caused by bunching compression, leads to beam bunch expansion in all directions. To counteract this effect, the beam is focused with an external magnetic field and the expansion in beam direction is suppressed by the buncher.

The following component after the buncher is a chopper (see Figure 2.1). This chopper is a dual frequency chopper and provides operation in two distinct modes. The general function of a chopper is to reduce beam losses as well as providing varying period bunch gaps realized by two different operation modes.

After the re-buncher, the next acceleration structure is a Drift Tube Linear (DTL) accelerator. It is a resonator structure that operates at 106.08 MHz and is divided into different modules. The DTL consists of 5 acceleration modules operating with an input power range of 10kW to 50kW, and 3 bunchers. The different modules operate independent from each other and allow separate functions of the DTL [7]. After the DTL the beam reaches the high energy beam transport (HEBT) section and is further delivered to the ISAC-II superconducting linear accelerator.

1.2.2 RF Cavity

A resonant cavity is a volume (vacuum to prevent beam loss) contained by metal conducting walls; usually copper for room temperature cavities. RF cavities come in many shapes and sizes characterized by the characteristic velocity, RF frequency, effective voltage, number of cells or gaps, or material. RF power of appropriate frequency (in resonance with the cavity geometry) is fed to the cavity and generates an electromagnetic field. The amplitude of the electromagnetic field grows similar to any driven but damped harmonic oscillator; damping comes from the resistance in the cavity walls. The drawing and photograph in Figure 1.2 show an example of a room temperature quarter wave cavity.

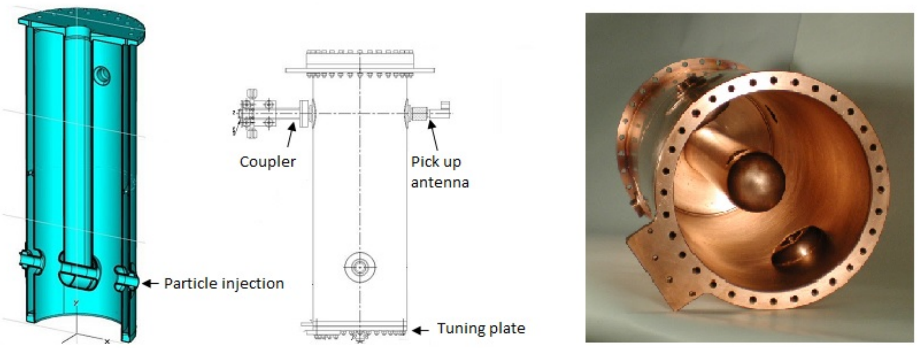

Figure 1.2: Drawing and photo of a room temperature quarter wave cavity.

Particle Acceleration in an RF Cavity

Particle accelerators use electric fields to accelerate charged particles through Lorentz force

$$\mathbf{F} = q(\mathbf{E} + \mathbf{v} \times \mathbf{B}), \tag{1.1}$$

where q is the charged particle, **E** and **B** are the electric and magnetic fields within the cavity and **v** is the velocity of the traveling particle. The kinetic energy of a charged particle increases by an amount equal to the work done,

$$\Delta W = \int \vec{F} d\vec{s} = q \int \vec{E} d\vec{s} = q \int \left(\vec{v} \times \vec{B} \right) d\vec{s}, \tag{1.2}$$

where $\vec{s}$ denotes the displacement. As the vectors $\vec{v}$ and $\vec{B}$ are orthogonal, the kinetic energy increases by the amount of

$$\Delta W = q \int \vec{E} d\vec{s}. \tag{1.3}$$

The fields are created within the resonant cavity, which is designed to create a strong electric field along the beam axis.

Figure 1.3 shows the field distribution of a quarter wave resonator. It is modeled as a coaxial transmission line and is shorted at one end and open at the other. The length of the inner conductor roughly equals the quarter wavelength of the operating frequency. The magnetic field curls around the inner conductor with the maximum magnitude at the shorted end. The electric field reaches its maximum amplitude at the open end of the inner conductor where the beam is accelerated.

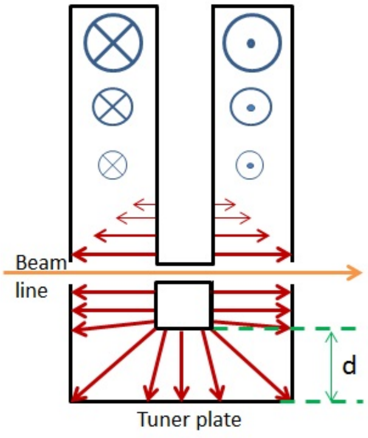

Figure 1.3: Field distribution quarter wave resonator.

Particles are injected into the cavity through an aperture, Figure 1.4.

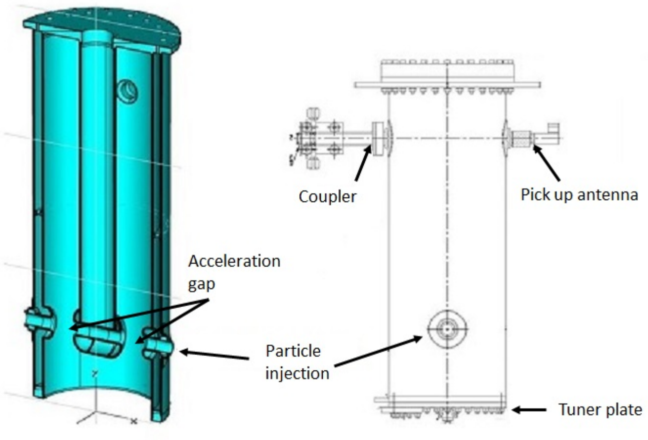

Figure 1.4: Particle injection into a cavity.

This RF quarter wave cavity is a two-gap cavity. The particles travel through the cavity and experience an accelerating electric field as they enter the first gap. The cavity is designed such that, during the field reversal, the particles are shielded from the field by the center electrode. As the particles exit the center electrode and enter the second gap, the electric field is fully reversed again and the particles experience a second acceleration kick in the same direction. The alternating nature of the acceleration field causes the particles to travel in bunches.

Depending on the phase of the arriving particle relative to the acceleration field it can be accelerated or decelerated. The correlation between the acceleration voltage and phase of the injected particle is presented in Figure 1.5.

A LINear ACcelerator (LINAC), such as TRIUMF's ISAC facility, is designed for the acceleration of a single ideal particle which remains in synchronism with the accelerating field and is called a *synchronous particle*. It is designed such that it has the same phase in all cavities.

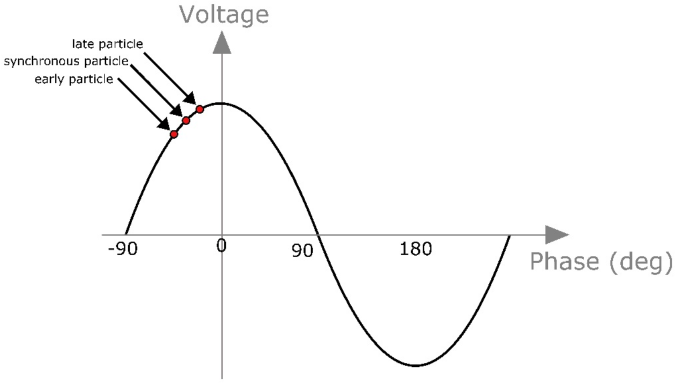

Figure 1.5: Phase of arriving particles versus acceleration voltage within a cavity.

Figure 1.5 shows the acceleration voltage versus the phase for a synchronous, late and early arriving particle, at an acceleration gap. The synchronous particle crosses the gap as the field is rising (negative phase). Early particles receive less kick and late particles receive more kick as the field amplitude grows. In addition to accelerating a particle bunch, synchronism with the rising acceleration field has an additional effect of shortening the bunch length. In order to keep synchronism along the linear accelerator, the particles have to gain a certain amount of speed/energy within each cavity, necessitating a stable acceleration field. To keep the acceleration field amplitude and phase stable, an RF control system is implemented and further explained in the following section.

1.2.3 Cavity Control

The main objective of a cavity control system is amplitude and phase stabilization of the acceleration field and frequency tuning of the cavities natural resonance frequency. Amplitude and phase stabilization is widely seen as cavity field control, the Low Level RF system (LLRF). Frequency tuning is oftentimes included within the amplitude and field stabilization but is a separate tuning loop. As described in section 1.2.2, the speed of the travelling particle bunch is synchronized with the acceleration field. However, the acceleration field and the cavity's resonance frequency are influenced by environmental changes such as temperature variations, which in turn affect the particle bunch's speed gain and the acceleration in further cavities along the accelerator. Hence, the control system's objective is to counteract these field disturbances.

The first step of the control system is to adjust the impedance of the power amplifier in combination with the transmission line impedance to the cavity impedance for maximum power transfer. Disturbances, such as changes in transmission line impedance, coupling factor, or cavity impedance, result in an impedance mismatch yielding phase and amplitude variations. Reasons for disturbances range from internal to environmental effects. Internal effects can be amplifier ripples, RF heating of the cavity, Lorentz force detuning, or helium boiling for superconducting cavities. External effects are mostly environmental ground vibration and temperature changes which affect the cavity itself and the transmission line.

The RF control system to stabilize the acceleration field of a cavity is a complex system and consists of several subsystems. Simrock summarized the state of the art in RF control in 2004 [8]. For completeness, the different subsystems and how they are connected are shown in *Simrock's* block diagram *Breakdown of RF Control Subsystems and some Choices for Implementation*, Figure 1.6.

An amplitude and phase control system focuses on the stabilization of the acceleration field independent of the resonance frequency of the cavity. As mentioned above, there are many causes for acceleration field variation. Given that the acceleration field is synchronized with the speed of the travelling particle bunches, the phase loop's objective is to shift the loop phase to its desired set point and the amplitude loop's objective is to control the

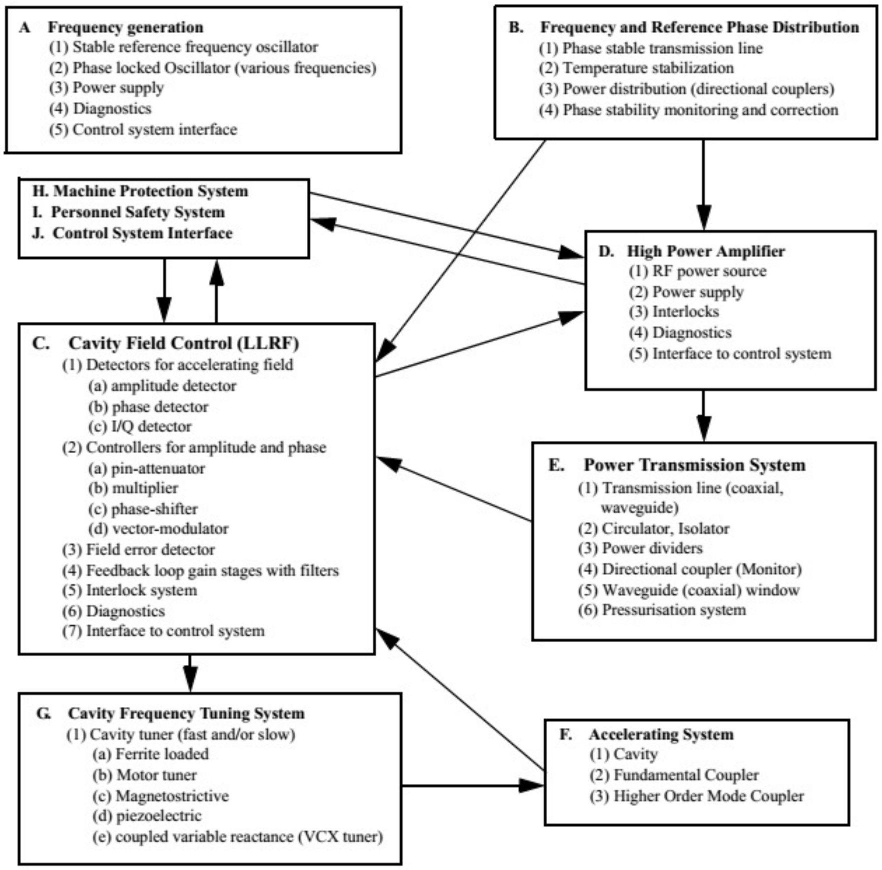

Figure 1.6: Breakdown of RF Control subsystems and some choices for implementation.

amplifier power which must be increased in case of disturbances to maintain the expected velocity gain of the particle bunch to keep synchronism.

The main causes for acceleration field variation are given by ripples created within high power amplifier and resonance frequency changes of the cavity. The resonance frequency ω_0 of a cavity is determined by the inductance and capacitance of the equivalent electromagnetic circuit, which is further explained in chapter 2. If one or both of the parameters change the resonance frequency changes as well. A variation of the cavity's natural resonance frequency leads to detuning of the cavity with respect to the generator or operating frequency. Figure 1.7 shows the necessary increase in generator power to maintain the same acceleration field while the resonance frequency is detuned.

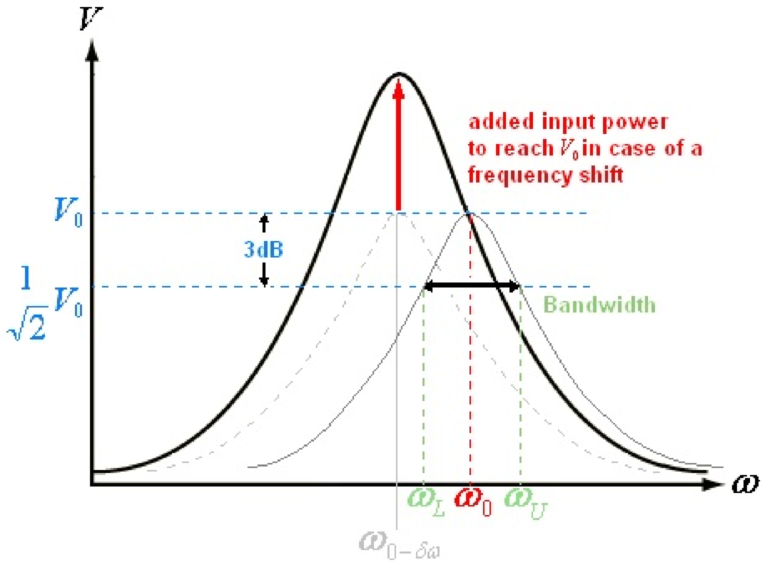

Figure 1.7: Cavity voltage amplitude versus the frequency. The grey curve shows the amplitude curve with its bandwidth. The dashed curve represents the frequency shift and the black curve shows the added input voltage provided by the amplifier to counteract the amplitude loss due to the frequency shift.

To our knowledge, the first amplitude and phase control system was presented in 1965 for a pulsed linear proton accelerator [9]. Amplitude and phase variations of the acceleration field were expected due to beam loading and temperature variations. The amplitude and phase variations are detected through a pick up antenna inserted in the cavity. The error signals are then used to adjust the phase set point using a phase shifter and the amplitude is adjusted through an increased input power. From 1965 until today, amplitude and phase stabilization systems have been widely used and improved for different accelerator machines and requirements [10] [11] [12] [13] [14].

A frequency tuning system in addition to amplitude and phase stabilization reduces the power requirements tremendously. Independent of the amplitude and phase control, a frequency tuning system adjusts the natural resonance frequency of the cavity to its operating frequency by changing its reactive component; in other words, impedance matching for maximum power transfer. In the following section an overview of the present state of technology is given. The main focus lies on resonance frequency tuning of the cavity where amplitude and phase stabilization is given.

1.2.4 Overview of the Present State of Technology of Cavity Frequency Tuning

With respect to the development of a new frequency tuning system, mainly block G of Figure 1.6 is of interest of the overall control system of a cavity. It is assumed that an amplitude and phase stabilization is given.

Particle accelerator machines range from pulsed machines to Continuous Wave (CW) machines. For pulsed and superconducting machines Lorentz force detuning affects the cavity strongly. Depending on the type of particle to be accelerated, beam loading can influence the cavities acceleration field. The quality factor of the different cavities influence the control requirements. For superconducting cavities the cavity bandwidth is so small that tuning is very problematic. Hence, a superconducting cavity is typically operated in overcoupled or undercoupled mode to broaden its bandwidth and simplify the tuning procedure to obtain a stable acceleration field. Additionally, microphonics strongly influence superconducting cavities. Depending on the accelerator machine, cavities are operated with high or low input power. All the different aspects regarding different particle accelerators and cavities yield to different control requirements and different control algorithms.

Frequency Tuning

A detuned cavity means a mismatched impedance between the cavity and the transmission line, which results in wave reflection. The goal of a frequency tuning system is to keep the resonance frequency of a cavity equal to its operating frequency with minimum wave reflection. In other words, the reactive component of the cavity's impedance has to be adjusted such that the reflected component is minimized and a voltage standing wave ratio (VSWR) of 1 is reached. The reactive component of the cavity can be varied by electrical or mechanical tuners. To our knowledge, all operational cavities in the world use the phase information to tune the frequency of the cavity. The phase error can be obtained by measuring the input and output phase, ϕ_{in} and ϕ_{out}, respectively, and calculate the phase lag as

$$\Delta\phi = \phi_{in} - \phi_{out}. \tag{1.4}$$

Given that the phase shift is the integral of the frequency deviation with respect to time, the frequency shift can be calculated as

$$\Delta f = \frac{1}{2\pi}\frac{d\phi}{dt}. \tag{1.5}$$

As it is assumed that the resonance frequency f_0 is sufficiently close to the operating frequency f_i, the phase difference can be approximated by

$$\Delta\phi = tan^{-1}\left(2Q_L\frac{\Delta f}{f_i}\right), \tag{1.6}$$

[15], [16]. Figure 1.8 shows a typical amplitude (power) and phase measurement versus the frequency deviation.

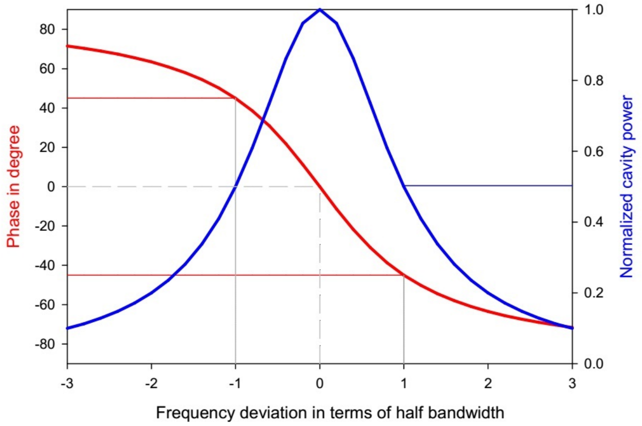

Figure 1.8: Typical phase and power measurement versus deviation between operating and resonance frequency.

Considering that the phase lag is approximately a linear function within the cavity bandwidth, it allows the use of linear and well known tuning algorithms for frequency stabilization. The most commonly used control strategies are PD filters for frequency tuning [17] [18] [19] [20] [21] [22]. Further feedback algorithms include Kalman filters [23], adaptive filters [24], Smith predictors [25] and optimal control. For known repetitive disturbances such as beam loading, microphonics of particular frequencies and lorentz force detuning in pulsed machines, also feed forward systems are implemented. A commonly used feed forward algorithm is an adaptive Least Mean Square (LMS) algorithm [19] [18] [21] [26].

Depending on the cavity itself and the accelerator machine, different hardware options are more suitable to the particular tuning problem. The tuning goal is to change either the capacitance, the inductance or both values of the cavity to match the total impedance of the cavity to that of the waveguide or coaxial cable with the amplifier. The reactive component of the cavity can be changed through mechanical deformation or through an electrical tuning approach. Frequency tuners range from ferrite loaded cavities, motor tuners, magnetostrictive elements, piezoelectric elements, electromagnetic tuner to coupled variable reactance tuners [8].

Ferrite loaded cavities are widely used for the acceleration of heavy ions in synchrotrons. RF frequencies are typically lower than 10 MHz, rendering the use of conventional RF resonators like a pill box impossible as the required spatial dimensions become too big. Reduction of the wavelength of the cavity is reached through a magnetic material load (ferrite). An advantage of ferrite loaded cavities versus pillbox cavities is that there can be simplified frequency tuning through the ferrite core. Changing the bias magnetic field of the core changes its inductance, thereby shifting the wavelength and resonance frequency [27] [28].

Mechanical (motor) tuning is realized through a plunger moving a grounded tuning plate in and out of the cavity, thus changing the capacitance or inductance. In addition to capacitive and inductive tuning, it can also be achieved through tuning by volume which changes both reactive components [29]. A variety of different mechanical tuner setups is available for different cavities, and a different research topic itself.

Considering room temperature cavities, slow tuner responses are sufficient as due to a broad cavity bandwidth, microphonics are not an issue compared to SC cavities. To be persistent with the example of a quarter wave resonator, Figure 1.2 is tuned by a grounded capacitive plate. The plate is moved in and out of the cavity to change the resonance frequency. The capacitance of a quarter wave resonator is given by the distance of the two capacitor plates, the inner conductor and the tuning plate. If the tuner plate moves into the cavity, the capacitance increases and the resonant frequency decreases as the resonance frequency is given by $\omega_0 = \frac{1}{\sqrt{LC}}$.

Mechanical frequency tuning systems are often classified into two main groups: *fast* and *slow* tuners. Slow tuners, motor tuners, are commonly used for coarse frequency adjustments to move the system into the range where fine tuning is possible. Some cavities do not require fast or fine tuning such as CW operated machines with negligible beam loading and room temperature operated cavities where microphonics and lorentz force detuning is negligible. Fast and fine tuning mechanisms are required when microphonics, lorentz force detuning or beam loading influence the acceleration field strongly. Fast fine mechanical tuning is obtained through magnetostrictive materials or piezo elements. They change their physical properties when exposed to magnetic or electric fields. These fast fine tuning mechanisms are typically used in combination with coarse motor tuning [30] [31] [18] [32].

1.3 Summary of Contribution and Outline of this Dissertation

The measured phase lag of a cavity is widely used to tune the resonance frequency of an RF cavity, especially because it is approximately a linear function and classical control approaches can be applied. However, the main problem with the phase measurement based system is the phase measurement itself. Environmental temperature variations affect the transmission system. For a waveguide system the effect is clearly the expansion of the waveguide itself which affects the phase drift. For a coaxial transmission line, temperature drifts lead to changes in the dielectric constant of the cable which in turn yields a phase drift [3]. These temperature induced phase drifts necessitate frequent phase set point adjustments, constant human oversight and compromise the overall tuning accuracy. Hence, it is desirable to eliminate the phase measurement altogether. The measured reflected power mirrors the cavity detune and is an alternative control variable to tune the resonance frequency of a cavity. The measurement is unaffected by environmental temperature changes and therefore a more accurate variable decreasing power requirements and human oversight. As the reflected power of a cavity is a nonlinear function of the frequency deviation, a nonlinear algorithm is required to tune the resonance frequency. Within this dissertation two different control strategies to tune the resonance frequency of an RF cavity are presented. In this regard, the contribution of this thesis is summarized as follows:

1.3.1 Chapter 2: Cavity Theory

This chapter lays out the cavity theory, its field equations and the figures of merit which are relevant for the control algorithm design. The acceleration field within a cavity can be described through a parallel resonant circuit. The differential equation derived from that describes the acceleration field within the cavity and depends on the RF signal coupled into the cavity, its resonance frequency and its quality factor. Cavities can be operated in two different modes, either fed by a source frequency which is called a generator driven resonator or by intrinsic noise which is called self excited loop. Further a description of TRIUMF's RF control system is provided.

1.3.2 Chapter 3: Extremum Seeking Control with main focus on Sliding Mode Extremum Seeking

Within this chapter an overview of extremum seeking control approaches is provided. The main focus lies on the development of sliding mode extremum seeking algorithms and their applications. Section 3.1.1 lays out the development of different algorithms based on the first documented sliding mode extremum seeking approach (in 1974), which focuses on finding and maintaining the maximum or minimum of a steady state performance function. Section 3.1.2 provides an overview of the wide range of applications in the renewable energy sector, automotive industry, and a variety of different industrial applications.

1.3.3 Chapter 4: Development of Control Algorithms Based on Reflected Power Measurements

This chapter describes the development of two different extremum seeking control algorithms to tune the resonance frequency of an RF cavity, which solely rely on the measurement of reflected power.

In section 4.1 an extremum seeking control approach based on gradient estimation of the performance function is derived. A stability analysis of the proposed system is performed using Lyapunov stability theorems and provides conditions for the controller parameters to guarantee stable system behavior up to twice the cavity bandwidth. The theoretical development of the gradient based resonance frequency approach was partly published in [33] and [4].

In section 4.2 a control law based on sliding mode extremum seeking is derived and analyzed in terms of its stability. To achieve the same system stability as for the gradient based approach, also conditions for the controller parameters are determined.

Section 4.3 discusses the parameter choice when the measured reflected voltage instead of the power is used as controller input variable.

1.3.4 Chapter 5: Simulation Study

A simulation study was conducted to examine the suitability of the developed control laws for cavity frequency tuning and to validate the derived conditions for the controller parameters to guarantee stable system behavior up to twice the cavity bandwidth. A variation of the controller parameters shows the effect on the convergence time and control accuracy. Both systems were simulated under perfect conditions. As noise and temperature variations affect a control system and its performance, the simulation study does not allow conclusions in terms of accuracy and convergence speed, but it can be concluded that both systems are suitable to tune the resonance frequency of a cavity.

1.3.5 Chapter 6: Experimental Evaluation

Both of the developed tuning algorithms were tested on a quarter wave resonator test bench. This chapter describes the experimental setup based on a quarter wave room temperature cavity, section 6.1 and the measured results on that test bench, section 6.2. The cavity itself is operated as a generator driven resonator, which is further explained in section 2.3. The resonance frequency is tuned using a stepper motor setup connected to the cavity's tuner plate. The reflected power or voltage measurement is provided through directional couplers. The tuning algorithms are programmed into a Galil motion controller.

Section 6.2 presents the test and measurement results of both developed algorithms. The obtained results for the gradient based and sliding mode based approach are presented in section 6.2.1 and 6.2.2, respectively. The controller parameters are chosen such that the stability conditions (chapter 4) are satisfied. Both control laws are augmented with an initialization phase, to detect the minimum reflected power value, such that oscillations around the optimum operating point are eliminated. Section 6.2.3 summarizes and compares the system characteristics of both systems in terms of accuracy, convergence speed, and sensitivity to noise, with an outcome of higher tuning accuracy for the sliding mode based tuning system. The measurements are further compared to experiences with the traditional phase measurement based frequency tuning system.

1.3.6 Chapter 7: System Commissioning and Performance Measurement on TRIUMF's DTL tank 4 and 5

Based on the test results on the quarter wave resonator test bench and a higher accuracy of the sliding mode based control law compared to the gradient based control law, the sliding mode based extremum seeking control law was chosen to be implemented on TRIUMF's DTL resonator tanks 4 and 5.

Section 7.1 explains the theory of particle acceleration within a single DTL tank. The physical frequency tuning system is presented in section 7.2. The system performance of tank 4 and tank 5 was monitored and presented in section 7.3.2 and 7.3.1, respectively. Tank 5 shows a perfect example of a critically coupled resonator, where the reflected power reaches zero at the optimal operating point. The measurement results on tank 4, on the other hand, show the system performance of a resonator with varying coupling factor. The reflected power does not converge to zero resulting in oscillations around the optimum operating point. Through adjustment of the controller parameters the oscillations could be minimized.

Environmental temperature variations influence the resonator and its surroundings. Within section 7.3.3 the temperature influence on TRIUMF's DTL is analyzed. Section 7.4 discusses the tuning results, the temperature influence and the advantages of the sliding mode based tuning system over the traditional phase measurement based system. The presented tuning results are partially published in [34].

1.3.7 Chapter 8: Summary, Conclusions, and Suggestions for Future Works

The research work accomplished in this thesis is summarized in this chapter. Based on the theoretical, simulation, and experimental studies, general conclusions concerning the outcome of this thesis are provided along with suggestions for future work.

Chapter 2

Cavity Theory

To develop a new resonance frequency control approach based on reflected power measurements, background knowledge of an RF resonant cavity is required. Within this chapter, the cavity, its characteristics in terms of quality factor, the influence of the coupling factor and its operation modes is presented.

A cavity field can mathematically be described by a parallel resonant circuit, section 2.1. The model involves the quality factor and the coupling factor. If one of the latter parameters varies also the cavity field changes. The quality factor of a cavity system represents the losses within it. As the operation of a cavity involves different components, the total losses, or external quality factor, is composed of several quality factors. Each quality factor represents the losses within its component. Section 2.2 gives an overview of the quality factor and how the different components weigh into the total quality factor.

Particles are accelerated through an electromagnetic field within the cavity. To excite the field, the cavity can either be operated under generator driven mode, where an external signal is coupled into the cavity, or under self excited loop, where the intrinsic signal of the cavity is amplified and fed back into the cavity. These operational modes and their characteristics are presented in section 2.3.

The developed acceleration field within each cavity is subject to disturbances, which requires a control system for stabilization. The existing control system at TRIUMF's ISAC I facility is presented in section 2.4.

2.1 Cavity as a Parallel Lumped Circuit

A parallel lumped circuit is the simplest and widely used model for describing a single mode of an accelerating cavity [1]. A basic parallel resonant circuit is shown in Figure 2.1. For simplicity and clarity, the impedance transformation occurred at the power coupler is not included. Hence, the input impedance is equal to the shunt impedance of the parallel resonant circuit. The circuit is powered by a sinusoidal source with a frequency ω_i and fed directly through a transmission line of characteristic impedance Z_0. Note that Z_0 is not the actual cable impedance but the transformed impedance of the coupling circuit. Likewise, the forward voltage v_f, the forward current i_f, the reversed voltage v_r and current i_r are the transformed values of the actual values.

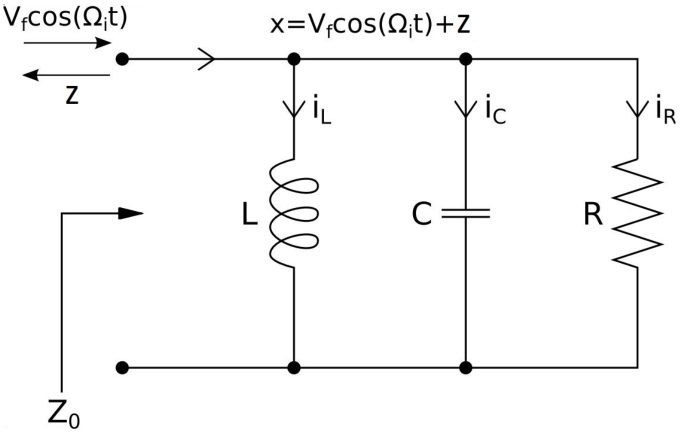

Figure 2.1: Equivalent parallel resonant circuit.

The forward wave going into a cavity is $v_f = V_f cos(\omega_i t)$ and $i_f = I_f cos(\omega_i t)$ with $\frac{v_f}{i_f} = Z_0$. Similarly, the reflected wave is $v_r = V_r cos(\omega_i t)$ and $i_r = -I_r cos(\omega_i t)$ with $\frac{v_r}{i_r} = -Z_0$. With Kirchhoff's current law

$$I(t) = i_L + i_C + i_R = i_f - i_r = \frac{v_f}{Z_0} - \frac{v_r}{Z_0}. \tag{2.1}$$

With $\frac{di_R}{dt} = \frac{1}{R}\frac{dV}{dt}$, $\frac{di_C}{dt} = C\frac{d^2V}{dt^2}$, and $\frac{di_L}{dt} = \frac{1}{L}V$,

$$\frac{dI(t)}{dt} = \frac{di_C}{dt} + \frac{di_R}{dt} + \frac{di_L}{dt} = C\frac{d^2V}{dt} + \frac{1}{R}\frac{dV}{dt} + \frac{1}{L}V. \tag{2.2}$$

The voltage at the cavity is

$$V(t) = v_f + v_r. \tag{2.3}$$

Hence,

$$I(t) = i_f - i_r, \tag{2.4}$$

$$I(t) = \frac{v_f}{Z_0} - \frac{v_r}{Z_0} = \frac{1}{Z_0}\left(v_f - V + v_r\right) = \frac{1}{Z_0}\left(2v_f - V\right), \tag{2.5}$$

$$\frac{dI(t)}{dt} = \frac{2}{Z_0}\frac{dv_f}{dt} - \frac{1}{Z_0}\frac{dV}{dt}. \tag{2.6}$$

Combining equation (2.2) and (2.6) yields

$$C\frac{d^2V}{dt^2} + \left(\frac{1}{R} + \frac{1}{Z_0}\right)\frac{dV}{dt} + \frac{1}{L}V = \frac{2}{Z_0}\frac{dv_f}{dt}, \tag{2.7}$$

with $v_f = V_f cos(\omega_i t)$, the equation of a damped driven oscillator can be written as

$$\frac{d^2V}{dt^2} + \left(\frac{\frac{1}{R} + \frac{1}{Z_0}}{C}\right)\frac{dV}{dt} + \frac{1}{LC}V = -\frac{2}{Z_0 C}V_f \omega sin(\omega_i t). \tag{2.8}$$

Denoting $\frac{\frac{1}{R}\frac{1}{Z_0}}{C} = \gamma$, the damping coefficient and $\frac{1}{LC} = \omega_0$, the natural resonance frequency of the resonator yields

$$\ddot{V} + \gamma\dot{V} + \omega_0^2 V = -\frac{2}{Z_0 C}V_f \omega_i sin(\omega_i t). \tag{2.9}$$

The differential equation (2.9) describes the acceleration field within a cavity.

2.2 Quality factor of an RF cavity

The quality factor of a cavity itself is denoted as the unloaded quality factor and can be expressed as the ratio of the energy stored in the oscillating resonator to the power dissipated per cycle.

$$Q_0 = \frac{Stored \quad Energy}{Power \quad losses \quad per \quad RFcycle} = \omega_0 \frac{U}{P_{cav}}, \tag{2.10}$$

where the losses P_{cav} are caused by the ohmic resistance of the resonator/cavity walls. Hence, it is a measure of power dissipated within the cavity. Or, it can be described as the ratio of the resonance frequency versus the bandwidth. The bandwidth is defined as the allowed frequency change $\delta\omega$ around the central frequency ω_0 where the stored energy remains within half the value of the maximum energy at ω_0 for constant power as

$$Q_0 = \frac{\omega_0}{\Delta\omega} = \omega_0 RC. \tag{2.11}$$

A graph for the stored energy versus the frequency variation $\delta\omega$ and the half power point in shown in Figure 2.2.

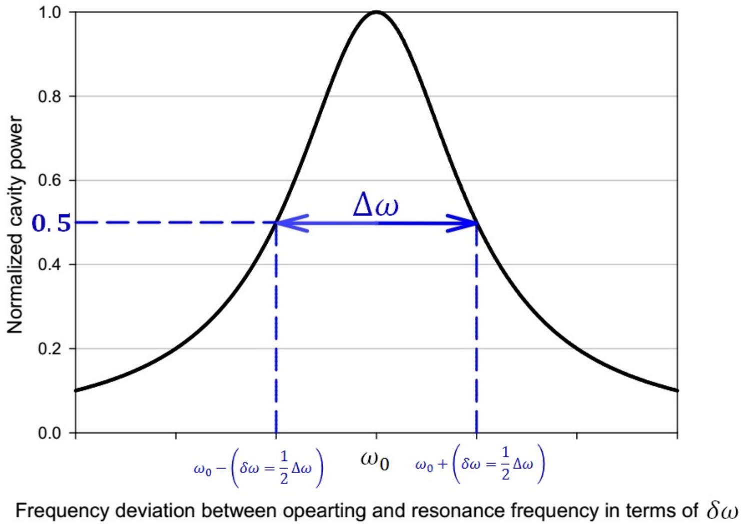

Figure 2.2: Normalized cavity power versus frequency deviation between resonance and operating frequency.

The unloaded quality factor regards only the losses within the cavity walls. To examine a cavity as a whole system the external losses, for example, through the coupler $P_{coupler}$ or the pick-up antenna $P_{pick-up}$ have to be accounted for. The total external losses are calculated by the sum of the individual losses.

$$P_{ext} = P_{pick_up} + P_{coupler} + ... \tag{2.12}$$

The external quality factor is calculated as

$$Q_{ext} = \omega_0 \frac{U}{P_{ext}}. \tag{2.13}$$

All the added losses form the total power loss P_{tot} within a cavity system. The quality factor of the whole cavity system is called loaded quality factor and calculated as

$$Q_L = \omega_0 \frac{U}{P_{tot}}. \tag{2.14}$$

The relation of the different quality factors can be easily calculated as

$$\frac{1}{Q_L} = \frac{1}{Q_0} + \frac{1}{Q_{ext}}. \tag{2.15}$$

2.2.1 Coupling

The standing wave is excited in the cavity by a coupling loop that couples a signal into the cavity as shown in Figure 2.3. The ratio of the cavity quality factor to the external

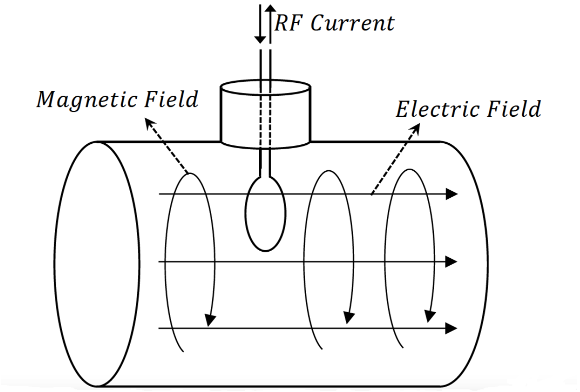

Figure 2.3: Excitation of electromagnetic in the cavity.

quality factor is called coupling beta

$$\beta = \frac{Q_0}{Q_{ext}}. \tag{2.16}$$

Figure 2.4 shows the circuit for an ideal coupler.

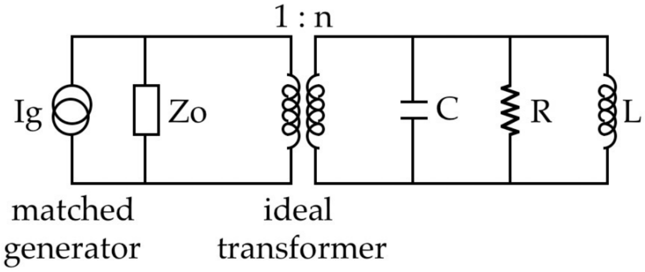

Figure 2.4: Coupling circuit.

With respect to Figure 2.4, β can also be expressed in terms of the impedances as

$$\beta = \frac{R}{n^2 Z_0}. \tag{2.17}$$

Optimal or critical coupling is achieved when $n^2 = \frac{R}{Z_0}$, hence, $\beta = 1$. As $Q_0 = (1+\beta)Q_L$, critical coupling yields $Q_0 = 2Q_L$. In this ideal case maximum energy is transferred to the cavity; no power is reflected due to perfect impedance matching of the cavity with the transmission line. With respect to equation (2.9), it means that the characteristic impedance Z_0 is equal to the shunt impedance of the parallel resonant circuit R. Normal conducting cavities are mainly operated close to perfect impedance matching conditions. Consequently, the differential equation describing normal conducting cavities (2.9) can be rewritten as

$$\ddot{V} + \gamma\dot{V} + \omega_0^2 V = -\gamma V_f \omega_i sin(\omega_i t). \tag{2.18}$$

Superconducting (SC) cavities on the other hand are mostly operated over or under coupled to lower the loaded quality factor, hence, broaden the cavity bandwidth. Since SC cavities can have cavity quality factors of 10^{12}, the bandwidth is very narrow and phase and amplitude stabilization (see section 1.2.3) can be problematic. Over or under coupling broadens the bandwidth and assures stable operation of the RF control system.

2.3 Cavity Operation

Cavities can be operated in a Self-Excited Loop (SEL), Figure 2.6 or as a Generator Driven Resonator (GDR), Figure 2.5. In GDR systems, the cavity is driven by an external RF frequency source which is amplified through an amplifier. In order to build an acceleration field within the cavity, the source frequency must be within the cavity bandwidth and at resonance frequency for a maximum amplitude.

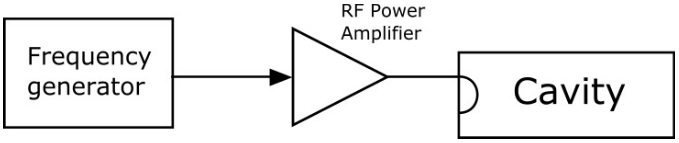

Figure 2.5: Block diagram basic generator driven resonator.

The concept of a SEL was first presented by Delayen [11], [12]. It is basically a positive feedback loop that does not require an RF source to excite the cavity field. Rather, intrinsic noises in the cavity induce oscillations. The output of the cavity is fed back to its input after passing a phase shifter, a limiter and an amplifier. The amplifier as well as the limiter are used to achieve a constant output amplitude. The frequency of the oscillation is the natural resonance frequency of the cavity determined by its reactance.

At oscillation frequency, the loop phase shift is an integer multiple of 2π and the loop gain is greater 1 [35]. The main advantage of the SEL over a GDR is that the cavity is immediately excited, regardless of the frequency. It tracks the frequency shift induced by temperature changes or vibration. Hence, SEL systems are mainly used in superconducting cavities with high quality factors and small cavity bandwidths [23].

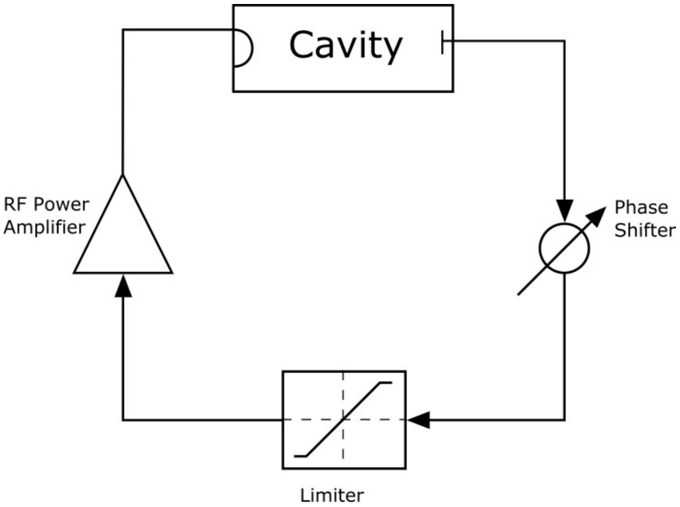

Figure 2.6: Block diagram basic self excited loop.

2.4 TRIUMF's RF Control Systems for Cavity Tuning

TRIUMF's cavity tuning system for the ISAC facility uses classic PID controllers to tune both the field amplitude and the phase. A block diagram of TRIUMF's ISAC control system is shown in Figure 2.7. Amplitude and phase are tuned through the red and the blue tuning loop, respectively. The green tuning loop tunes the natural resonance frequency of the cavity.

2.4.1 Amplitude and Phase Control

A pick up loop antenna inserted in the cavity provides a sample of the acceleration field. The acceleration field can either be directly detected through phase and amplitude detectors or through I/Q detectors. Due to the high frequencies related to RF cavities, typically in the range of MHz to GHz, direct sampling of amplitude and phase is difficult and the signal is down converted first. Down conversion is obtained through a mixer. Figure 2.8 shows a diagram of an ideal mixer, where $y_{RF}(t)$ denotes the high frequency antenna signal, $y_{LO}(t)$ the local oscillator low frequency signal and $y_{IF}(t)$ the down converted intermediate signal. The intermediate signal is then given by

$$\begin{aligned} y_{IF}(t) = & \frac{1}{2} A_{LO} A_{RF} sin\left[\left(\omega_{RF} - \omega_{LO}\right) t + \left(\phi_{RF} - \phi_{LO}\right)\right] \\ & + \frac{1}{2} A_{LO} A_{RF} sin\left[\left(\omega_{RF} + \omega LO\right) t + \left(\phi_{RF} + \phi_{LO}\right)\right]. \end{aligned} \tag{2.19}$$

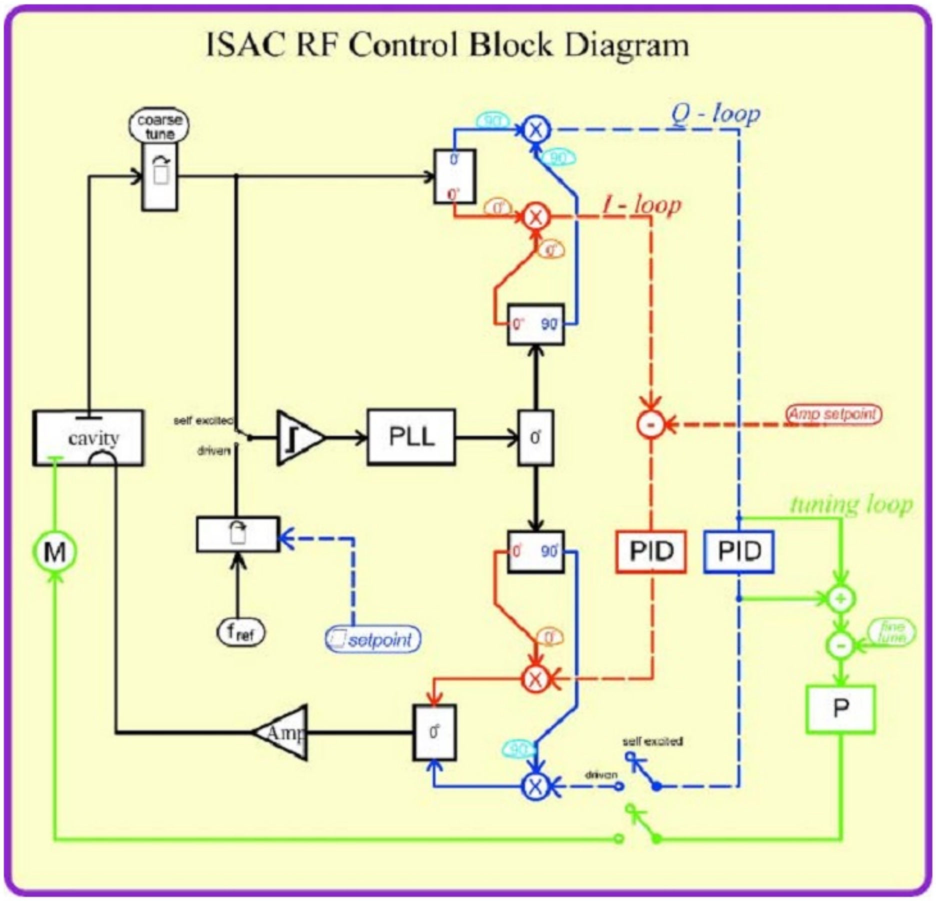

Figure 2.7: ISAC RF Control Block Diagram.

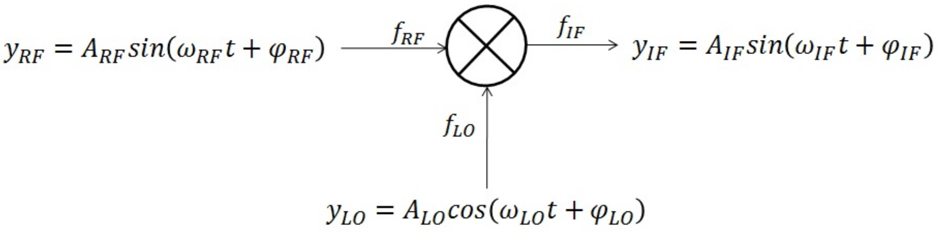

Figure 2.8: Ideal down conversion from high frequency to intermediate frequency using a mixer.

The signal y_{IF} consists of the two signals $\frac{1}{2} A_{LO} A_{RF} sin\left[(\omega_{RF} - \omega_{LO})\, t + (\phi_{RF} - \phi_{LO})\right]$ and $\frac{1}{2} A_{LO} A_{RF} sin\left[(\omega_{RF} + \omega_{LO})\, t + (\phi_{RF} + \phi_{LO})\right]$ representing the lower and the upper sideband signal, respectively. Low pass filtering the upper sideband yields

$$y_{IF}(t) = A_{IF} sin\left(\omega_{IF} + \phi_{IF}\right) \tag{2.20}$$

with $\omega_{IF} = \omega_{RF} - \omega_{LO}$, $A_{IF} = \frac{1}{2}A_{LO}A_{RF}$ and $\phi_{IF} = \phi_{RF} - \phi_{LO}$. With A_{LO} and ϕ_{LO} constant, $A_{IF} \propto A_{RF}$, $\phi_{IF} \propto \phi_{RF}$ and the basic properties of the RF signal are conserved. The IF signal is now of much lower frequency. An important property is that the phase changes or jitter are conserved. Jitter is basically the deviation from the true periodicity of a periodic signal in relation to a reference clock source. For an example a timing jitter of 10 ps at 500 MHz yields a phase difference of 1.8 deg whereas the same timing jitter at 50 MHz yields a phase difference of 0.18 deg. Hence, the requirements of directly sampling an RF signal are much stronger than sampling a down converted signal. After converting the signal to a lower frequency, amplitude and phase can either be detected through an amplitude and phase detector or through IQ sampling, see Figure 1.6 block C. If direct amplitude and phase detection is used, the simplest amplitude detection is built through a diode detector - a diode between the input and the output of a circuit connected to a resistor and capacitor in parallel from the output of the circuit to the ground. The output signal is then A_{IF}, the baseband signal. Phase detection can be obtained through a double balanced mixer similar to Figure 2.8. For phase detector application $\omega_{LO} = \omega_{RF}$, then

$$\begin{aligned} y_{IF}(t) &= \frac{1}{2}A_{LO}A_{RF}sin\left(\phi_{RF} - \phi_{LO}\right) \\ &+\frac{1}{2}A_{LO}A_{RF}sin\left[2\omega_{RF}t + \left(\phi_{RF} + \phi_{LO}\right)\right]. \end{aligned} \tag{2.21}$$

With proper filtering the term $\frac{1}{2}A_{LO}A_{RF}sin\left[2\omega_{RF}t + \left(\phi_{RF} + \phi_{LO}\right)\right]$ can be eliminated and

$$y_{IF}(t) = \frac{1}{2}A_{LO}A_{RF}sin\left(\phi_{RF} - \phi_{LO}\right). \tag{2.22}$$

When the difference between the RF and the LO is ±90 deg, $y_{IF}(t) = 0$. When the difference is 0 deg the output is the maximum positive value and, with a difference of 180 deg, the output is the maximum negative value.

Another way to detect amplitude and phase is IQ demodulation. IQ demodulation makes use of the vector representation of the RF signal. The down converted signal $y_{IF} = A_{IF}sin\left(\omega_{IF}t + \phi_{IF}\right)$ can be rewritten as

$$y_{IF}(t) = A_{IF}cos\phi_{IF}sin\omega_{IF}t + A_{IF}sin\phi_{IF}cos\omega_{IF}t. \tag{2.23}$$

Denoting $A_{IF}cos\phi_{IF}$ as I, the in-phase component, and $A_{IF}sin\phi_{IF}$ as Q, the quadrature-phase component, then

$$y_{IF}(t) = Isin\omega_{IF}t + Qcos\omega_{IF}(t) \tag{2.24}$$

and

$$A_{IF} = \sqrt{I^2 + Q^2}, \tag{2.25}$$

$$\phi_{IF} = atan\left(\frac{Q}{I}\right). \tag{2.26}$$

With a sampling rate of $f_s = 4f_{IF}$ the phase advance between two samples equals 90°. At sampling time $t_0 = 0$, $\omega_{IF}t_0 = 0$ and $y_{IF}(t_0) = Q$. At the sampling time t_1, the phase is 90° advanced, $\omega_{IF}t_1 = \frac{\pi}{2}$ and $y_{IF}(t1) = I$. For the next two samples at t_3 and t_4, the sampled values are $y_{IF}t_2 = -Q$ and $y_{IF}t_3 = -I$, respectively. Hence, IQ sampling results in signal detection in reference to a time or reference phase. The phase difference between the incident wave of the cavity and the pick up signal can be calculated as $\Delta\phi = \phi_{in} - \phi_{out}$. As depicted in Figure 2.7, TRIUMF's control system uses IQ sampling to detect the amplitude and the phase. Both field variables are tuned by separate PID control algorithms.

2.4.2 Frequency Tuning

The frequency tuning loop, illustrated with green in Figure 2.7, uses the phase lag as input signal for the controller. A PD loop regulates the tune of the cavity by adjusting the the reactive component of the cavity through a mechanical motor tuner.

2.5 Summary Cavity Theory

This chapter provided an overview of a cavity, a mathematical model, the influence of quality and coupling factor, the different modes of operation and the existing cavity tuning system at TRIUMF's ISAC I facility.

The cavity model (section 2.1) builds the foundation for the theoretical part of control algorithm development based on reflected power measurements.

The quality factor of a cavity is generally used to describe the controllable bandwidth, which is one of the most important characteristics of a cavity frequency tuning system. As most cavities are not perfectly critically coupled, it will further be shown how the coupling factor affects the cavity performance and its tuning system, 6.2.1, 6.2.2 and 7.3.2.

TRIUMF's existing ISAC I control system (section 2.4) provides the information, that their cavities were tuned as well by using the traditional phase based measurement tuning system. It also builds the foundation of the physical setup for the developed control system, section 7.2.

Chapter 3

Extremum Seeking Control with main focus on Sliding Mode Extremum Seeking

In chapter 4 it will be shown that the reflected power function of a cavity is a minimum function resulting in an extremum seeking control problem. To understand extremum seeking control approaches, this chapter provides an overview of extremum seeking control algorithms with main focus on sliding mode extremum seeking. After providing a general overview on the topic, the development of sliding mode extremum seeking control algorithms and their applications within different industry sectors is presented in section 3.1.

Extremum Seeking Control (ESC) is used to find and maintain either the maximum or minimum of a function. Due to limited knowledge of the plant, in many applications the output of the plant is not analytically known but can be measured. The objective of ESC is to design a controller that drives the system parameters to their optimal value only using the output measurement of the plant, hence, it is a model free control approach. A general extremum seeking block diagram is shown in Figure 3.1.

For simplicity we assume that the plant is a single input single output (SISO) system, where y denotes the output of the steady state performance function and u the input. Without loss of generality a minimum is assumed in this example. The measured output y of the steady state performance map is fed into the controller. The goal of the controller is to change u such that the optimum operating point denoted with $y^\star$ and $u^\star$ is reached and maintained.

Extremum seeking control can be traced back into the early 1920s [36]. Leblanc used ESC to provide maximum power transfer to the output of an electromechanical system. As a model free control approach ESC became very popular and applications range from the automotive industry, renewable energies [37], [38], [39] and a variety of industrial applica-

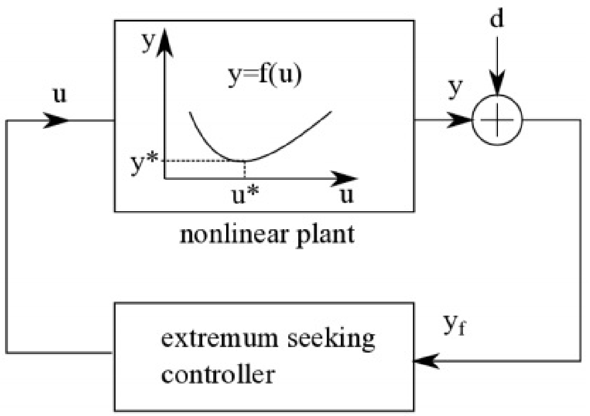

Figure 3.1: Block diagram for a general extremum seeking control scheme.

tions. Different extremum seeking approaches range from performance function gradient calculation, perturbation based ESC, approximation based ESC, neural network ESC to sliding mode extremum seeking. History and comparisons of the mentioned different algorithms are provided in [36] [40] [41] [42]. The widely used and most analyzed extremum seeking scheme is the perturbation based approach, which is considered to be the classical method. It uses a continuous perturbation signal to seek the steady state map and approximate gradient [43]. Regardless of the popularity of extremum seeking algorithms in the industry, the theory of extremum seeking made little progress for many decades. The first rigorous stability analysis of the classic extremum seeking feedback scheme was provided by Krstic and Wang in 2000 [44].

Extremum seeking algorithms can be divided into the groups gradient and non-gradient based algorithms. Gradient based control algorithms, as direct gradient calculation or gradient estimation through perturbation, mainly rely on the gradient of the performance function. Non-gradient based approaches search the extremum point completely independent of the gradient of the performance function. A recently popular non-gradient extremum seeking algorithm is called sliding mode extremum seeking.

3.1 Sliding Mode Extremum Seeking

In this section an overview of the different available sliding mode extremum seeking algorithms and their applications in the industry is provided.

3.1.1 Sliding Mode Extremum Seeking Algorithms

Static Optimization with Sliding Mode Extremum Seeking

To our knowledge, the first sliding mode extremum seeking algorithm was developed by Korovin and Utkin in 1974 [45] [46], it features a monotonically increasing or decreasing reference function and it is the task of the control system to track the reference input. The static optimization problem proposed by Korovin and Utkin [45] is shown in Figure 3.2 and described by the following equations

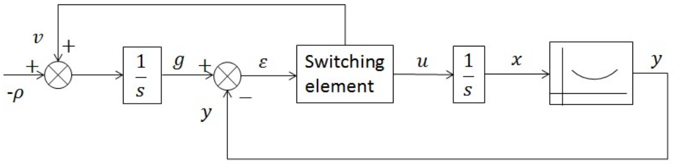

Figure 3.2: Basic sliding mode extremum seeking block diagram for static optimization.

$$y = f(x), \tag{3.1}$$

$$\dot{x} = U_0 sign(s_1 s_2), \tag{3.2}$$

$$s_1 = g(t) - y, \tag{3.3}$$

$$s_2 = g(t) - y + \delta, \tag{3.4}$$

$$\dot{g} = -\rho + Mv(s_1, s_2), \tag{3.5}$$

where $y(t)$ has a unique minimum (for a maximum $+\rho$), U_0, δ, ρ, M are positive design constants and $v(s_1, s_2)$ is obtained through a three positional relay switch. Sliding mode occurs when the function $v(s_1, s_2) = 0$. At a sliding mode, U switches with an infinitely high frequency and either s_1 or s_2 is zero, assuming an ideal system. At $v(s_1, s_2) = 0$ the system follows the monotonically increasing or decreasing reference function $g(t)$ to reach a maximum or minimum, respectively. Static optimization is reached using the system above. However, in the real world system imperfections lead to a limited switching frequency, yielding the well known chattering phenomenon associated with sliding mode control. Since 1974 this basic system has been investigated intensely to improve the chattering phenomenon, the convergence speed, and to make it applicable to systems involving dynamics.

Two Time Scale Sliding Mode and System Delay

Two time scale sliding mode was introduced 1999 by Utkin [47], and Haskara [48]. The idea of the two time scale sliding mode extremum seeking approach relies on the introduction of a control parameter, rather than the control input itself, while a preselected stabilization controller is already in the loop. They considered a SISO nonlinear system

$$\frac{d}{dt}x(t) = f(x(t), u(t)) \tag{3.6}$$

with an output or cost function of

$$y(t) = F(x(t)). \tag{3.7}$$

The main assumption for the two time scale system is given by the existence of a smooth control law

$$u(t) = \beta(x(t)\theta) \tag{3.8}$$

to stabilize the above nonlinear control system. θ is a parameter which determines a unique equilibrium point. A block diagram of the two time scale sliding mode approach is shown in Figure 3.3.

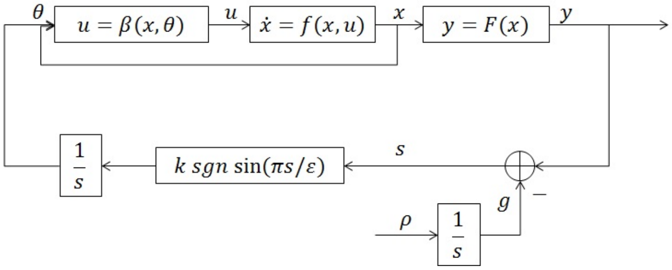

Figure 3.3: Two time scale sliding mode extremum seeking block diagram.

As for the controller, the sliding function is defined as

$$s(t) = y(t) - g(t), \tag{3.9}$$

where $g(t)$ is the increasing or decreasing function satisfying $\dot{g}(t) = \rho$ or $\dot{g}(t) = -\rho$, respectively for a maximum or a minimum. The parameter θ is designed to satisfy

$$\dot{\theta} = ksign\left(sin\left(\frac{\pi s(t)}{\epsilon}\right)\right), \tag{3.10}$$

where ρ, k, ϵ are the extremum seeking design parameter, which are responsible for convergence speed and control accuracy of the system. The advantages of this approach versus the basic static optimization idea are given by a smoothed out discontinuous term as well as the eliminated requirement of the knowledge of the relative degree of the system, since optimization is obtained through a control parameter. The main disadvantage of such a system is given by the dependence of the accuracy of the two time scale closed loop system, which might put restrictions on the adaption rate and the optimization speed. It is based on the assumption that the convergence of $\dot{y}$ to the optimizing parameter $\dot{\theta}$ is much faster than the optimizing process of θ. Hence, the system dynamics have to be much faster than the adaption rate to avoid an interference between the stabilization and the optimization. Pan et al. [49] and Yu and Ozguner [50] analyzed in detail the stability and performance improvement of such a system. Yu and Ozuguner showed [51] that systems with larger time delays result in larger oscillations of the system after reaching the vicinity of the extremal point. They proposed a change of the control parameter ϵ after the optimal working state is reached. The switch of ϵ in the optimal working region locks θ in the region with reduced oscillations. Since the performance criterion is unknown, they used the knowledge detected from the error signal to determine the changing threshold. A typical application for a slow system is ABS Control Strategy with Pneumatic Braking System [51].

Second Order Sliding Mode

Despite the robustness achieved through sliding mode, the undesired chattering phenomenon limits the range of applications. Second order and higher order sliding mode control has been investigated and it is proven to decrease the chattering phenomenon of systems with relative degree one [52], [53]. In order to decrease the chattering, Yu and Ozguner [54] and Pan et al. [55] investigated second order sliding mode extremum seeking. The idea is based on the two time scale sliding mode model with the same main assumption that there exists a smooth control input, equation (3.8), to stabilize the nonlinear system. It uses the first and the second derivative of the switching function, equation (3.9) as

$$\dot{s} = \frac{\partial y}{\partial \theta}\dot{\theta} - \rho \tag{3.11}$$

$$\ddot{s} = \frac{\partial^2 y}{\partial \theta^2}\dot{\theta} + \frac{\partial y}{\partial \theta}\ddot{\theta}. \tag{3.12}$$

The first derivative of the switching function involves the knowledge of the gradient. If the latter is available for measurement this "standard" second order sliding mode system can be used for implementation. Since in general, the derivative of the performance function is not measurable, $\dot{s}$ can not be included in the control law. A special type of second order sliding mode is called the super twisting algorithm [56], [57], which does not involve the first derivative of performance functions. It further augments an integrator into the control loop, such that control becomes a continuous time function. The control law is defined as

$$\theta = -k_1\sqrt{|s|}sign(s) + v, \tag{3.13}$$

$$\dot{v} = -k_2 sign(s), \tag{3.14}$$

with $k_1, k_2 > 0$ being the design constants. Pan et al. [55] compared the super twisting algorithm with standard second order sliding mode ESC (with a measurable gradient of the performance function) with an outcome of a much faster convergence utilizing the twisted algorithm equations (3.13) and (3.14). The main benefits over the first order two time scale system are given by lower chattering phenomenon as well as the application to systems with slower dynamics.

Integer Order and Fractional Order Sliding Mode Extremum Seeking Control

Oliveira et al., [58] [59] as well as Yin et al. [60] proposed an output feedback tracking and extremum seeking controller for a SISO nonlinear system of relative degree one. They extended the previous sliding mode based ESC ideas to achieve new contributions as more general than first order dynamics or convergence from arbitrarily large initial conditions. They reformulated the previous sliding and switching function, equations (3.9) and (3.10) from the two time scale approach, as

$$s(t) = \gamma_1 e(t) + \gamma_2 \int_0^t sign(e(\tau))d\tau, \tag{3.15}$$

$$\theta = \phi(t) sgn\left(sin\left(\frac{\pi}{\epsilon}s(t)\right)\right), \tag{3.16}$$

where $e(t) = y(t) - y_r(t)$, $\gamma_1, \gamma_2, \epsilon > 0$ controller design constants and $\phi(t)$ is a redesign modulation function. Yin et al. [60] further developed the algorithm to reduce oscillations around the optimal point. They basically changed the switching function (3.15) by using a tangent hyperbolic instead of the sign function and reformulated the modulation function. By exchanging the sign function with a tangent hyperbolic function or a saturation function the boundary layer is widened. The continuous function eliminates the jumping of the system trajectory to the minimal space on either side of the sliding mode. However, the wider the boundary layer the lower the chatter but the lower the tracking accuracy [61].

They further developed an algorithm for a fractional order sliding mode based extremum seeking algorithm [62]. The main difference to the integer order (IO) system, equations (3.15) and (3.16), is given by the sliding function now defined as

$$s(t) = \gamma_1 e(t) + \gamma_2 \left({}_0D_t^{q-1} sign(e)\right), \tag{3.17}$$

$$\theta = \phi(t) sgn\left(sin\left(\frac{\pi}{\epsilon}s(t)\right)\right), \tag{3.18}$$

where ${}_0D_t^{q-1}$ is the Riemann-Liouville derivative, $0 < q < 1$ and the other parameters are defined as above. A comparison between the integer order sliding mode extremum seeking control (IO SM ESC) algorithm and the fractional order sliding mode extremum seeking control (FO SM ESC) is presented and shows a better tracking performance for the latter. A double integrator example shows further a comparison between the IO SM ESC, the FO SM ESC and the two time scale sliding mode system (3.9), (3.10) with the result of a slightly faster tracking and accuracy performance of the FO system vs. the IO system, which also outperforms the two time scale system. An application example was provided by a maximum power point tracking problem of a PV array.

Model Based Sliding Mode ESC

For designs where better knowledge of the plant is attainable, Fu and Ozguner investigated model based extremum seeking designs. They presented three different algorithms so as to achieve faster convergence and better robustness. The first approach uses integral sliding mode for systems with fast dynamics and of relative degree one [63]. Through integral sliding mode the gradient of the performance function is estimated and is robust against measurement noise. For systems with relative degree greater than one, Fu [63] introduced a model based extremum seeking algorithm, which incorporates a coordination control component. They further proposed an algorithm for discrete sliding mode gradient estimation [64] [65] as well as asymptotic regulation of a nonlinear SISO plant. The idea is to combine a regulation controller as well as the extremum seeking into a single control loop. The system is designed such that only the sign of the gradient estimation is used within the regulation controller to enhance robustness against noise in the performance measurement. Considering the nonlinear system, equations (3.6) and (3.7), the sliding surface for the sliding mode gradient estimator is defined as

$$s_k = p_{k-1} - \frac{\Delta F_k}{\Delta \theta_k}. \tag{3.19}$$

The observer for $\frac{\partial F}{\partial \theta}$ is designed as

$$p_k = p_{k-1} - V_0 T sign(s_k \Delta\theta_k) sign(\Delta\theta_k), \tag{3.20}$$

where V_0 is a constant and has to be defined such that stability is guaranteed [65]. In a second step the plant controller aims to regulate the derivative of θ to a piecewise constant reference function. To achieve asymptotic regulation a partial state feedback controller [66] is implemented.

3.1.2 Sliding Mode Extremum seeking Applications

In the following, we will present some typical sliding mode extremum seeking applications for all the mentioned model free sliding mode extremum seeking approaches.

Automotive Applications

Probably the most investigated problems regarding SM ESC are antilock braking systems (ABS) and wheel slip control. The objective of ABS is to manipulate the wheel slip such that maximum friction is obtained and the steering stability is maintained, while reaching the shortest distance possible to stop the vehicle. The output of the dynamic system is given by the friction force to control the breaking torque. Many different approaches have been investigated. (1992) Y. K. Chin [67] applied the first developed static optimization controller to the wheel slip problem whereas S. Drakunov [68] (1995) investigated the problem by utilizing the two time scale sliding mode ESC approach, section 3.1.1. Haskara et al. [69], (2000) analyzed the same problem but using a dynamic spark advance controller, which modulates the engine torque output by retarding the spark angle based on the filtered engine RPM measurement. They further used a low pass filter at the output of the sliding mode optimizer to reduce the undesired chattering phenomenon. Peixoto et al [70] (2010) applied the integer order algorithm equation (3.15), (3.16) to the wheel slip problem. Within each of the mentioned papers simulation results are provided to show effectiveness, with reduced chattering phenomenon over time. Theoretically, all algorithms could be applied to the real system. However, in theory, sliding mode control is well known for its robust characteristics towards model uncertainties and disturbances but the downside is given by the undesired chattering phenomenon which can result in heat loss and system instability. A. Aly et al. published 2011 [71] a technical review of Antilock-Braking Systems where they compared different systems and concluded that sliding mode systems up to 2011 are inferior to other systems due to the chattering.

Renewable Energy

Applications in the renewable energy sector vary from wind energy conversion over photovoltaic systems to fuel cells.

Fuel Cells: In Polymer Electrolyte Membrane (PEM) fuel cells hydrogen is fed to the anode and oxygen is fed to the cathode through a compressor. From the control perspective, the objective is to control the compressor such that a desired oxygen excess ratio is maintained and the net power output is maximized. I. Matraji et al. [72] investigated the problem and applied the second order super twisting algorithm equations (3.13), (3.14) to the control problem. Presented simulation results showed the effectiveness of the applied control algorithm to the problem.

Wind Energy: Wind energy is fast growing renewable energy. To gain energy from wind turbines a wind energy conversion system is needed. Power characteristics show that maximum output energy is reached at a certain tip speed ratio. Tip speed ratio is the ratio between the tangential speed of the tip of a blade and the actual velocity of the wind. Given that wind speed changes throughout the day, it is necessary to track the maximum power point (MPPT) independent of the wind speed. Different approaches can be found to solve this problem. The well known systems are tip speed ratio control, which requires wind speed and turbine speed measurement or estimation to regulate the rotational speed.

Another approach is power signal feedback control which requires maximum power curves as well as a reference power to manipulate the rotor speed. An algorithm which does not require any measurements other than the power output itself is the hill climbing process with a drawback of slow convergence. Pan et al. [73] proposed the application of the first sliding mode extremum seeking static optimization process, equations (3.1) to (3.5). Simulation results showed the effectiveness. J.H. Chen et al. further improved the application [74] by utilizing the chaos embedded particle swarm optimization to optimize the control parameter U_0, equation (3.2) as well as using the concept of sliding layers, meaning the usage of a saturation function instead of a sign function, see section 3.1.1.

Photovoltaic Systems: H. T. Yau and C. H. Wu experimentally [75] validated the results of their comparison study [40] of different extremum seeking algorithms with respect to photovoltaic energy. They compared the three different strategies: 1. ESC based on gradient measurement. 2. ESC based on a sinusoidal perturbation signal to extract the gradient of the performance function. 3. Sliding mode extremum seeking based on the static optimization idea proposed by Korovin and Utkin [45]. The experimental analysis validated the simulation analysis with best performance obtained by utilizing the sliding mode extremum seeking algorithm. They further improved the algorithm in the same way as for wind energy optimization, namely using particle swarm optimization to optimize U_0 and using the sliding layer concept to reduce chattering [76].

Industrial

Raman amplifier: A. Peixoto and T. Oliveira [77] extended the single input single output system given in equation (3.15) and (3.16) to a multivariable framework with an application of Raman amplifier. Raman amplifiers are often used in fiber to amplify the optical signal. The Raman amplification is achieved through an interaction between the signal and a pump laser within fiber. From the control perspective the objective is to minimize the variation of the amplified signal power from a desired power level. Presented simulation results showed the controller performance and effectiveness of variation minimization of the amplified signal from a desired power level.

Lighting Control: C. Yin et al. [78] applied the integer order and fractional order extremum seeking approaches given by (3.15), (3.16) and (3.17), (3.18) respectively, to a lighting control system to reduce electrical energy consumption. They built a hardware-in-loop prototype of an adaptive minimum energy lighting control system. The lights in a miniature office with hybrid solar lighting are distributed and the brightness of each lamp can be adjusted individually with the goal of maintaining the right level of illumination. If the lights are split in two parts, far lights and near lights, the electrical energy is given by $E = I_1^2 + I_2^2$, where I_1 denotes the current for the far lights and I_2 denotes the current for the near light. With $I_1 = \omega I$ and $I_2 = (1 - \omega I)$ and $0 \leq \omega \leq 1$ there exist a minimum energy point tracking problem. The hardware in loop simulations with the IO SM ESC as well as the FO SM ESC showed convergence to minimal energy usage where the IO SM ESC system needed almost double the convergence time than the FO SM ESC system.

Chapter 4

Development of Control Algorithms Based on Reflected Power Measurements

In this chapter, two different control algorithms are developed to tune the resonance frequency of an RF cavity. As input variable to the controller the reflected power component of a cavity is used. Based on the mathematical model of an RF cavity, derived in chapter 2, an analytical expression for the reflected power is deduced. The reflected power function is a minimum function, hence, extremum seeking approaches are used to derive the control algorithms. Despite a variety of available extremum seeking approaches two types of extremum seeking approaches are chosen, namely, a gradient based and a non-gradient based algorithm. In section 4.1 a gradient based extremum seeking control algorithm is developed based on a Lyapunov approach. A rigorous stability proof provides the necessary control parameter conditions to guarantee system stability. In section 4.1.3 a non gradient based extremum seeking algorithm is developed based on the concept of sliding mode. Every cavity is different in terms of its characteristics like frequency, sensitivity, and quality factor. To guarantee stable system behavior up to twice of the cavity bandwidth an analysis is provided on how to choose the controller parameter based on the knowledge of the cavity characteristics. An alternative measurement to the reflected power is the reflected voltage. Section 4.3 analyzes the differences between using reflected power and reflected voltage in terms of the controller parameter conditions.

Without loss of generality and to be consistent, the example of the quarter wave cavity is used to explain the tuning procedure. The differential equation describing the acceleration field of RF cavity was given in equation (2.9). As discussed in section 1.2.2, an application of a control input to the mechanical tuner plate changes the resonance frequency $\omega_0 = \frac{1}{\sqrt{LC}}$

of the cavity. Denoting the distance of the grounded capacitive tuner plate to the inner conducter with θ and adding a proportionality parameter k yields the new differential equation describing the cavity field

$$\ddot{x} + \gamma \dot{x} + \left(\omega_0^2 + k\theta\right) x = -\gamma V_f \omega_i sin\left(\omega_i t\right). \tag{4.1}$$

A quarter wave cavity is capacitively tuned, hence, only the capacitance changes through tuning whereas the inductance remains constant. The formula for a parallel plate capacitance, neglecting the fringe effect, is given as $C = \epsilon_r \epsilon_0 \frac{A}{d}$, with $\epsilon_r =$*relative static permittivity*, $\epsilon_0 =$ *electric constant*, $A =$ *area of capacitive plates*, $d =$ *distance of capacitive plates.* With $\omega_0^2 = \frac{1}{LC}$, $\omega_0^2 = \frac{d}{L\epsilon_r \epsilon_0 A}$. Thus, ω_0^2 varies linearly with the distance, which is in case of the cavity equals θ and k is the proportionality constant, which can be measured and is referred to as the cavity sensitivity. $x(t)$ describes the voltage developed within the cavity along the beam axis. With respect to Figure 2.1, $z(t) = x(t) - V_f cos(\omega_i t)$ and equation (4.1) can be rewritten in terms of the reflected signal $z(t)$ as

$$\ddot{z} + \gamma \dot{z} + \left(\omega_0^2 + k\theta\right) z = V_f cos\left(\omega_i t\right)\left(\omega_i^2 - \omega_0^2 - k\theta\right). \tag{4.2}$$

The solution to (4.2) can be analytically obtained in terms of transient and steady state components. The resonance frequency of the cavity varies slowly due to temperature drifts. The goal is to eliminate the difference between resonance and operating frequency or alternatively drive $\omega_0^2(t) + k\theta(t) - \omega_i^2$ to zero. Since the variations in $\omega_0(t)$ and $\theta(t)$ are much slower than the operating frequency ω_i, they can be kept as *frozen* parameters. Consequently, the transient part can be neglected and the cavity signal $z(t)$ is given by its steady state solution. Using phasor analysis and solving for the steady state value of z, yields

$$Z(j\omega) = \frac{V_f\left(\omega_i^2 - \omega_0^2 - k\theta\right)}{s^2 + \gamma s + \left(\omega_0^2 + k\theta\right)}|_{s=j\omega_i} \tag{4.3}$$

$$= \frac{V_f\left(\omega_i^2 - \omega_0^2 - k\theta\right)}{-\omega_i^2 + j\gamma\omega_i + \left(\omega_0^2 + k\theta\right)}. \tag{4.4}$$

Transforming into the time domain

$$z(t) = V_f \sqrt{\frac{\left(\omega_0^2 + k\theta - \omega_i^2\right)^2}{\left(\omega_0^2 + k\theta - \omega_i^2\right)^2 + \gamma^2\omega_i^2}} cos\left(\omega_i t + \phi(\theta)\right). \tag{4.5}$$

The measured reflected power is obtained through the low pass filtered rectified reflected signal, which can be mathematically modeled by a low pass filter as follows

$$\eta + \tau\dot{\eta} = z^2, \tag{4.6}$$

where τ denotes the time constant of the low pass filter and η describes the reflected power and is a function of the control variable θ. The reflected power can then be mathematically expressed as

$$\eta = \frac{1}{2} V_f^2 \frac{\left(\omega_0^2 + k\theta - \omega_i^2\right)^2}{\left(\omega_0^2 + k\theta - \omega_i^2\right)^2 + \gamma^2 \omega_i^2} = F(\theta). \tag{4.7}$$

The ideal reflected power η has a minimum of zero when $\omega_0^2 + k\theta = \omega_i^2$ as shown in Figure 4.1. The control objective is to find a control input θ such that the reflected power converges to zero.

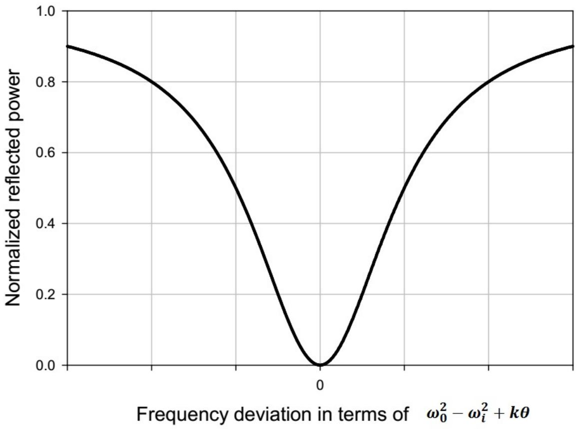

Figure 4.1: Normalized reflected power versus the difference between resonance and operating frequency.

4.1 Gradient Based Algorithm

In the first stage of the gradient based control algorithm development, section 4.1.1, the measured phase lag is used as guidance for the motor direction movement. In the next stage, 4.1.3 the phase lag will be replaced by a gradient estimator.

4.1.1 Phase and Reflected Power

A classical approach to finding a control algorithm for a nonlinear system is to use Lyapunov's second method [79]. It is introduced for a system $\dot{x} = f(x)$ with an equilibrium point of $x = 0$. It states that, considering a function $V(x)$ with continuous first order derivatives such that $V(x)$ is positive definite, $\dot{V}(x)$ is negative semi definite, then the system is locally stable in the sense of Lyapunov. To prove asymptotic stability $\dot{V}(x)$ has to be negative definite and to prove global stability $V(x)$ has to be radially unbounded. In that context, let us choose a positive definite Lyapunov-like function $V = \frac{1}{2}\eta^2$, where η is the reflected power (4.7). Then $\dot{V}$ is given by

$$\dot{V} = \eta\dot{\eta} = \eta\frac{\partial\eta}{\partial u}\frac{\partial u}{\partial t}. \tag{4.8}$$

Denoting $X^2 = (\omega_0^2 + k\theta - \omega_i^2)^2$ we have

$$\dot{V} = \frac{1}{2}V_f^4\frac{X^2\gamma^2\omega_i^2 kX}{\left(X^2+\gamma^2\omega_i^2\right)\left(X^2+\gamma^2\omega_i^2\right)^2}\dot{\theta}. \tag{4.9}$$

Further, let $M = \frac{1}{2}V_f^4\frac{X^2\gamma^2\omega_i^2 k}{\left(X^2+\gamma^2\omega_i^2\right)\left(X^2+\gamma^2\omega_i^2\right)^2}$. Since $M \geq 0$ we have

$$\dot{V} = M\left(\omega_0^2 + k\theta - \omega_i^2\right)\dot{\theta}. \tag{4.10}$$

Choosing the control input as

$$\dot{\theta} = -\mu sign\left(\omega_0^2 + k\theta - \omega_i^2\right)\eta \tag{4.11}$$

yields

$$\dot{V} = -\mu M X sign(X)\eta \leq 0. \tag{4.12}$$

Notice, that $\dot{V} \leq 0$ implies that $\ddot{V}$ is bounded and $V(t) \leq V(0)$. Thus $\dot{V}$ is uniformly continuous. Using Barbalat's lemma [80], $\dot{V} \to 0$ which implies that the reflected power $\eta \to 0$ as $t \to \infty$.

The $sign\left(\omega_0^2 + k\theta - \omega_i^2\right)$ can be obtained by phase measurement between the input and the output phase of the cavity. As shown in Figure 1.8, for a positive difference between the two frequencies, the phase value is positive, whereas a negative deviation results in a negative value. Hence, the phase information gives the direction of the tuner plate movement. Note that the tuning speed $\dot{\theta}$ is a multiplication of the gain μ, the direction and the reflected power η. In an ideally critical coupled cavity the reflected power decreases to zero as the reflected power approaches zero, therefore, the motor speed will asymptotically approach zero and oscillation around the optimum operating point is eliminated. A block diagram of the developed control system is depicted in Figure 4.2.

4.1.2 Stability Analysis

In the following a closed loop stability analysis of the cavity system with control input (4.11) is presented. Consider the dynamic equation (4.2) which can be written in state space formulation $\dot{z} = A_z z + b_z$ as

$$\begin{bmatrix}\dot{z}\\ \ddot{z}\end{bmatrix} = \begin{bmatrix}0 & 1\\ -(\omega_0^2+k\theta) & -\gamma\end{bmatrix}\begin{bmatrix}z\\ \dot{z}\end{bmatrix} + \begin{bmatrix}0\\ V_f cos(\omega_i t)(\omega_i^2-\omega_0^2-k\theta)\end{bmatrix}.$$

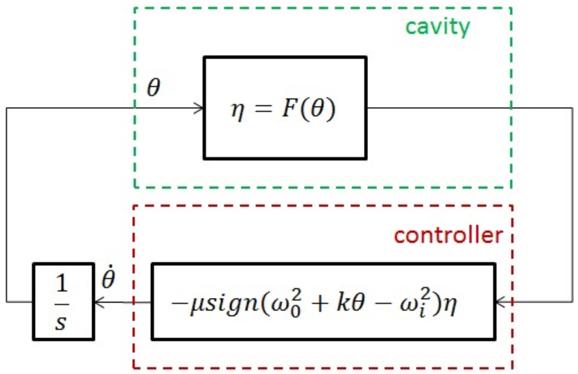

Figure 4.2: Block diagram of phase and reflected power based control algorithm.

Since A_z is a Hurwitz matrix, the following Lyapunov equation [79] is satisfied

$$A_z^T P_z + P_z A_z = -2I. \tag{4.13}$$

Where P_z is symmetric positive-definite and can be computed as

$$P_z = \begin{bmatrix} \frac{\gamma^2+(\omega_0^2+k\theta+1)(\omega_0^2+k\theta)}{\gamma(\omega_0^2+k\theta)} & \frac{1}{\omega_0^2+k\theta} \\ \frac{1}{\omega_0^2+k\theta} & \frac{1}{\gamma}\frac{\omega_0^2+k\theta+1}{\omega_0^2+k\theta} \end{bmatrix},$$

with a time derivative of $\dot{P}$ of

$$\dot{P}_z = \begin{bmatrix} \frac{k\dot{\theta}\left(\omega_0^2+k\theta\right)^2-\gamma^2}{\gamma\left(\omega_0^2+k\theta\right)} & \frac{-k\dot{\theta}}{\left(\omega_0^2+k\theta\right)^2} \\ \frac{-k\dot{\theta}}{\left(\omega_0^2+k\theta\right)^2} & \frac{-k\dot{\theta}}{\gamma\left(\omega_0^2+k\theta\right)^2} \end{bmatrix}.$$

Let us further define the variables $\zeta = \theta$, $\bar{\zeta} = \frac{\omega_i^2-\omega_0^2}{k}$, and $\tilde{\zeta} = \zeta - \bar{\zeta}$. Substituting these new variables into the control law given by equation (4.11) the latter equation can be rewritten as

$$\dot{\tilde{\zeta}} = -\mu sign(k\tilde{\zeta})\eta. \tag{4.14}$$

Since ω_0 is treated as a frozen variable, we also have $\dot{\theta} = \dot{\tilde{\zeta}}$. Let us choose a positive-definite Lyapunov function candidate as follows

$$V = \frac{1}{2}\alpha_z z^T P_z z + \frac{1}{2}\alpha_\eta \eta^2 + \frac{1}{2}\alpha_\zeta \tilde{\zeta}^2, \tag{4.15}$$

where α_z, α_η and α_ζ are small positive scaling constants. Taking the time derivative of V along the system trajectories results in

$$\dot{V} = \frac{1}{2}\alpha_z \dot{z}^T P_z z + \frac{1}{2}\alpha_z z^T P_z \dot{z} + \frac{1}{2}\alpha_z z^T \dot{P} z + \alpha_\eta \eta \dot{\eta} + \alpha_\zeta \tilde{\zeta}\dot{\tilde{\zeta}}. \tag{4.16}$$

After substituting $\dot{z}$, P_z, $\dot{P}_z$, $\dot{\tilde{\zeta}}$ and some manipulations we have

$$\begin{aligned} \dot{V} \;\; = \;\; & -\frac{\alpha_\eta}{\tau}\eta^2 - \alpha_\zeta \mu \eta sign(k\tilde{\zeta})\tilde{\zeta} \\ & - \left[\alpha_z \left(1 - \frac{1}{2}\frac{\left(\omega_0^2 + k\theta\right)^2 - \gamma^2}{\gamma\left(\omega_0^2 + k\theta\right)^2} k\dot{\theta}\right) - \eta\frac{\alpha_\eta}{\tau}\right] z^2 \\ & -\alpha_z \left[1 + \frac{1}{2}\frac{k\dot{\theta}}{\gamma\left(\Omega_0^2 + k\theta\right)^2}\right]\dot{z}^2 \\ & -\alpha_z V_f cos\left(\omega_i t\right)\frac{k}{k\tilde{\zeta} + \omega_i^2}\tilde{\zeta} z \\ & -\frac{\alpha_z}{\gamma} V_f cos\left(\omega_i t\right) k \frac{k\tilde{\zeta} + \omega_i^2 + 1}{k\tilde{\zeta} + \omega_i^2}\tilde{\zeta}\dot{z} \\ & -\alpha_z \frac{k\dot{\theta}}{\left(\omega_0^2 + k\theta\right)^2} z\dot{z}. \end{aligned} \tag{4.17}$$

Now, let us consider a bounded region in the error space given by

$$\Lambda_0 = \{\eta, \tilde{\zeta}, z, \dot{z} | \eta < \eta_0, |\tilde{\zeta}| < |\tilde{\zeta}_0|, |z| < |z_0|, |\dot{z}| < |\dot{z}_0|\},$$

where $\eta_0 > 0$, $\tilde{\zeta}_0$, z_0, $\dot{z}_0$ are some initial state values. In the following, some inequality constraints based on the above bounded region will be developed which will be used to show that if the system states start within Λ_0, they will remain there afterwards with η, $\tilde{\zeta}$, z, $\dot{z}$ approaching zero. Starting with the inequality constraints, given by $|\tilde{\zeta}| < |\tilde{\zeta}_0|$, we have an upper bound of $\frac{k|\tilde{\zeta}_0|}{\omega_i^2 - k|\tilde{\zeta}_0|}$, (line 4 eq.(4.17))

$$\frac{k\tilde{\zeta}}{k\tilde{\zeta} + \omega_i^2} < \frac{k|\tilde{\zeta}_0|}{\omega_i^2 - k|\tilde{\zeta}_0|}, \forall\zeta \in \Lambda_0 \tag{4.18}$$

and an upper bound of $1 + \frac{1}{\omega_0^2 - k|\tilde{\zeta}_0|}$, (line 5 eq.(4.17))

$$\frac{k\tilde{\zeta} + \omega_i^2 + 1}{k\tilde{\zeta} + \omega_i^2} < 1 + \frac{1}{\omega_i^2 - k|\tilde{\zeta}_0|}, \forall\tilde{\zeta} \in \Lambda_0. \tag{4.19}$$

Now, let us define a saturation level L for $sign\left(k\tilde{\zeta}\right)$, yielding an upper bound of $L|\tilde{\zeta}_0|$ for (line 1 eq.(4.17))

$$0 \leq sign\left(k\tilde{\zeta}\right)\tilde{\zeta} \leq L|\tilde{\zeta}_0| \tag{4.20}$$

and

$$\begin{aligned}&-\alpha_\zeta \mu\eta L|\tilde{\zeta}| \leq -\alpha_\zeta \mu\eta sign\left(k\tilde{\zeta}\right)\tilde{\zeta} \leq 0,\\ &\forall\tilde{\zeta},\mu,\eta \in \Lambda_0.\end{aligned} \tag{4.21}$$

Furthermore, assume (line 2 eq.(4.17))

$$\alpha_z\left(1-\frac{1}{2}\frac{\left(\omega_0^2+k\theta\right)^2-\gamma^2}{\gamma\left(\omega_0^2+k\theta\right)^2}k\dot{\theta}\right)-\eta\frac{\alpha_\eta}{\tau}>0. \tag{4.22}$$

This assumption is made for the following matrix Γ to be positive definite, equation (4.35). Let us find a minimum for eq. (4.22) and set a condition for this minimum to be positive. Since

$$\frac{\left(\omega_0^2+k\theta\right)^2-\gamma^2}{\gamma\left(\omega_0^2+k\theta\right)^2}=\frac{1}{\gamma}-\frac{\gamma}{\left(\omega_0^2+k\theta\right)^2} \tag{4.23}$$

and γ being much smaller than $\left(\omega_0^2+k\theta\right)^2$ we have

$$0<\frac{\left(\omega_0^2+k\theta\right)^2-\gamma^2}{\gamma\left(\omega_0^2+k\theta\right)^2}<\frac{1}{\gamma}. \tag{4.24}$$

Utilizing the inequality constraint (4.20) yields

$$-\mu\eta_0 L\frac{k}{2\gamma}<\frac{\left(\omega_0^2+k\theta\right)^2-\gamma^2}{\gamma\left(\omega_0^2+k\theta\right)^2}\frac{1}{2}k\dot{\theta}<\mu\eta_0 L\frac{k}{2\gamma}. \tag{4.25}$$

Hence, we can define a new variable as

$$k_z=\alpha_z\left(1-\frac{1}{2}\mu\eta_0 Lk\frac{1}{\gamma}\right)-\frac{\eta_0\alpha_\eta}{\tau}>0 \tag{4.26}$$

with a condition for k_z to be positive as

$$1>\frac{1}{2}\mu\eta_0 Lk\frac{1}{\gamma}. \tag{4.27}$$

Now, consider the following term from equation (4.17)

$$\alpha_z\left[1+\frac{1}{2}\frac{k\dot{\theta}}{\gamma\left(\Omega_0^2+k\theta\right)^2}\right]. \tag{4.28}$$

Hence, assuming (4.28) to be positive we have a minimum value in Λ_0 when $\dot{\theta} = -\mu\eta_0 L$, $\theta = -|\tilde{\zeta_0}|$. Now, let us define a new variable $k_{\dot{z}}$ as follows

$$k_{\dot{z}} = \alpha_z \left[1 - \frac{1}{2}\frac{k\mu\eta_0 L}{\gamma\left(\omega_0^2 - k|\tilde{\zeta_0}|\right)^2}\right] > 0. \tag{4.29}$$

Using inequality (4.20), we further have (see line 6 eq.(4.17))

$$\frac{k\dot{\theta}}{\left(\omega_0^2 + k\theta\right)^2} < \frac{\mu k\eta_0 L}{\left(\omega_0^2 - k|\tilde{\zeta_0}|\right)^2}. \tag{4.30}$$

Rewriting $\dot{V}$ using the inequality constraints (4.18), (4.19), (4.54), (4.26), (4.29) and (4.30) yields

$$\begin{aligned} \dot{V} \quad \leq \quad & -\frac{\alpha_\eta}{\tau}\eta^2 - k_z z^2 - k_{\dot{z}}\dot{z}^2 \\ & +\frac{\alpha_z V_f k|\tilde{\zeta_0}|}{\omega_i - k|\tilde{\zeta_0}|}|z| \\ & +\frac{\alpha_z}{\gamma}V_f k\left(1 + \frac{1}{\omega_i^2 - k|\tilde{\zeta_0}|}\right)|\tilde{\zeta_0}||\dot{z}| \\ & +\frac{\alpha_z\mu k\eta_0 L}{\left(\omega_0^2 - k|\tilde{\zeta_0}|\right)^2}|z||\dot{z}|. \end{aligned} \tag{4.31}$$

For simplification, let us define new variables as follows

$$\gamma_z = \frac{\alpha_z V_f k|\tilde{\zeta_0}|}{\omega_i^2 - k|\tilde{\zeta_0}|}, \tag{4.32}$$

$$\alpha_{z\dot{z}} = \frac{\alpha_z\mu k\eta_0 L}{\left(\omega_0^2 - k|\tilde{\zeta_0}|\right)}, \tag{4.33}$$

$$\gamma_{\dot{z}} = \frac{\alpha_z}{\gamma}V_f k\frac{\omega_i^2 - k|\tilde{\zeta_0}| + 1}{\omega_i^2 - k|\tilde{\zeta_0}|}|\tilde{\zeta_0}|. \tag{4.34}$$

Rearranging $\dot{V}$ yields

$$\dot{V} \leq -\begin{bmatrix}\eta & |z| & |\dot{z}|\end{bmatrix}\Gamma\begin{bmatrix}\eta \\ |z| \\ |\dot{z}|\end{bmatrix} + \gamma^T\begin{bmatrix}\eta \\ |z| \\ |\dot{z}|\end{bmatrix}, \forall(\eta, z, \dot{z}) \in \Lambda_0$$

where

$$\Gamma = \begin{bmatrix} \frac{\alpha_\eta}{\tau} & 0 & 0 \\ 0 & k_z & -\frac{1}{2}\alpha_{z\dot{z}} \\ 0 & -\frac{1}{2}\alpha_{z\dot{z}} & k_{\dot{z}} \end{bmatrix}, \tag{4.35}$$

$$\gamma^T = \begin{bmatrix} 0 & \gamma_z & \gamma_{\dot{z}} \end{bmatrix}.$$

Now, consider the matrix Γ. This matrix will be positive-definite if $k_z k_{\dot{z}} > \frac{1}{4}\alpha_{z\dot{z}}^2$. Suppose that for a given system and controller parameters, Γ is positive definite. Let us define the sets

$$\mathcal{R} = \{(\eta, z, \dot{z}) \mid \begin{bmatrix} \eta & |z| & |\dot{z}| \end{bmatrix} \Gamma \begin{bmatrix} \eta \\ |z| \\ |\dot{z}| \end{bmatrix} \le \gamma^T \begin{bmatrix} \eta \\ |z| \\ |\dot{z}| \end{bmatrix} \} \cap \Lambda_0 \tag{4.36}$$

$$\mathcal{S} = \{(\eta, \tilde{\zeta}, z, \dot{z}) | V(\eta, \tilde{\zeta}, z, \dot{z}) \le c_1\} \subset \Lambda_0 \tag{4.37}$$

$$\mathcal{T} = \{(\eta, \tilde{\zeta}, z, \dot{z}) | V(\eta, \tilde{\zeta}, z, \dot{z}) = c_2\} \subset \Lambda_0 \tag{4.38}$$

where $0 < c_2 \le c_1$ and c_2 is the smallest constant such that $\mathcal{R} \subset \mathcal{T}$. Since the trajectory defined by $\eta, z, \dot{z}$ is bounded and Γ is positive definite, $\mathcal{R}$ is uniformly bounded. If the initial state is outside $\mathcal{S} - \mathcal{R}$, where $\dot{V} \le 0$, it follows that there exists a finite time t_f such that any solution starting from $\mathcal{S} - \mathcal{R}$, at $t > 0$, will enter $\mathcal{T}$ at t_f, and remain in $\mathcal{T}$ thereafter for all $t \ge t_f$. The residual set $\mathcal{T}$ encompasses an ellipsoid in $\begin{bmatrix} \eta & |z| & |\dot{z}| \end{bmatrix}$ coordinates with its bounds being $\frac{1}{2}\sqrt{\frac{\gamma^T\Gamma^{-1}\gamma}{\lambda_{min}(\Gamma)}}$ and $\frac{1}{2}\sqrt{\frac{\gamma^T\Gamma^{-1}\gamma}{\lambda_{max}(\Gamma)}}$ which can be made small by proper choice of parameters as they depend on γ_z and $\gamma_{\dot{z}}$. Note that the important condition on how to choose the controller parameter μ is given by (4.27).

4.1.3 Gradient Estimation

To completely eliminate the phase measurement, we can alternatively use the sign of the gradient of the steady state reflected power function in Figure 4.1. The sign of the gradient represents $sign(\omega_0^2 + k\theta - \omega_i^2)$ and guides the controller to seek the minimum in the correct direction. To obtain an estimate of the gradient, let us consider a basic discrete time gradient calculation of the reflected power function shown in Figure 4.1. At the sampling instant jT, where T is the sampling period, the value of $\eta_j = \eta(jT)$ is available through measurement whereas the value of $\theta_j = \theta(jT)$ is generated within the controller and therefore available as well. The gradient can then be calculated as

$$\frac{\Delta\eta_j}{\Delta\theta_j} \tag{4.39}$$

where $\Delta\eta_j = \eta_j - \eta_{j-1}$ and $\Delta\theta_j = \theta_j - \theta_{j-1}$.

The gradient estimation in (4.39) is very sensitive to noise, especially when the reflected power approaches zero and $\Delta\eta_j$ and $\Delta\theta_j$ are both close to zero, since in the vicinity of zero, the signal to noise ratio for both denominator and numerator of (4.39) are low. Thus, a Savitzky-Golay filter [81] is used for a smooth estimation of the gradient.

Savitzky-Golay is basically a weighted moving average filter that performs a least-squares curve fit of the signal within the filter window [82]. The weighting coefficients can be obtained from [83]. In this case, a 6-point least squares filter is used and $\Delta\eta_j$ and $\Delta\theta_j$ are calculated as

$$\begin{aligned} \Delta\eta_j &= 0.14286\eta_j + 0.08571\eta_{j-1} + 0.02857\eta_{j-2} \\ &\quad -0.02857\eta_{j-3} - 0.08571\eta_{j-4} - 0.14286\eta_{j-5} \end{aligned} \tag{4.40}$$

$$\begin{aligned} \Delta\theta_j &= 0.142860\theta_j + 0.085710\theta_{j-1} + 0.028570\theta_{j-2} \\ &\quad -0.028570\theta_{j-3} - 0.085710\theta_{j-4} - 0.142860\theta_{j-5} \end{aligned} \tag{4.41}$$

Substituting the gradient into equation (4.11) yields

$$\dot{\theta} = -\mu sign\left(\frac{\Delta\eta_j}{\Delta\theta_j}\right)\eta. \tag{4.42}$$

The control law (4.42), with η given by (4.7), solely depends on the measurement of the reflected power. An ideal critically coupled cavity does not reflect power when the driving and resonance frequencies are equal. In reality, however, not all cavities in operation are critically coupled. Over or under-coupling results in a small amount of reflected power, even when the two frequencies are matched. Considering control law (4.42), the motor speed $\dot{\theta}$ is calculated such that the reflected power η is multiplied by the sign of the gradient and a gain. For a perfectly critical coupled cavity, the motor movement decreases to zero when the two frequencies are matched.

Oscillation Elimination

For an over or under-coupled cavity, motor movement cannot reach zero and the tracked resonance frequency oscillates around the value of the driving frequency.
To eliminate oscillations, let us rewrite control law (4.42) as follows

$$\dot{\theta} = -\mu sign\left(\frac{\Delta\eta_j}{\Delta\theta_j}\right)(\eta - \eta_0), \tag{4.43}$$

where η_0 denotes the minimum reflected power value when both frequencies are matched. For particle accelerator facilities with many cavities, it is undesirable to evaluate each cavity with respect to the coupling factor; hence, the minimum reflected power. Dividing the control system in two phases, namely initialization phase and operating phase, eliminates the evaluation of η_0 of each cavity. Tracking η_0 during the initialization phase with control law (4.42) provides the minimum achievable reflected power value. During the operational phase, control law (4.43) tracks the driving frequency without oscillation around the optimum operating point.

4.1.4 Parameter Determination to Guarantee Stable System Operation up to Twice the Cavity Bandwidth

This section discusses how to choose the controller parameter μ as well as the gradient estimation sample time T to guarantee stable system behavior up to twice the cavity bandwidth when the cavity parameters, Q quality factor, ω_i operating frequency, and k tuner sensitivity are known. Without loss of generality normalized reflected power is assumed. The inequality constraint (4.27) defines how to choose the controller parameter μ to guarantee stable system behavior. The condition is given by

$$1 > \frac{1}{2}\mu\eta_0 L k \frac{1}{\gamma}. \tag{4.44}$$

Inspecting the parameters, η_0 is the initial reflected power, $L = 1$ is the saturation level, and $\gamma = \frac{\omega_0}{Q}$. As the frequency variation between ω_0 and ω_i is very small compared to the operating frequency ω_i, $\gamma \approx \frac{\omega_i}{Q}$. The condition can then be rewritten as

$$\mu < 2\frac{\omega_i}{\eta_0 k Q}. \tag{4.45}$$

The normalized reflected power function is given by

$$F(\theta) = \frac{\left(\omega_0^2 + k\theta - \omega_i^2\right)^2}{\left(\omega_0^2 + k\theta - \omega_i^2\right)^2 + \gamma^2\omega_i^2}. \tag{4.46}$$

When $\omega_0^2 - \omega_i^2 = k\theta$, the reflected power $F(\theta) = 0$. Hence the difference $\omega_0^2 - \omega_i^2$ can be represented by $k\theta$. Defining $F(\theta) = 0$ at $\theta = 0$, and representing the difference $\omega_0^2 - \omega_i^2$ by $k\theta$, the reflected power equation can be rewritten as

$$F(\theta) = \frac{k^2\theta^2}{k^2\theta^2 + \gamma^2\omega_i^2}, \tag{4.47}$$

with $\gamma^2\omega_i^2 = \frac{\omega_0^2\omega_i^2}{Q^2}$. Since ω_0 can be approximated by ω_i, $\gamma^2\omega_i^2 \approx \frac{\omega_i^4}{Q^2}$. This results in a simplified reflected power equation solely depending on the tuner position θ.

$$F(\theta) = \frac{k^2\theta^2}{k^2\theta^2 + \frac{\omega_i^4}{Q^2}}. \tag{4.48}$$

The normalized reflected power versus θ in terms of $\frac{\omega_i^2}{kQ}$ is presented in Figure 4.3. To guarantee stable system behavior up to twice the cavity bandwidth assume the initial position $\theta_0 = -2\frac{\omega_i^2}{kQ}$, which corresponds to an initial normalized reflected power of $\eta_0 = 0.8$, yielding a condition for μ of

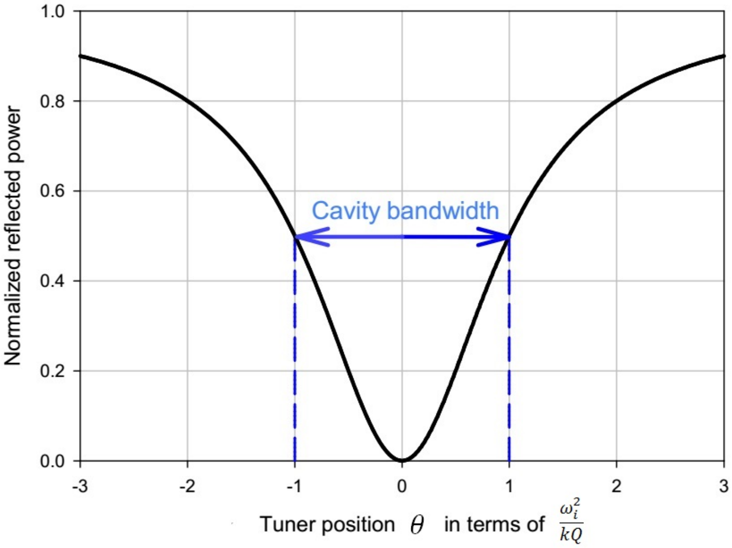

Figure 4.3: Normalized reflected power versus tuner position θ. Plot will be redone properly

$$\mu < 2.5\frac{\omega_i}{kQ}. \tag{4.49}$$

It should be mentioned that the stability proof 4.1.2 does not take the gradient estimation into account. The condition for μ, equation (4.49), is only valid if the sign of the gradient is known, as assumed in the stability analysis. To guarantee stable system behavior using the gradient estimation 4.1.3 the sampling period T has to be chosen carefully. The maximum initial normalized reflected power is given by 0.8. The initial estimated gradient sign $sign\left(\frac{\Delta\eta_j}{\Delta\theta_j}\right)$ is unknown, therefore the initial direction of tuner movement is unknown.

The gradient estimation becomes more sensitive to noise the smaller $\Delta\eta_j$ or $\Delta\theta_j$ become. Assuming that the initial gradient estimation is wrong and the tuner position diverges from the optimum, a maximum movement distance has to be defined in which the gradient estimation has to be recalculated such that θ does not move too far out of the controllable range and the gradient calculation becomes inexact. Define a maximum movement of $\Delta\theta = \frac{\omega_i^2}{kQ}$. With an initial position of $\theta = -2\frac{\omega_i^2}{kQ}$ the maximum divergence from the optimum is given by $\theta_{max} = -3\frac{\omega_i^2}{kQ}$ corresponding to a maximum normalized reflected power of $F(\theta)_{max} = 0.9$, see Figure 4.3. With a maximum of $\dot{\theta}_{max} = -0.9\mu$

$$\Delta\theta_{max} = \int_0^{t=T} 0.9\mu dt \tag{4.50}$$

and

$$\Delta\theta_{max} \leq \frac{\omega_i^2}{kQ} \tag{4.51}$$

the condition for T yields

$$T \leq \frac{\omega_i^2}{0.9\mu kQ}. \tag{4.52}$$

Choosing the controller parameter based on the knowledge of the tuner sensitivity k, quality factor Q and operating frequency ω_i such that the inequalities (4.49) and (4.52) are satisfied guarantees a stable operation up to twice the cavity bandwidth.

4.2 Sliding Mode Based Algorithm

The developed sliding mode based extremum seeking controller to tune the resonance frequency of a cavity is based on the *Two Time Scale Sliding Mode and System Delays* by Utkin [47], presented in chapter 3.

In this case we want to minimize the reflected power, thus maximising the field amplitude within the cavity. Given that the dynamics of the system are much faster than the adjustment of the resonance frequency (in the range of seconds), the reflected power can be seen as static map $F(\theta)$, where the parameter θ describes the tuner plate displacement, see Figure 4.1.4. To avoid tuning motor abrasion resulting from the chattering phenomenon of the two time scale sliding mode approach the control algorithm is augmented such that the motor speed $\dot{\theta}$ is multiplied by the measured reflected power. The control algorithm is then given with the switching function designed as

$$s(t) = F(\theta) - g(t), \tag{4.53}$$

where $g(t)$ is a time decreasing function satisfying

$$\dot{g} = -\rho; \tag{4.54}$$

where ρ is a positive constant and the tuner speed calculated to satisfy

$$\dot{\theta} = k_\theta sgn\left[sin\left(\pi s/\epsilon\right)\right] F(\theta), \tag{4.55}$$

where k_θ is positive gain. A block diagram of the modified extremum seeking control system with sliding mode and a static map is shown in Figure 4.4.

4.2.1 Stability Analysis

The stability of the system with sliding mode will be shown in three steps. In the first step, a reaching condition to converge towards a sliding mode will be presented. The

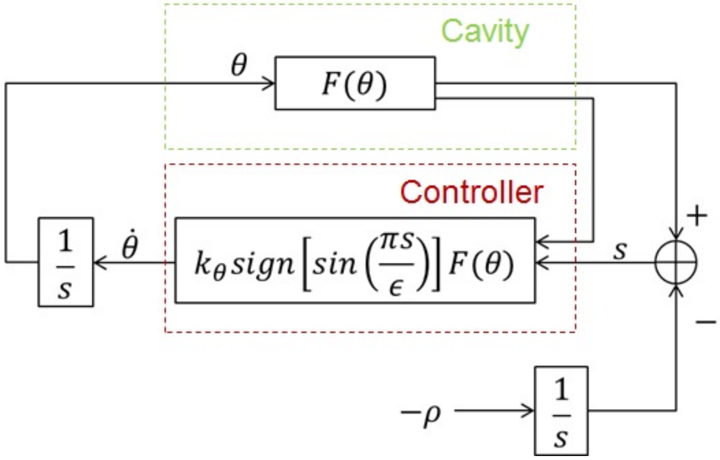

Figure 4.4: Block diagram: Sliding mode based extremum seeking.

reaching condition will not be satisfied in the vicinity of the optimum operating point. The next step discusses how the system asymptotically reaches the optimum operating point after the reaching condition does not hold anymore. The third step discusses the controller parameter condition to guarantee a system stability of twice the cavity bandwidth.

4.2.2 Sliding Mode Reaching Condition

Pan et al. [50], [49] discussed for general single input single output extremum seeking systems with sliding mode the existence of multiple sliding surfaces. Based on the Lyapunov stability approach a condition will be developed for which a sliding surface is an attractive surface, meaning the system will move towards that surface. It will also be shown that if the condition is not fulfilled the system moves away from that surface until a different sliding surface it reached.

In that context consider the Lyapunov-like function $V = \frac{1}{2}s^2$. Then the time derivative of V is given by

$$\dot{V} = s\dot{s} = s\left(\frac{\partial}{\partial\theta}F(\theta)\dot{\theta} + \rho\right), \tag{4.56}$$

with $\frac{\partial}{\partial\theta}F(\theta) = \Psi(\theta)$

$$\dot{V} = -k_\theta\Psi(\theta)sign\left[sin\left(\frac{\pi s}{\epsilon}\right)\right]F(\theta) + \rho s. \tag{4.57}$$

To guarantee $\dot{V}$ to be negative,

$$|\Psi(\theta)|\,F(\theta) > \frac{\rho}{k_\theta} \tag{4.58}$$

determines the sliding mode reaching condition. Without loss of generality we assume $sign\left[sin\left(\frac{\pi s}{\epsilon}\right)\right]$ is initially positive, then until $sign\left[sin\left(\frac{\pi s}{\epsilon}\right)\right]$ changes

$$\dot{V} = \left(-k_\theta\Psi(\theta)F(\theta) + \rho\right)s. \tag{4.59}$$

Choosing k_θ and ρ such that the reaching condition equation (4.58) is satisfied, assuming $\Psi(\theta) > 0$, and denoting $k_\theta \Psi(\theta) F(\theta) = k_s$, then $k_s > 0$. With $V = \frac{1}{2}s^2$, $|s| = \sqrt{2V}$. As s is always positive,

$$\dot{V} < -k_s \sqrt{2V}. \tag{4.60}$$

V approaches zero and a sliding manifold will be attained in finite time, a more detailed analysis is shown in [84]. For the second case of $\Psi(\theta) < 0$ and $-k_\theta \Psi(\theta) - \rho = k_p$, $k_p > 0$ and

$$\dot{V} > k_p \sqrt{2V} \tag{4.61}$$

$$\frac{1}{\sqrt{2}} \frac{dV}{\sqrt{V}} > k_p dt \tag{4.62}$$

$$\sqrt{V} \int_{V_0}^{V} \frac{1}{2} V^{-\frac{1}{2}} dV > \int_{t_0}^{t} k_p dt \tag{4.63}$$

$$V > \left(V_0^{\frac{1}{2}} + \frac{k_p}{\sqrt{2}} (t - t_0)^2 \right). \tag{4.64}$$

Hence V will grow according to the above inequality, yielding s to increase as well until the sign of $sin\left(\frac{\pi s}{\epsilon}\right)$ changes. To guarantee system stability, ϵ has to be chosen such that sign of $sin\left(\frac{\pi s}{\epsilon}\right)$ changes before the system moves outside the controllable range. A condition for ϵ to guarantee system stability will be discussed in section 4.2.4. Once on a sliding mode the switching function s(t) is constant. Hence, with $s(t) = F(\theta(t)) - g(t)$ the reflected power function $F(\theta)$ will decrease on the sliding mode with

$$\dot{F}(\theta) = \dot{g}(t) = -\rho. \tag{4.65}$$

4.2.3 Entering the Vicinity of Optimum

When entering the vicinity of optimum the sliding mode condition does not hold anymore. Denote the time instance when the system enters the vicinity of optimum as t_0. Without loss of generality, assume the system starts on the left side of optimum, $\theta^\star$, and the direction of θ is towards optimum, as depicted in Figure 4.5, then

$$\dot{\theta} = k_\theta F(\theta) \tag{4.66}$$

until the sign of $sin\left(\frac{\pi s}{\epsilon}\right)$ switches. With $s = F(\theta) + \rho t$, the sign of $\dot{\theta}$ changes at time instance t_1, when

$$\Delta s = \epsilon = \Delta F_a + \rho \Delta t_a, \tag{4.67}$$

with $\Delta F_a = F(\theta_1) - F(\theta_0)$ and $\Delta t_a = t_1 - t_0$. At t_1, $\dot{\theta} = -k_\theta F(\theta)$ and the system moves away from optimum until the sign $sin\left(\frac{\pi s}{\epsilon}\right)$ switches again at time instance t_2 with

$$\Delta s = \epsilon = \Delta F_b + \rho \Delta t_b, \tag{4.68}$$

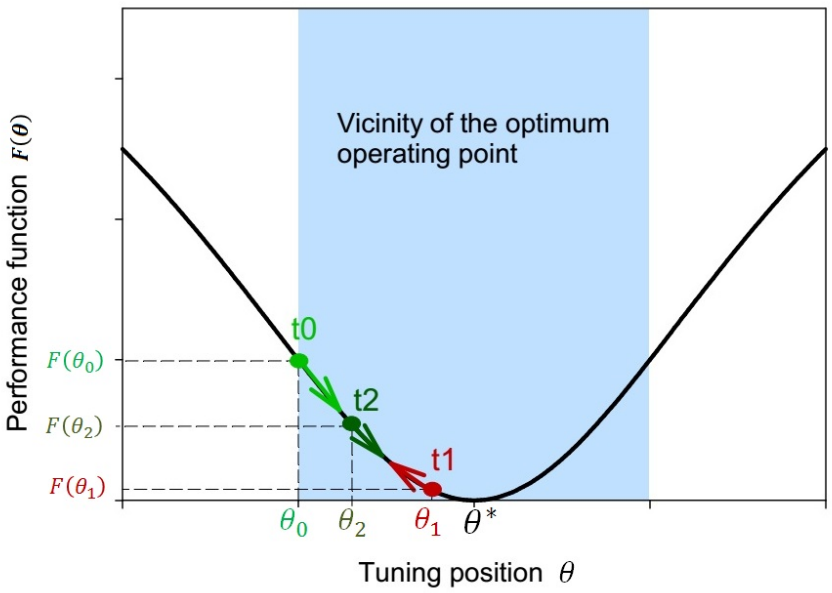

Figure 4.5: Entering the vicinity of optimum.

where $\Delta F_b = F(\theta_2) - F(\theta_1)$ and $\Delta t_b = t_2 - t_1$. Since $\Delta F_a < 0$ and $\Delta F_b > 0$ and

$$\Delta t = \frac{\epsilon + \Delta F(\theta)}{\rho} \tag{4.69}$$

it can be concluded that $\Delta t_a > \Delta t_b$. Thus, the system moves asymptotically towards the optimum operating point $\theta^\star$ with an oscillation of decreasing amplitude as the reflected power $F(\theta)$ decreases.

4.2.4 Parameter Determination to Guarantee Stable System Operation up to Twice the Cavity Bandwidth

The normalized reflected power function was derived in section 4.1.4 and given by

$$F(\theta) = \frac{k^2\theta^2}{k^2\theta^2 + \frac{\omega_i^4}{Q^2}}. \tag{4.70}$$

Substituting $F(\theta)$ and $\frac{\partial}{\partial\theta}F(\theta)$ into sliding mode condition equation (4.58) yields a sliding mode condition depending on the known cavity parameters

$$|\Psi(\theta)|\, F(\theta) = \left| \frac{2k^4\theta^3 \frac{\omega_i^4}{Q^2}}{\left(k^2\theta^2 + \frac{\omega_i^4}{Q^2}\right)^3} \right| > \frac{\rho}{k_\theta}. \tag{4.71}$$

The position θ is within the cavity bandwidth if $-\frac{\omega_i^2}{kQ} \leq \theta \leq \frac{\omega_i^2}{kQ}$ as shown in Figure 4.1.4. To satisfy the sliding mode condition within twice the cavity bandwidth calculate $|\Psi(\theta)|\, F(\theta)$ at $\theta = \pm 2\frac{\omega_i^2}{kQ}$. Choosing the controller parameter such that sliding mode condition holds at $\theta = \pm 2\frac{\omega_i^2}{kQ}$ guarantees the existence of sliding modes within the operational range.

Choosing the range for the sliding mode condition as

$$\frac{1}{4} cavitybandwidth \leq \theta \leq cavitybandwidth \tag{4.72}$$

or $\frac{1}{2}\frac{\omega_i^2}{kQ} \leq \theta \leq \frac{\omega_i^2}{kQ}$ on the positive side and $-\frac{\omega_i^2}{kQ} \leq \theta \leq \frac{1}{2}\frac{\omega_i^2}{kQ}$ on the negative side of θ yields a sliding mode condition

$$0.128\frac{kQ}{\omega_i^2} > \frac{\rho}{k_\theta}, \tag{4.73}$$

see Figure 4.6. If ρ and k_θ are chosen such that equation (4.73) holds, then the system will enter the vicinity of optimum when $F(\theta) < 0.2$ or $-\frac{\omega_i^2}{kQ} < \theta < \frac{\omega_i^2}{kQ}$. The sliding mode condition is not satisfied if $\theta > 2\frac{\omega_i^2}{kQ}$ or $\theta < -2\frac{\omega_i^2}{kQ}$. At $\theta = \pm 2\frac{\omega_i^2}{kQ}$ the normalized reflected power $F(\theta) = 0.8$. Without loss of generality, assume the system starts initially at $\theta = 2\frac{\omega_i^2}{kQ}$ and the system moves in the wrong direction first such that $\dot{\theta} = k_\theta F(\theta)$ until the sign of $\dot{\theta}$ changes. To guarantee that the system will not move outside the controllable range before the sign of $\dot{\theta}$ changes, define a maximum normalized reflected power of $F_{max}(\theta) = 0.9$ corresponding to a position $\theta_{max} = 3\frac{\omega_i^2}{kQ}$. Define the time span before the sign of $\dot{\theta}$ changes as Δt_{max}. Then, the sign of $\dot{\theta}$ switches when

$$\Delta s = \epsilon = \Delta F(\theta) + \Delta t_{max}\rho \tag{4.74}$$

With $\Delta F(\theta) = 0.1$

$$\Delta t_{max} = \frac{\epsilon - 0.1}{\rho}. \tag{4.75}$$

With a maximum of $\dot{\theta}_{max} = 0.9k_\theta$

$$\Delta\theta_{max} = \int_0^{t=\Delta t_{max}} 0.9k_\theta dt. \tag{4.76}$$

As we defined $\Delta\theta_{max} = \frac{\omega_i^2}{kQ}$, we have

$$0.9k_\theta \Delta t_{max} \leq \frac{\omega_i^2}{kQ}. \tag{4.77}$$

Combining equation (4.75) and (4.77) yields a condition for epsilon as

$$\epsilon \leq \frac{\omega_i^2}{kQ}\frac{\rho}{0.9k_\theta} + 0.1. \tag{4.78}$$

Choosing the controller parameter based on the knowledge of the tuner sensitivity k, quality factor Q and operating frequency ω_i such that the inequalities (4.73) and (4.78) are satisfied guarantees a stable operation up to twice the cavity bandwidth.

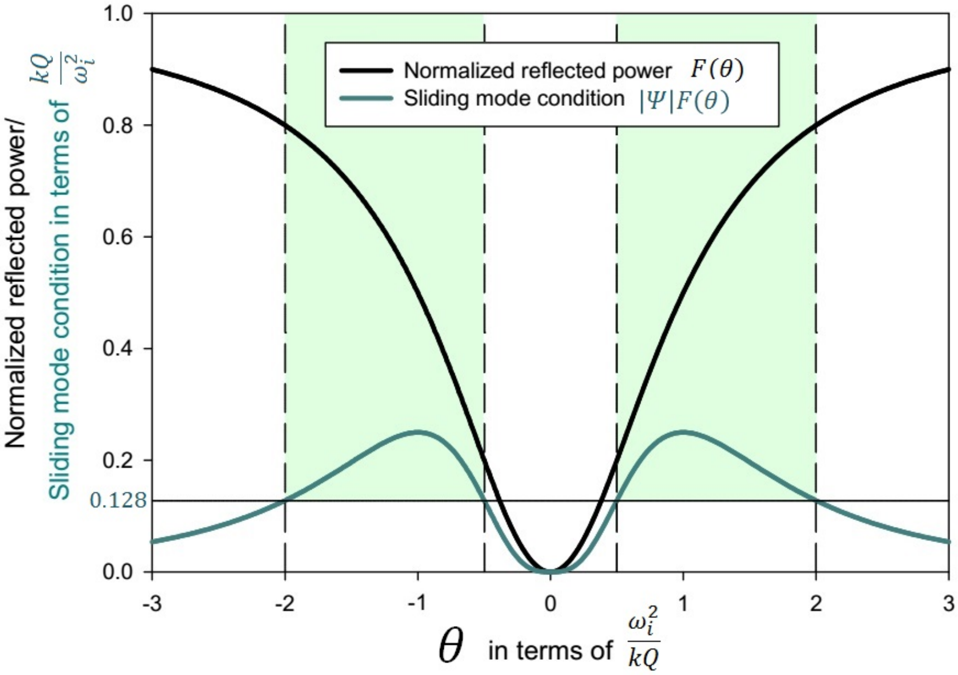

Figure 4.6: Normalized reflected power and sliding mode condition versus θ.

4.3 Using Reflected Voltage Instead of Reflected Power

So far the normalized reflected power function was used as input signal to the controller. An alternative option to the reflected power can be reflected voltage. The reflected voltage is defined as $H(\theta) = \nu$ as

$$\nu = |\sqrt{\eta}| = H(\theta) = \left|\sqrt{F(\theta)}\right|. \tag{4.79}$$

The simplified reflected power function solely depending on the tuner position was given by equation 4.70. Hence, the reflected voltage is calculated as

$$\nu = H(\theta) = \frac{k\,|\theta|}{\sqrt{k^2\theta^2 + \frac{\omega_i^4}{Q^2}}}. \tag{4.80}$$

which is as well a minimum function with the same characteristic of minimum reflected voltage when both of the frequencies are equal. The normalized reflected voltage versus the tuner deviation is shown in Figure 4.7. To guarantee the same system stability, as for using reflected power measurement as tuning variable, the controller parameters have to be

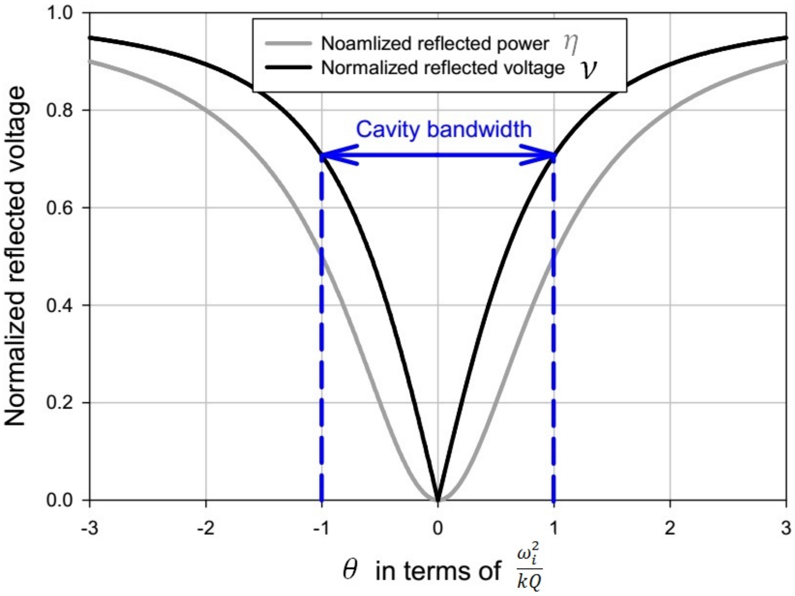

Figure 4.7: Normalized reflected voltage versus tuner position. For reference, the grey curve shows the normalized reflected power.

adjusted due to the steeper reflected voltage function. The next two sections discuss the controller parameter choice using reflected voltage.

4.3.1 Parameter Determination for the Gradient Based Tuning Approach

Following the stability analysis provided in section 4.1.2, the condition for the controller parameter μ can be concluded as

$$\mu < 2\frac{\omega_i}{\nu_0 kQ}, \tag{4.81}$$

where ν_0 denotes the initial reflected voltage. With respect to Figure 4.7 and an initial deviation of $\theta_0 = -2\frac{\omega_i^2}{kQ}$, the initial normalized reflected voltage $\nu_0 = 0.707$ yielding a condition for μ as

$$\mu < 2.828\frac{\omega_i}{kQ} \tag{4.82}$$

and for the gradient estimation sample time

$$T \leq \frac{\omega_i^2}{0.948\mu kQ}. \tag{4.83}$$

4.3.2 Parameter Determination for the Sliding Mode based Tuning Approach

Following the same steps as for the case of using reflected power as controller input, the sliding mode existence condition for the chosen controller equations 4.53 and 4.55 with

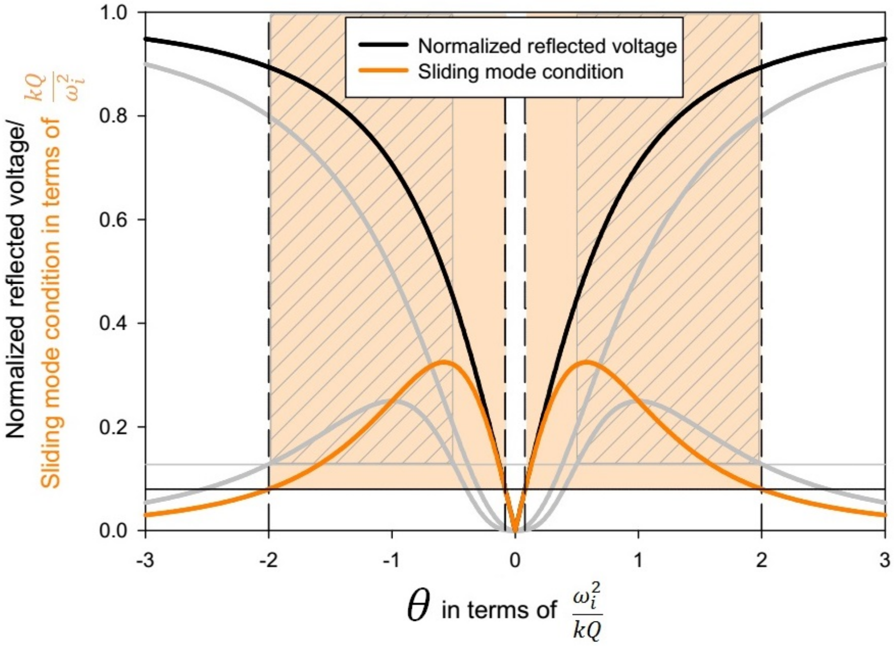

Figure 4.8: Normalized reflected voltage and sliding mode condition versus θ. The grey curves show the normalized reflected power conditions Figure 4.6 for comparison.

respect to the reflected voltage is then given by

$$|\Xi(\theta)|\, H(\theta) > \frac{\rho}{k_\theta} \tag{4.84}$$

with $\Xi(\theta) = \frac{\partial}{\partial\theta}H(\theta)$. To calculate the sliding mode existence condition up to twice the cavity bandwidth substitute $\theta = \pm 2\frac{\omega_i^2}{kQ}$ into equation (4.84). The sliding mode existence condition, for using reflected voltage, is then given by

$$\frac{2}{25}\frac{kQ}{\omega_i^2} > \frac{\rho}{k_\theta}. \tag{4.85}$$

To compute the controller parameter ϵ such that that the system will not move outside the range of $1.5 * cavitybandwidth$ on each side corresponding to $\theta = \pm 3\frac{\omega_i^2}{kQ}$ follow the same approach as for reflected power equation (4.74) to (4.78). The condition for epsilon is then given by

$$e \leq \frac{\omega_i^2}{kQ}\frac{\rho}{0.948k_\theta} + 0.0536. \tag{4.86}$$

Chapter 5

Simulation Study

In this chapter, the controllers designed in the previous chapter are simulated in the Matlab/Simulink environment. The main goal of this section is to check the suitability of the developed control laws and validate the obtained stability conditions guaranteeing stable system behavior up to twice the cavity bandwidth. Section 5.1 presents the block diagram and the simulation results with a varying controller parameter for the gradient based system, section 5.2 presents the equivalent for the sliding mode based control system. In section 5.3 the difference between the reflected power and the reflected voltage as control variable is simulated. The simulation results are discussed in section 5.4. The cavity parameters chosen for the simulations are shown in Table 5.1.

parameter	**value**
Q	$5 * 10^4$
Ω_i	$106\ MHz$
γ	21200
k	$1 * 10^{15}\ Hz^2/m$
V_f	$40\ kV$

Table 5.1: Cavity simulation parameter.

5.1 Gradient Based Algorithm

The simulation scheme for the gradient based control law (4.42) is presented in Figure 5.1. It is comprised of two blocks; one block simulates the steady state cavity behavior and the other one generates the output signal θ that drives the reflected power to zero. The inputs to the cavity include the cavity parameters table 5.1 and the feedback from the controller (θ). The output of the cavity is the reflected power $F(\theta)$ and fed into the controller as well as the position θ, which is needed to calculate the gradient.

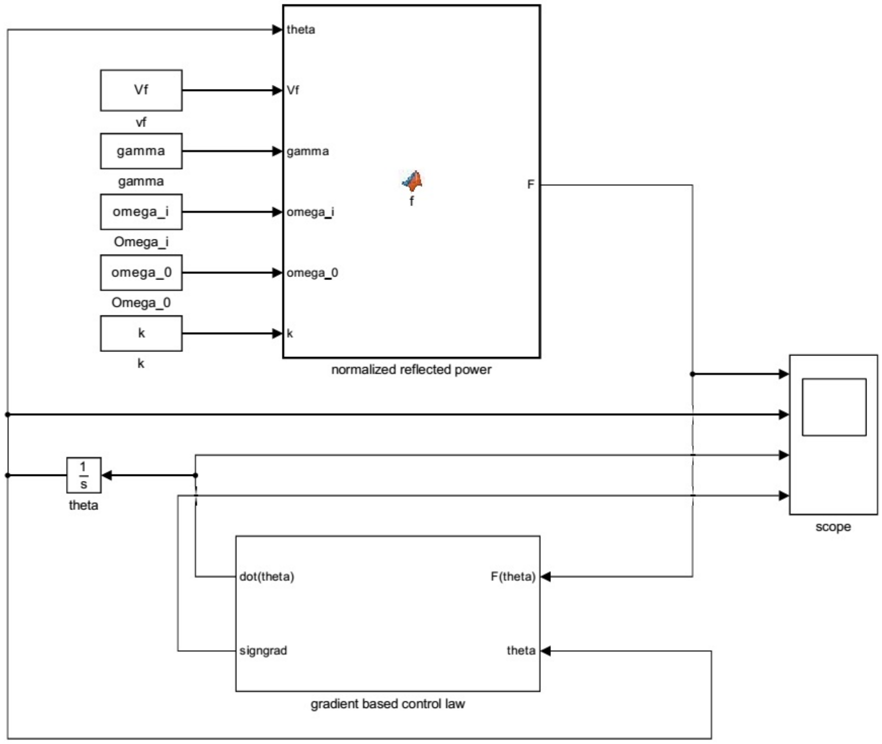

Figure 5.1: Matlab simulation scheme of cavity with gradient based controller.

According to the stability analysis section 4.1.4 and the chosen cavity parameters, the condition for the feedback gain μ to guarantee stable operation is calculated as $\mu < 5.3 * 10^{-11}$. This condition causes the system to be very slow. As the stability analysis is conservative, a higher feedback gain does not necessarily result in unstable system behavior. To achieve a reasonable convergence time the feedback gain μ is chosen as $\mu = 600000000$ for the first two simulation results. The time period T, which determines the time span to recalculate the gradient of the performance function, is calculated according to condition (4.52) as $T = 0.169s$, which guarantees that the system does not move outside the controllable range, corresponding to a maximum reflected power of 0.9 (section 4.1.4). The simulation results are obtained as follows: The initial position θ_0 is chosen as $+2\frac{\omega_i^2}{kQ}$ and $-2\frac{\omega_i^2}{kQ}$ for the simulation results Figure 5.2 and Figure 5.3, respectively. It can be observed that the initial sign of the gradient calculation is always negative. Depending on the initial position of θ, which represents the initial frequency deviation between the operating and resonance frequency, the gradient is initially either right (Figure 5.3) or wrong (Figure 5.2). Since T is chosen such that condition (4.52) is satisfied the gradient is recalculated before the normalized reflected power value reaches 0.9, yielding stable system operations up to twice the cavity bandwidth. The convergence time is observed as approximately one second.

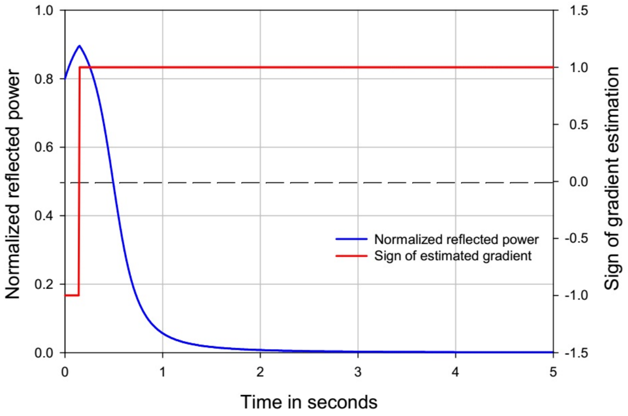

Figure 5.2: Normalized reflected power and sign of calculated gradient with an initial position of $\theta = 2\frac{\omega_i^2}{kQ}$.

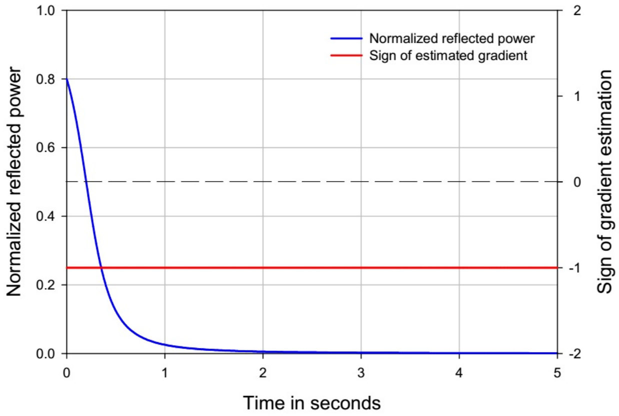

Figure 5.3: Normalized reflected power and sign of calculated gradient with an initial position of $\theta = -2\frac{\omega_i^2}{kQ}$.

Figure 5.4 shows the normalized reflected power versus time for different values of the feedback gain μ. The initial deviation for each value of μ was $\theta_0 = 2\frac{\omega_i^2}{kQ}$ and T was calculated such that equation (4.52) was satisfied. It is clear that the convergence time is influenced by the feedback gain and that stable behavior is achieved through calculation of T.

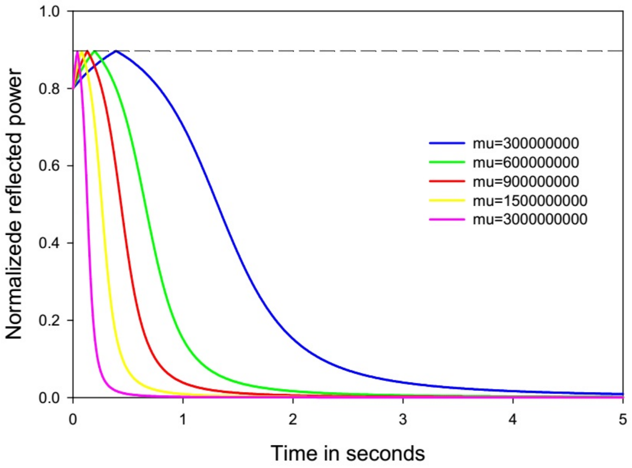

Figure 5.4: Normalized reflected power versus time, initial position of $\theta = 2\frac{\omega_i^2}{kQ}$, and multiple values for the feedback gain μ.

5.2 Sliding Mode Based Algorithm

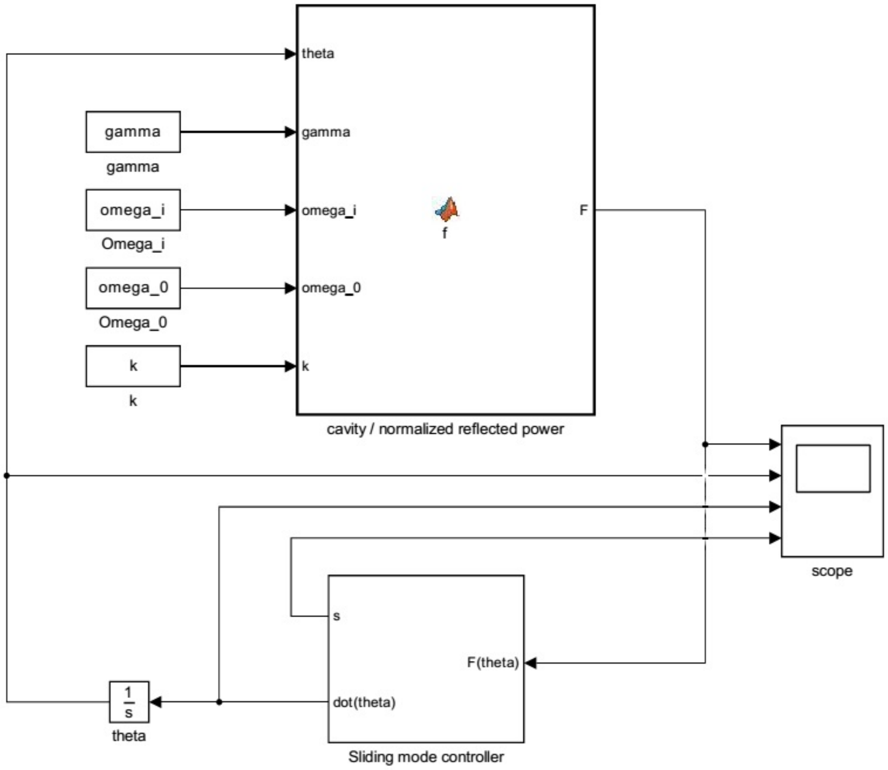

Figure 5.5: Matlab simulation scheme of cavity with sliding mode based controller.

The simulation scheme for the sliding mode based control law equation (4.53) and (4.55) is presented in Figure 5.5. It is built in the same way as for the gradient based approach and comprised of two blocks; one for the cavity behavior and the other one generates the output signal θ. For the first two simulation results the controller parameter ρ is chosen as $\rho = 1$; k_θ and ϵ are calculated such that the conditions for stable system behavior (section 4.2.4, equations (4.73) and (4.78)) are satisfied. The initial condition θ_0 was given by $2\frac{\omega_i^2}{kQ}$ and $-2\frac{\omega_i^2}{kQ}$, respectively for Figure 5.6 and 5.7. As illustrated, depending on the sign of the initial frequency deviation, the system moves in different directions. Since ϵ is chosen such that the reflected power does not exceed $F(\theta) = 0.9$, the motor movement direction changes accordingly. Figures 5.6 and 5.7 show the normalized reflected power (in blue) and the sliding function s (in red) versus time. The grey highlighted area denotes the movement along a sliding mode. The function s is constant and the reflected power $F(\theta)$ decreases with a slope of ρ. The convergence time is mainly influenced by the choice of ρ. Figure 5.8 shows the simulation result for different values of ρ and an initial position $\theta_0 = 2\frac{\omega_i^2}{kQ}$, ϵ and k_θ are recalculated for each ρ to satisfy the stability conditions. It can be observed that the oscillation amplitude around the optimum operating point decreases with an increasing ρ, and the oscillation frequency increases. The oscillation amplitude is also decaying and asymptotically approaching zero as the reflected power decreases.

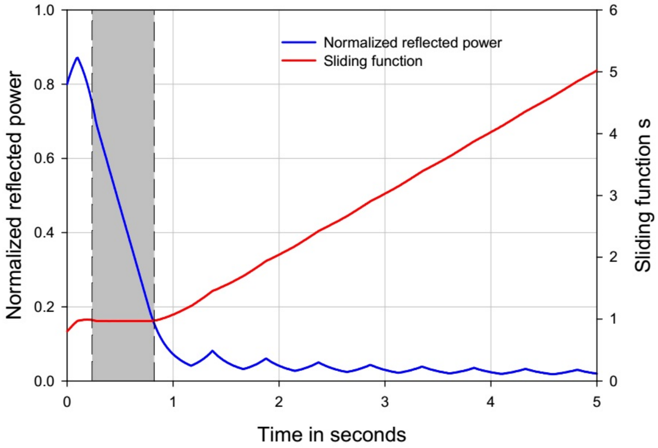

Figure 5.6: Normalized reflected power versus time, initial position of $\theta = 2\frac{\omega_i^2}{kQ}$, $\rho = 1$.

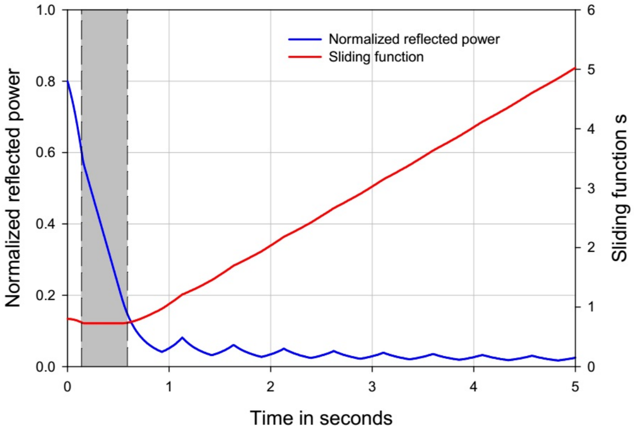

Figure 5.7: Normalized reflected power versus time, initial position of $\theta = -2\frac{\omega_i^2}{kQ}$, $\rho = 1$.

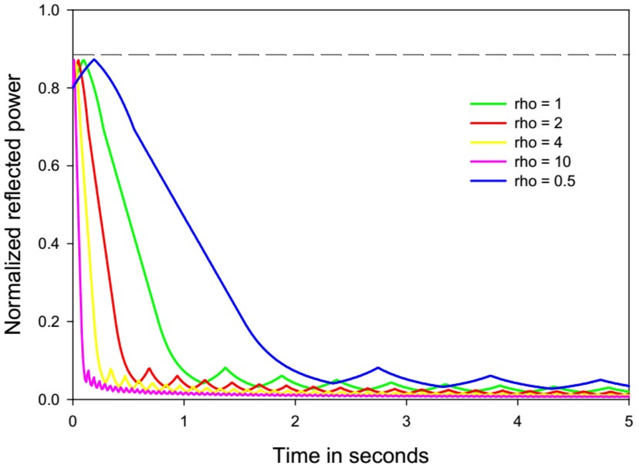

Figure 5.8: Normalized reflected power versus time for different values of ρ, initial position $\theta_0 = 2\frac{\omega_i^2}{kQ}$.

5.3 Voltage Versus Power

This section presents simulations that demonstrate the difference between using reflected power and reflected voltage as controller inputs. As the simulation results are very similar for both developed control approaches, we will only focus on the sliding mode based approach. Figure 5.9 presents the normalized reflected power versus time for the two cases - the measured power (red) and the measured voltage (black) as controller inputs. The controller parameter ρ is in both cases chosen as 1, k_θ and ϵ are calculated to satisfy the stability condition equations and the initial position $\theta_0 = 2\frac{\omega_i^2}{kQ}$. The convergence time as well as the oscillation amplitude are improved for the case where reflected voltage is used.

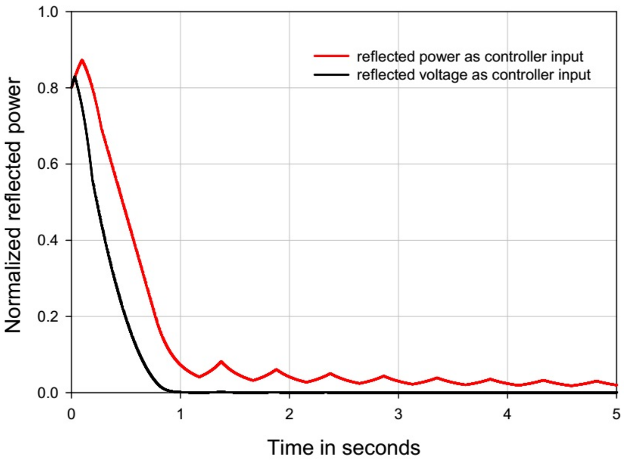

Figure 5.9: Normalized reflected power versus time for different values of ρ, initial position $\theta_0 = 2\frac{\omega_i^2}{kQ}$.

Figure 5.10 shows a $3D$ diagram of θ, $\dot{\theta}$ and the simulation time corresponding to the simulation result Figure 5.9. The high frequency switching of the sign of $\dot{\theta}$ indicates the movement along a sliding mode where s is constant. It can be observed that the movement along a sliding mode is extended for the case of using reflected voltage. For the same position of θ the absolute value of $\dot{\theta}$ is bigger when using reflected voltage versus using reflected power, yielding a faster convergence and a smaller oscillation amplitude around the optimum operating point $\theta = 0$.

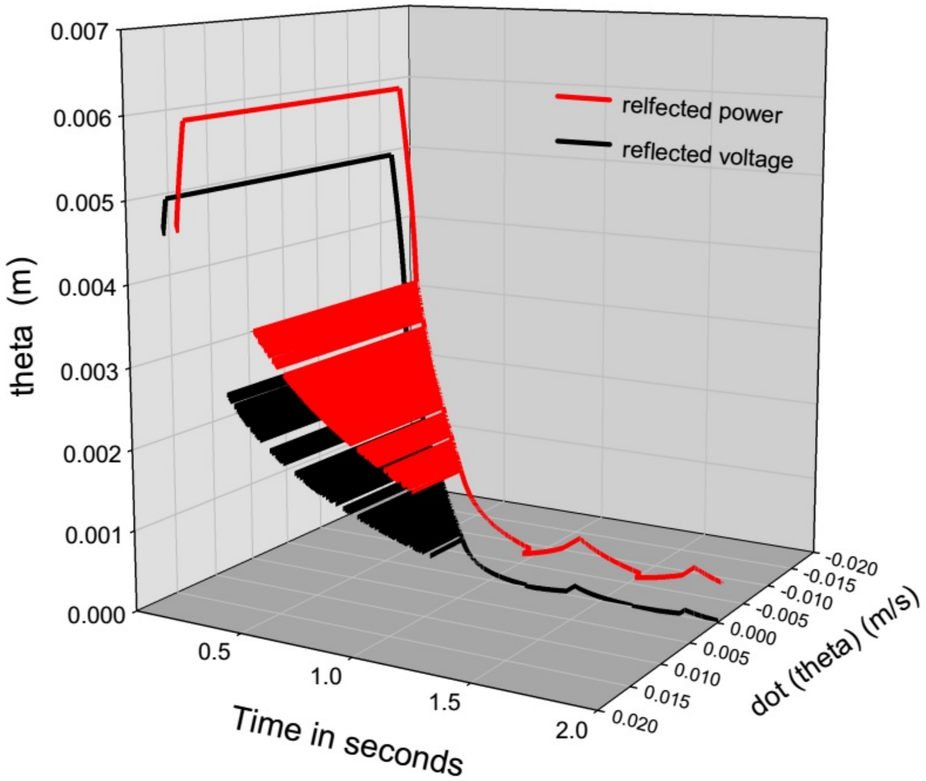

Figure 5.10: Normalized reflected power versus simulation time for the two different cases of using reflected power (red) or reflected voltage (black) as controller input variable, initial position $\theta_0 = 2\frac{\omega_i^2}{kQ}$.

5.4 Simulation Results Discussion

Both developed control laws of chapter 4 were simulated under perfect conditions, noise and system delay times were not considered. The convergence time was influenced by the choice of controller parameter and was shown to be in the millisecond range for high controller gains μ and ρ. It should be noted that for a real system the motor speed is limited by the motor itself and its setup, which in turn limits the convergence speed. Since the cavity system was simulated under perfect conditions, the simulation study does not allow conclusions in terms of convergence speed and system accuracy. But, it allows the conclusion that both control approaches are suitable to tune the resonance frequency of a cavity. Regarding the controller parameters, the simulation results verified the conditions to guarantee stable system operation up to twice the cavity bandwidth for the sliding mode based control approach, obtained in section 4.2.1. Although the controller parameter μ of the gradient based system was chosen much higher than the stability condition (equation 4.49), the simulation results validate the condition for the time period T.

Chapter 6

Experimental Evaluation

To test the algorithms developed in chapter 3, a test bench based on a quarter wave room temperature cavity was built. This chapter presents the physical setup of the test bench in section 6.1 and test and measurement results of the developed control approaches based on gradient estimation and sliding mode extremum seeking in section 6.2.

6.1 Experimental Test Bench Setup

Figure 6.1 shows a block diagram of the setup for testing the developed control law based on reflected power, and phase measurement used for tuner direction, section 4.1.1. The block diagram solely depending on reflected power measurements, section 4.1.3 and section 4.2, is presented in Figure 6.2.

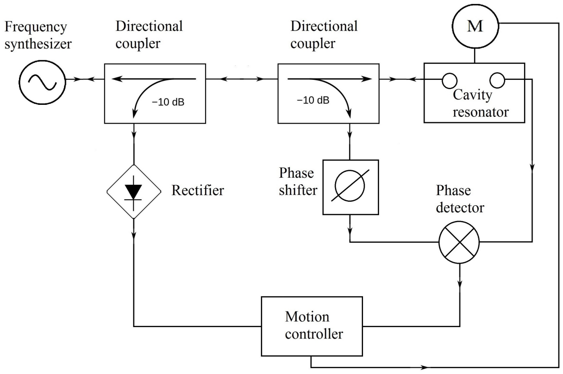

Figure 6.1: Block diagram of the experimental setup using phase, for tuner movement direction, and reflected power to tune the resonance frequency of the cavity.

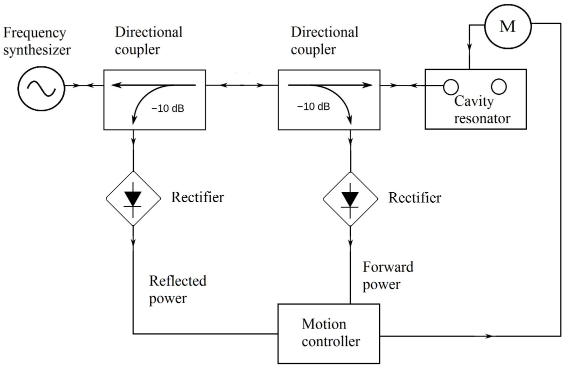

Figure 6.2: Block diagram of the experimental setup solely depending on reflected power measurements.

A $104MHz$ normal-conducting quarter-wave cavity resonator (Figure 1.2) with a measured quality factor of about 5200 and a corresponding cavity bandwidth of $20kHz$ is used as the test cavity.

The tuner plate, attached to the top of the cavity (Figure 6.3), is a $1mm$ thick copper sheet radially slotted and formed with an "oil can" undulation to increase the flexibility. The same tuner plates are used for TRIUMF's superconducting quarter wave cavities [85]. The tuner plate movement is limited to $\pm 2mm$.

The cavity sensitivity in terms of frequency deviation with respect to tuner plate movement is roughly measured as $\pm 30kHz \approx \pm 2mm$. A quarter wave cavity is capacitively tuned. To broaden the frequency range, with the same tuner plate movement, the cavity sensitivity, $\frac{\Delta C}{C}$, has to be increased. This can be achieved by shortening the distance between the two capacitor plates, the inner conductor and the tuner plate. An attached metal piece to the tuner plate, as shown in Figure 6.4, increases the cavity sensitivity to roughly $\pm 40kHz$ for a $\pm 2mm$ movement range.

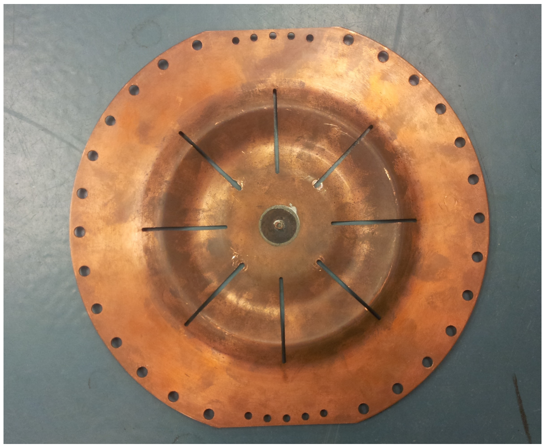

Figure 6.3: Tuner plate

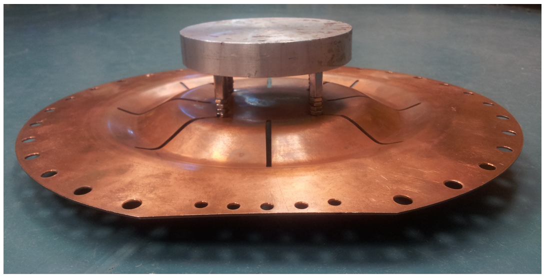

Figure 6.4: Metal piece attached to tuner plate.

The cavity is operated in generator driven mode and the RF input is provided by a frequency synthesizer followed by a power amplifier. The output of the power amplifier is coupled to the cavity through a double wound adjustable coupling loop to achieve critical coupling. To achieve critical coupling, the coupling loop was inserted into the cavity while the reflection coefficient, S11, was measured with a network analyzer. The coupling loop was adjusted to minimize S11 to approximately -28 dB.

A directional coupler (Merrimac CR-10-500, 20 dB directivity) was used to pick up a small portion of the cavity's input. The sampled input signal flows out of the third port of the directional coupler. A second directional coupler was also used to sample the reflected signal. The reflected signal was then passed through a rectifier circuit and a low pass filter (with a cutoff frequency of 100 kHz) which provided input to the motion controller.

A pick-up antenna provides information of the electromagnetic field within the cavity. The output signal of the cavity was fed to a phase detector circuit along with the sampled input signal. A phase shifter was used to compensate the phase shift due to different cable lengths of the input and output signals.

The phase detector circuit obtains the phase lag between the input and output signals of the cavity, which are fed to the motion controller along with the reflected power. The controller sets the speed and direction of the motor to move the tuner plate to a position where the reflected power is minimum.

A single-axis motion controller (DMC-30017, Galil Motion Control, Inc., Rocklin, CA, USA) is used to drive the tuner plate, thus changing the resonance frequency. The developed control schemes are implemented on the 32-bit processor embedded in the motion controller. The program is written using DMC Smart Terminal software in the specific Galil command language. The incorporated motor driver is operated in micro stepping mode, producing 256 micro steps per full step.

A lead screw (Figure 6.5) is connected to the grounded capacitive tuner plate as shown in Fig. 6.3. On the top of the lead screw, two gears are meshed (with a gear ratio of 2.2) connected to the motor. The lead screw converts the rotational movement of the gears into linear movement which moves the tuner plate in and out of the cavity, hence adjusting its natural resonance frequency. The gears are driven by a Slo-Syn synchronous stepping motor model HS50 200 steps/revolution (Superior Electric Co., Bristol, CT, USA). The motor setup and the gear train is shown in Figure 6.5. The described motor setup has a resolution of roughly 47Hz per step. The motor setup is connected to the tuner plate on the top of the cavity, as shown in Figure 6.6.

The rectified reflected power and phase measurements are provided to the ADC of a LabJack T7 DAQ (LabJack Corporation, Lakewood, CO, USA), which is connected to a computer via Ethernet for data acquisition.

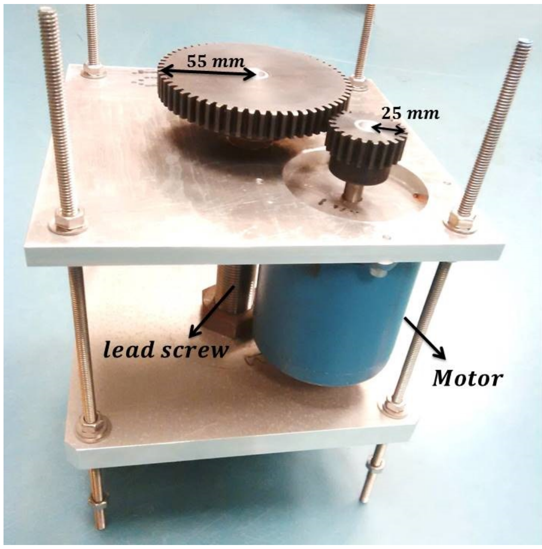

Figure 6.5: Motor setup

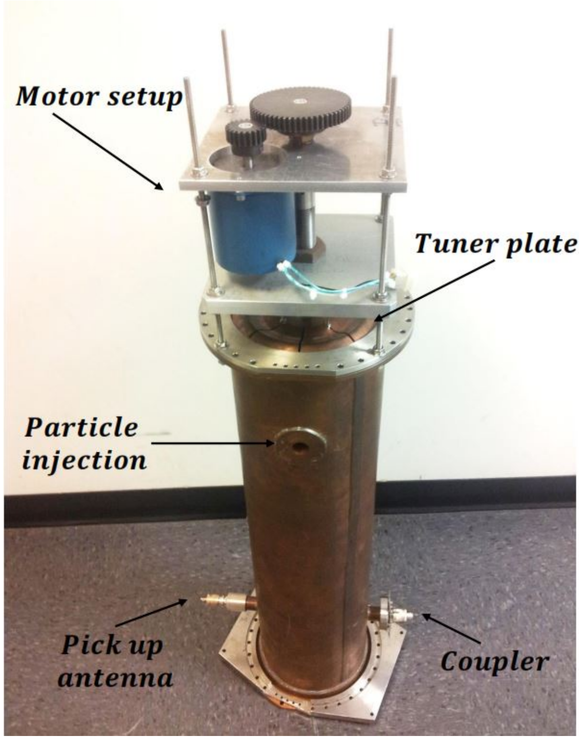

Figure 6.6: Motor setup connected to the cavity resonator

6.2 Test and Measurement Results on the Quarter Wave Test Bench Setup

Test results were obtained using the setup described in section 6.1. Given that the cavity is operated in generator driven mode, the tests were performed such that the driving frequency (provided by the frequency synthesizer) was varied and the resonance frequency of the cavity, tracks the driving frequency. In section 4.3 it was shown that the reflected voltage function is a steeper function compared to the reflected power function, yielding a faster convergence to the optimum operating point, as for both developed control algorithms, the tuner speed is multiplied by the reflected power or voltage. Therefore, the chosen controller input is the measured reflected voltage. Without loss of generality, all system results are plotted in terms of reflected power. The controller parameter for the different control laws are chosen such that the conditions (derived in section 4.3) for stable cavity operation, up to twice the cavity bandwidth, are satisfied.

6.2.1 Experimental Results of the Gradient Based Algorithms

Test 1: Based on Phase Measurement

The first test was performed using control law (4.11), which uses the measured phase as additional controller input and as guidance for the direction of tuner movement. Figure 6.7 shows the measured normalized reflected power and the measured phase versus time. The left arrow shows a change of the driving frequency of $+10kHz$, and the second arrow indicates a change of $-10kHz$. These correspond to a normalized reflected power of roughly 0.5 and positive and negative phase measurement, respectively. The sign of the phase measurement provides the motor movement direction. From Figure 6.7, the tracking time of the resonance frequency of the cavity to the vicinity of zero reflection is obtained ($500ms$). The reflected power converges to zero, indicating that the resonance frequency and the operating frequency are equal and a maximum acceleration field within the cavity achieved.

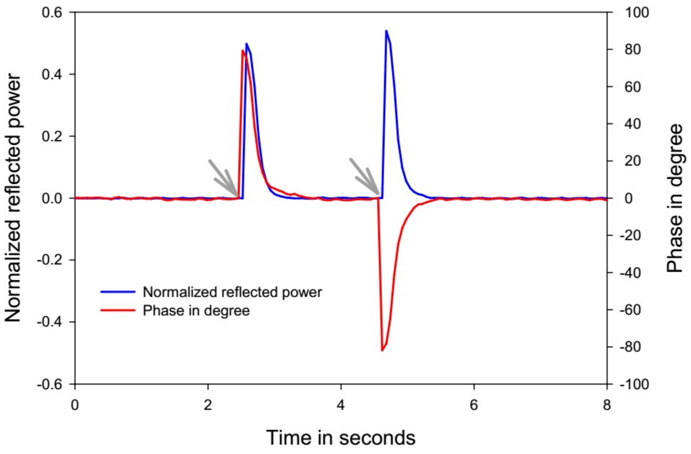

Figure 6.7: Test result using control law (4.11); Measured normalized reflected power and phase in degree versus time.

Test 2: Based on Gradient Estimation

The second test was performed using control law (4.42). The gradient calculation was implemented in the Galil motion controller such that the gradient was re-calculated every $300ms$. It is also only re-calculated for the case where the reflected power increases, meaning that the driving frequency and the resonance frequency are drifting apart. Figure 6.8 shows the measured normalized reflected power and the calculated gradient versus time. After the first driving frequency change (indicated by the first arrow) the reflected power increases and the gradient is recalculated. A change of sign of the gradient results in a motor movement in the right direction and the reflected power decreases. While the first arrow indicates a negative driving frequency change the second arrow indicates a positive change, which is shown by a negative and a positive gradient, respectively. When the reflected power approaches zero, the gradient calculation becomes inaccurate as the signal to noise ratio decreases drastically at the optimum operating point. With respect to the control law (4.42), the motor speed $\dot{\theta}$ is calculated such that the reflected power η is multiplied by the sign of the calculated gradient and the gain. Given that the reflected power approaches zero when perfectly tuned, the inaccuracy of the calculated gradient at optimum tuning can be neglected.

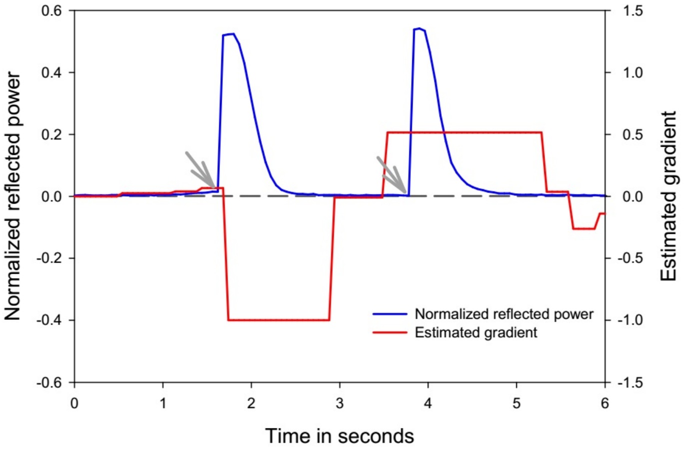

Figure 6.8: Test result using control law (4.42); Measured normalized reflected power and estimated gradient versus time.

Test 3: System Initialization

Figure 6.9 shows the effect of an over or under coupled cavity, explained in section 4.1.3. The cavity is over coupled such that 13% of the power is reflected when the two frequencies match. The initial frequency deviation amounts to $5kHz$. After tracking the driving frequency at about second 1, η does not reach zero. Using solely control law (4.42) results in an oscillation of the resonance frequency around the operating frequency (after the optimum operating point is reached). To eliminate the oscillations, the minimum reflected power η_0 has to be tracked. When η_0 is known, control law (4.43) can be used to to tune the resonance frequency without oscillations.

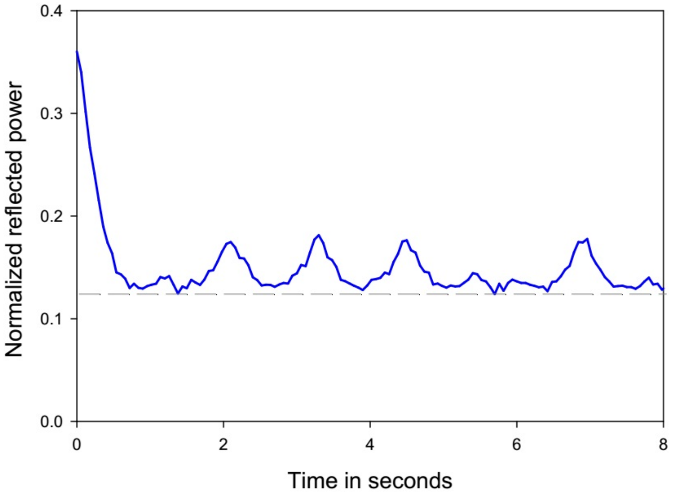

Figure 6.9: Test result using control law (4.42); Measured normalized reflected power versus time for an under coupled cavity.

Figure 6.10 shows the normalized reflected power versus time of a combined system, using control law (4.42) for the initialization phase and (4.43) for the operating phase. The initialization was programmed such that the controller tracked the minimum reflected power value for 3 seconds and substituted the tracked η_0 in control law (4.43) for the operational phase. The test was performed under the same conditions as in Figure 6.9, with a 13% over-coupled cavity and an initial frequency deviation of $5kHz$. As depicted in Figure 6.10, operating the control system in two stages such that the minimum reflected power level is tracked, assures minimal tuner oscillation and best system performance in any case of coupling.

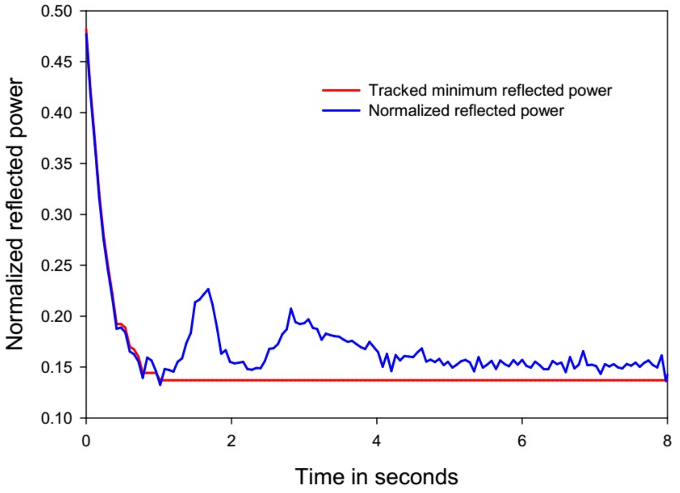

Figure 6.10: Test result using combined control laws (4.42), (4.43); Measured normalized reflected power versus time for an over coupled cavity.

6.2.2 Experimental Results of the Sliding Mode Based Algorithm

The sliding mode extremum seeking control law was developed based on the *Two Time Scale Sliding Mode and System Delays* by Utkin [47], chapter 3. In section 4.2, the control law by Haskara was improved for the purpose of frequency tuning such that the tuner speed $\dot{\theta}$ is multiplied with the reflected power $F(\theta)$. The following test results show the performance difference of the basic algorithm developed by Haskara and the improved control law derived in section 4.2.

Test 1: Sliding Mode Extremum Seeking Algorithm by Haskara

The control law is given by equations (3.9) and (3.10). Figure 6.11 shows the normalized reflected power and the sliding function versus time. The arrows indicate a change of driving frequency of $10kHz$. The plot shows that a sliding mode is reached quickly and the system tracks the new driving frequency. On the sliding mode the function s is '*constant*' and the reflected power decreases with a slope of ρ. Although the convergence speed and the control accuracy can be optimized through controller parameter choice, it is obvious that oscillations around the optimum operating point can not be eliminated since the motor speed is always $\pm k$.

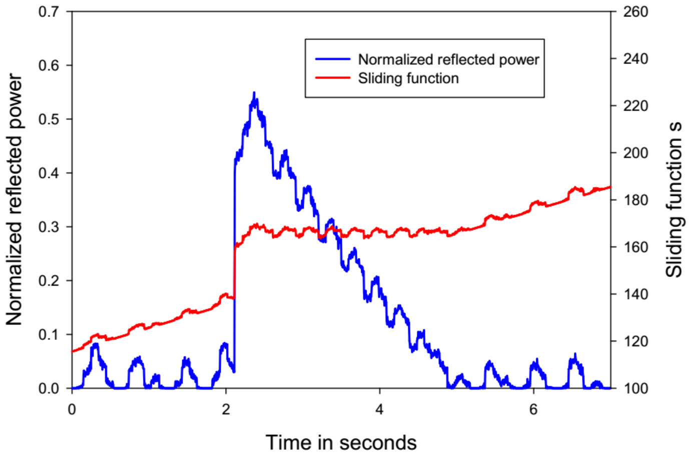

Figure 6.11: Control law Haskara; Measured normalized reflected power and sliding function versus time where.

Test 2: Improved Sliding Mode Extremum Seeking Algorithm

The second test was performed using the improved control law (4.55). Figure 6.12 shows the normalized reflected power, the sliding function s and the motor speed $\dot{\theta} = \pm k_{\theta} F(\theta)$ versus time. The arrow indicates a driving frequency jump of $10kHz$. The system immediately finds a sliding mode. On the sliding mode, the reflected power decreases with the slope of ρ until the sliding mode condition $\left|\frac{\partial F}{\partial \theta}\right| F(\theta) > \frac{\rho}{k_\theta}$ is not satisfied anymore. Then reflected power asymptotically approaches zero as the motor speed approaches zero.

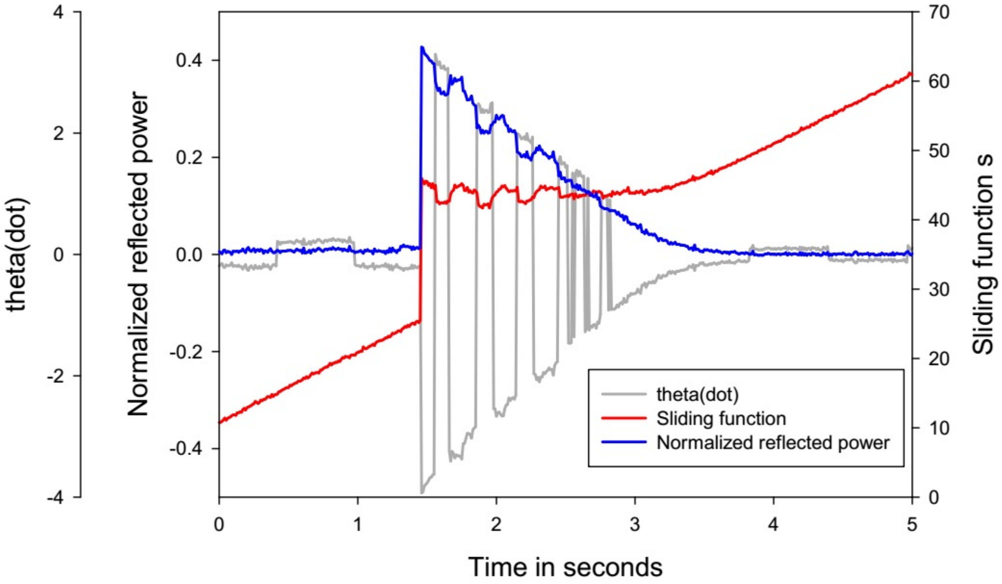

Figure 6.12: Measured normalized reflected power, sliding function, and motor speed versus time using control law (4.55)

.

Test 3: System Initialization

The initialization is done as shown in section 6.2.1 for the same reason of oscillation elimination in case the cavity is not critically coupled. In this case the controller was programmed such that the minimum reflected power $F(\theta)_{min}$ is tracked for 7.5 seconds using control law (4.55). Then, the controller switched automatically to $\dot{\theta} = k_\theta sign\left[sin\left(\frac{\pi s}{\epsilon}\right)\right]\left(F(\theta) - F(\theta)_{min}\right)$ during the operational phase.

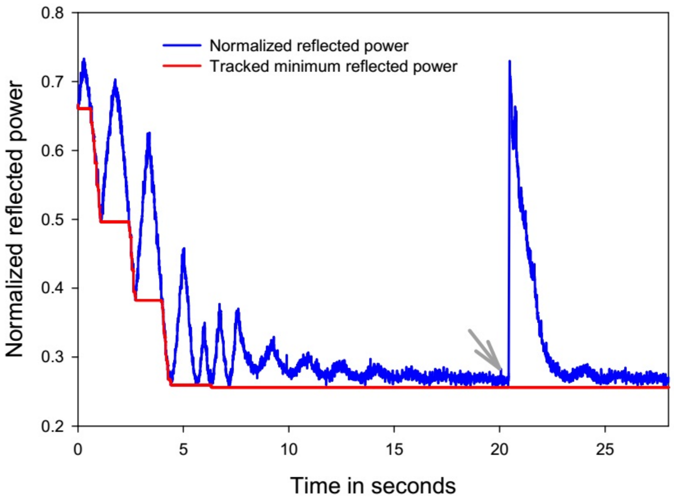

Figure 6.13: Normalized reflected power and tracked minimum power point versus.

At second 20, indicated by the arrow, the driving frequency was changed yielding a measured reflected power jump of roughly 0.7. It can be observed that the new driving frequency is reached quickly within roughly 2 seconds and the oscillation amplitude is approaching zero.

6.2.3 Comparison of System Characteristics of the Gradient Based and Sliding Mode Based Control Algorithms

The system characteristics are defined in terms of accuracy, controllable bandwidth, convergence speed, sensitivity to noise, and necessity of re-initialization. It should be noted that the '*best*' controller variable choice is always a trade off between accuracy and speed. The controller parameters are chosen such that the stable operating conditions (derived in chapter 4) are satisfied and empirically adjusted for best overall performance. Each characteristic is evaluated for both systems under the same conditions and the same controller parameters. Although the results vary slightly for different controller parameters this characterization is intended to give a general comparison.

Accuracy

For a cavity in operation, slow variations of the resonance frequency due to temperature drifts are expected. To simulate a slow drift, the driving frequency was increased by 100Hz per second. Figure 6.14 shows the measured normalized reflected power for the three cases of: tuner switched on using the gradient control law (section 4.1.3), the sliding mode control law (section 4.2) and the third case when the tuner is switched off. It is depicted that the reflected power linearly increases with the frequency deviation. When the tuner is switched on, the normalized reflected power is minimized, independently of the control algorithm.

Regarding the sliding mode based algorithm (blue curve), the wave-form like behavior of the reflected power suggests that the measured reflected power has to reach a threshold value such that the motor speed becomes big enough to actually move the motor, this threshold defines the accuracy and depends on the controller parameter k_θ.

With respect to the gradient based algorithm (red curve), the measured reflected power also shows a wave-form like behavior but not as periodic as for the sliding mode system. This is explained through the gradient calculation and the low signal to noise ratio close to the optimum operating point. Further, to avoid division by zero within the gradient calculation, $\Delta\theta$ is set to 1 if the actual $\Delta\theta = 0$, which can result in the wrong tuner movement direction until the the gradient is recalculated after the time period T. Hence, the accuracy depends on both controller parameters, μ and T.

Comparing the maximum reflected power values, of 0.018 for sliding mode based algorithm and 0.057 for the gradient based algorithm, the accuracy for the sliding mode based algorithm is higher by a factor of ≈ 3.

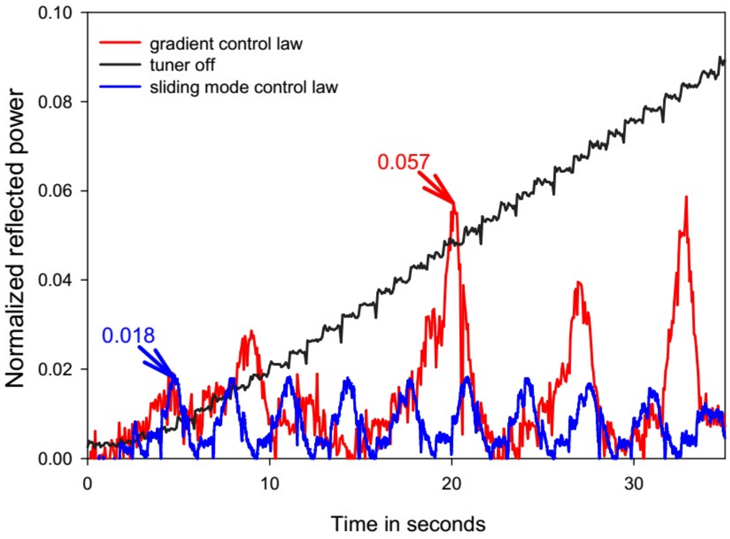

Figure 6.14: Accuracy; Measured normalized reflected power for a slow cavity frequency drift (increase of $100 Hz$ per second)

Controllable Bandwidth

The controller parameters for both developed control laws are chosen such that stable operation up to twice the cavity bandwidth is guaranteed.

Convergence Speed

To obtain a qualitative and comparable result for the convergence speed, the system was at first perfectly tuned and then a frequency jump of $+10 kHz$ was applied to the driving frequency, as indicated as arrows in Figure 6.15 and Figure 6.16. Both systems show a similar convergence time of roughly 2 seconds for a frequency deviation of half the cavity bandwidth.

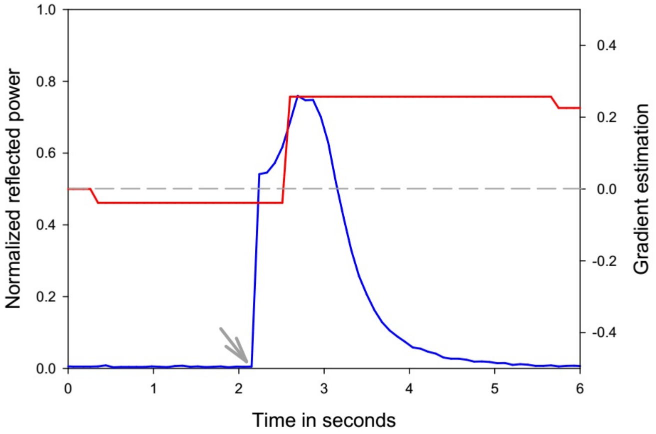

Figure 6.15: Gradient based convergence time test; normalized reflected power and gradient estimation versus time.

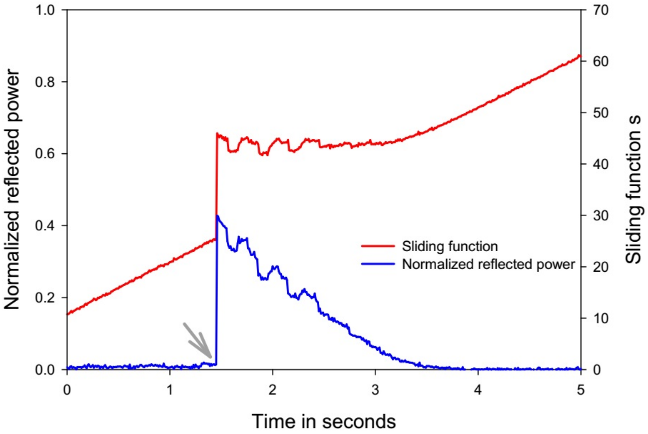

Figure 6.16: Sliding mode based convergence time test; normalized reflected power and sliding function versus time.

Sensitivity to noise

For a cavity in operation, noise can be created by pumps or environmental surroundings creating vibration. To simulate a strong and randomly vibrating environment, we hit the cavity with a hammer while the tuning system was in operation and tracked the driving frequency. Figure 6.17 and Figure 6.18 show the measured normalized reflected power versus time for the gradient based and sliding mode based system, respectively. The arrows indicate changes in the driving frequency. Both system performances are unaffected by the random noise application.

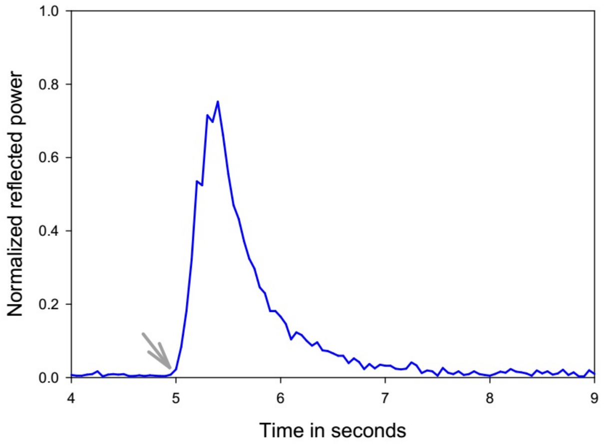

Figure 6.17: Gradient based sensitivity to noise test: Measured normalized reflected versus time.

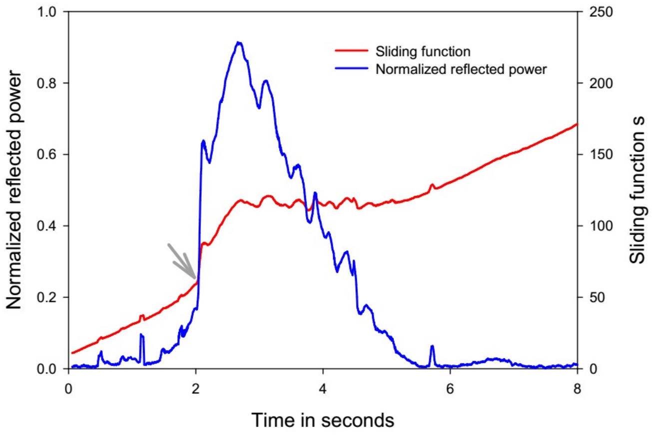

Figure 6.18: Sliding mode based sensitivity to noise test: Measured normalized reflected versus time.

Necessity of re-initialization

Required maintenance work, for example a change of cables, necessitate the RF field to be switched off from time to time. An important feature for frequency tuning systems is the autonomy of the system. In other words, it is of great advantage if a control system can keep running independent of the surroundings such that tuning algorithm does not have to be re-initialized after the RF field is switched off and on. A test for both systems was designed such that the cavity system was perfectly tuned at first, then the RF from the frequency source was switched off for several seconds while the tuning system, the controller, kept running. Before the RF was switched back on, the driving frequency was changed, which is common for cavities in operation as the cavity temperature depends on the RF field.

Figure 6.19 and Figure 6.20 show the test results for both systems, gradient based and sliding mode based, respectively. The results show that both systems run independent of the cavity status.

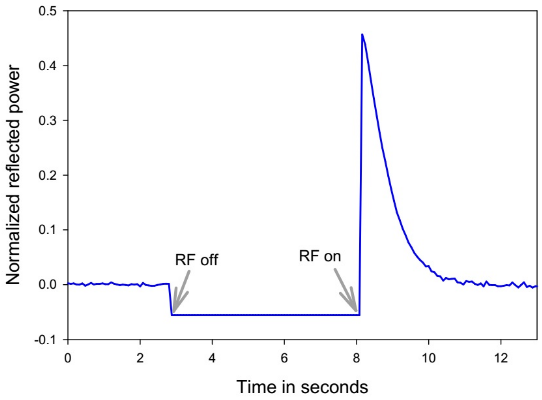

Figure 6.19: Gradient based necessity of re-initialization test; Measured normalized reflected power while RF is switched off and driving frequency is changed.

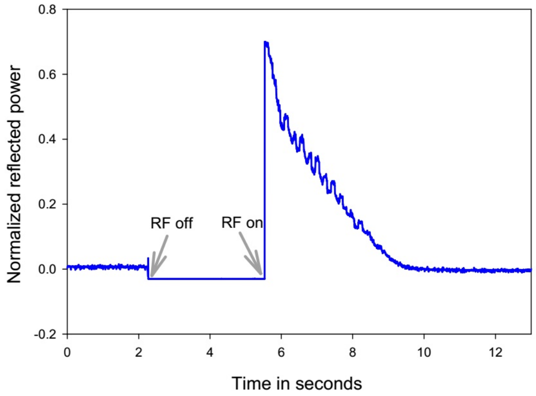

Figure 6.20: Sliding mode based necessity of re-initialization test; Measured normalized reflected power while RF is switched off and driving frequency is changed.

6.2.4 Discussion of the Performance of the Control System

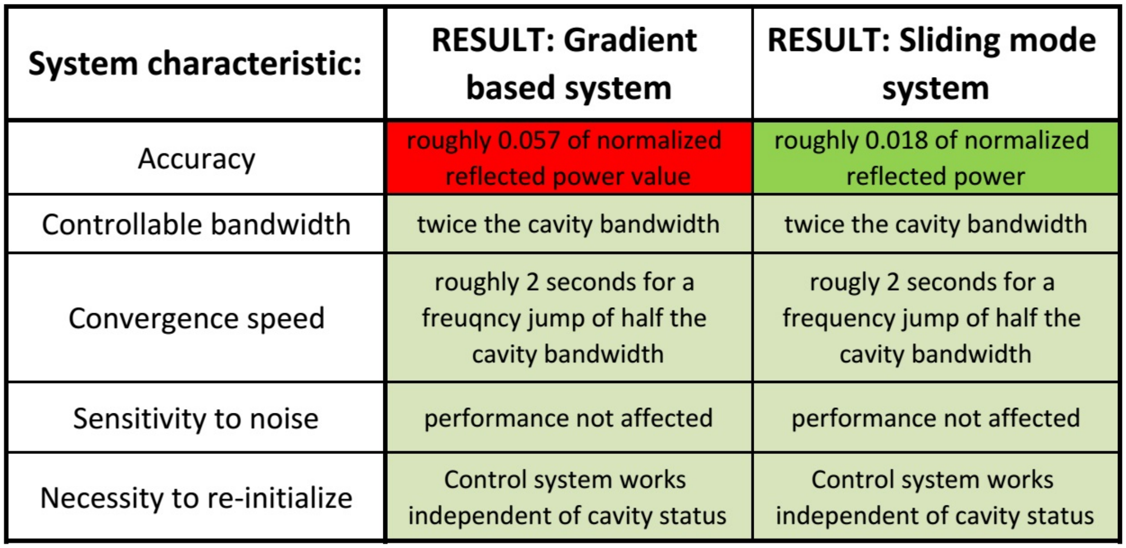

System characteristic:	RESULT: Gradient based system	RESULT: Sliding mode system
Accuracy	roughly 0.057 of normalized reflected power value	roughly 0.018 of normalized reflected power
Controllable bandwidth	twice the cavity bandwidth	twice the cavity bandwidth
Convergence speed	roughly 2 seconds for a freuqncy jump of half the cavity bandwidth	rougly 2 seconds for a frequency jump of half the cavity bandwidth
Sensitivity to noise	performance not affected	performance not affected
Necessity to re-initialize	Control system works independent of cavity status	Control system works independent of cavity status

Figure 6.21: System characteristics of developed gradient based and sliding mode based control laws.

The test results showed that normal conducting cavities can be tuned using solely reflected power measurements, independent of the choice of developed control law. The system characteristics are evaluated and summarized in table Figure 6.21. The light green highlighted boxes represent the same system characteristics. The only performance difference between the gradient and the sliding mode based tuning system is the accuracy. The sliding mode based system shows a better performance in accuracy of a factor of roughly 3, compared to the gradient based system.

As most operational cavities in the world are tuned using the measured phase lag, a comparison between TRIUMF's phase based system and the developed algorithms (based on the reflected power) is of interest.

The phase lag is a linear function in the range of roughly the cavity bandwidth (Figure 1.8). Hence, the system's controllable bandwidth is limited to the cavity bandwidth. The proposed systems, however, reach a controllable bandwidth of twice the cavity bandwidth, also rendering it effective for frequency deviations outside the cavity bandwidth.

A phase comparison system needs a phase shifter to compensate for the phase shift due to the difference in cable-length of the input and output signals of the cavity. For the traditional phase measurement based system, maintenance work such as cable change, or simply long term phase drifts necessitate re- initialization of the control system. However, the reflected power based control system is autonomous and does not have to be re- started when the RF signal is switched off; yielding a more effective system in terms of manual work hours.

The tuning accuracy can not be compared since there are no measurement data of the traditional phase measurement based tuning system available. Nonetheless, the phase measurement is strongly influenced by environmental temperature variations, rendering it inaccurate if the phase set point is not adjusted with respect to the temperature. Reflected power measurements, on the other hand, are insignificantly influenced by temperature changes yielding a more accurate measurement. An example of the temperature influence is presented in section 7.4.

Comparing the system characteristics with the existing linear control system, based on phase lag measurement, yields a better overall performance for the proposed systems using reflected power measurements. Note, the proposed system was tested on a test bench whereas the system characteristic values for the conventional method are empirical values for cavities under operation. Hence, the exact values of the system characteristics have to be verified for a cavity in operation.

Chapter 7

System Commissioning and Performance Measurement on TRIUMF's DTL tank 4 and 5

Within this chapter, the commissioning and performance measurements of the developed resonator frequency tuning system solely depending on reflected power measurement is presented. Based on the measurement results on the quarter wave cavity test bench and the higher accuracy of the sliding mode based control law, the latter was chosen to be implemented on TRIUMF's room temperature drift tube linear accelerator (DTL) tank 4 and tank 5. The chapter starts with an introduction of TRIUMF's DTL and explains how particles are accelerated within such a resonator. Section 7.2 describes the physical setup of the resonance frequency tuning system. Section 7.3.1 and 7.3.2 present the measurement results for tank 5 and tank 4, respectively. It will be shown that the controller parameter have to be chosen with respect to the coupling factor of each individual tank. The influence of environmental temperature changes on room temperature resonators is illustrated in section 7.3.3. The measurement results are discussed in section 7.4.

7.1 Particle Acceleration within a DTL

A drawing of TRIUMF's DTL is shown in Figure 7.1. It consists of 8 RF modules; 5 acceleration structures and 3 bunchers [86]. As the names suggest, the acceleration structures accelerate the traveling particle bunch, while the bunchers' objective is to "re-bunch" the particles as slightly asynchronous particles will drift of the bunch.

Particle acceleration in one DTL tank occurs in a sequence of acceleration gaps. The gaps produce a time varying electric field from the resonant RF voltage. Figure 7.2 shows a cartoon of how particles are accelerated through a DTL. As shown in Figure 7.2(a), the tube parts connected to the upper holder have a positive potential whereas the parts connected

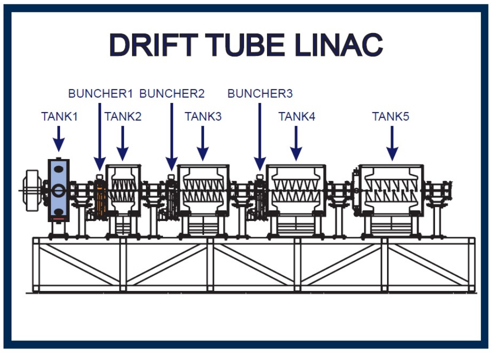

Figure 7.1: Drawing of TRIUMF's DTL.

to the lower holder have a negative potential, resulting a longitudinal acceleration force on the particle bunch. While the particles travel through the separated tube parts the field alternates with the driving frequency. The acceleration of two particles is presented. The blue particle (blue dot) is synchronous with the acceleration field and the red particle (red dot) is slightly asynchronous. From the pictures (a) to (g), the gap between the two particles increases. From Figure 7.2 it is obvious that the resonance frequency of the DTL tank has to be equal to the driving frequency to keep synchronism in following acceleration structures.

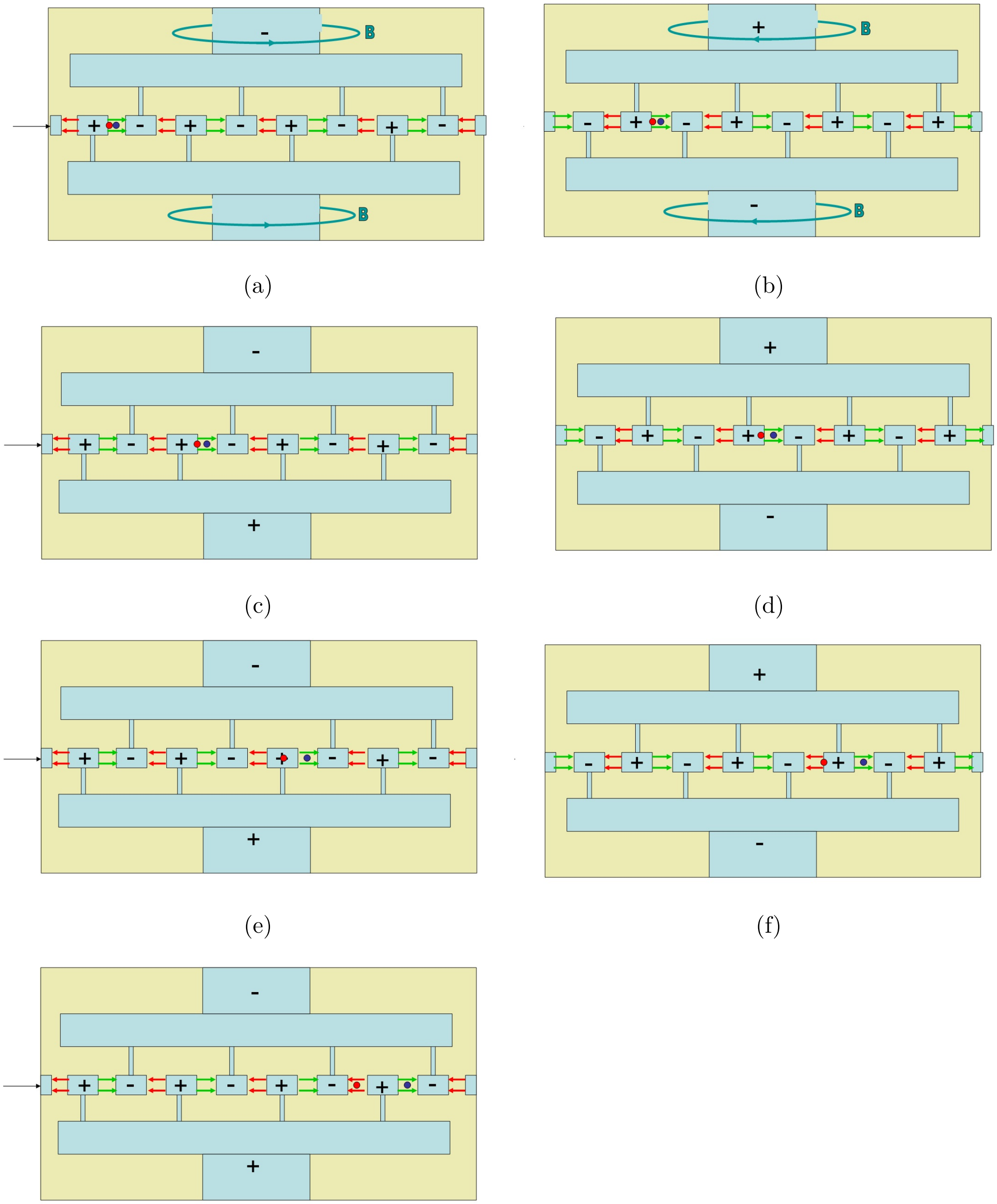

(a)

(b)

(c)

(d)

(e)

(f)

(g)

Figure 7.2: Particle acceleration through a DTL

7.2 Physical Setup of the Tuning System

The physical setup of the tuning system is similar to the quarter wave test bench setup, chapter 6.1. A block diagram of the setup was shown in Figure 6.2. A four-axis motion controller (DMC-2143, Galil Motion Control, Inc., Rocklin, CA, USA) is used as controller board. The control scheme, equation (4.53), (4.55), is implemented on the 32-bit processor embedded in the motion controller. The program is written using DMC Smart Terminal software in the specific Galil command language. Figure 7.3 shows the controller board. The controller is equipped with 4 motor drivers and 8 analog input signals.

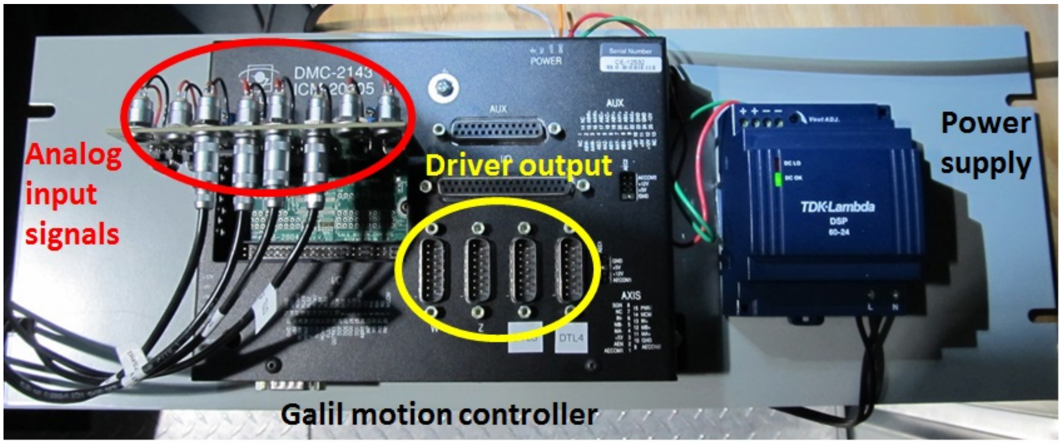

Figure 7.3: Galil Contoller board setup.

The input signals of the controller are internally pulled up to 5V through 4.7 $k\Omega$ resistors. The reflected and forward power signals are $0-10V$ signals with a high output impedance. To match the impedances the controller input signals are buffered through operational amplifiers (CA3140) with unity gain. A printed circuit board was designed, which buffers the input signals and is directly connected to the pin header of the galil controller. A front view picture of the printed circuit board is shown in Figure 7.4, the cavity power signals are connected with LEMO connectors.

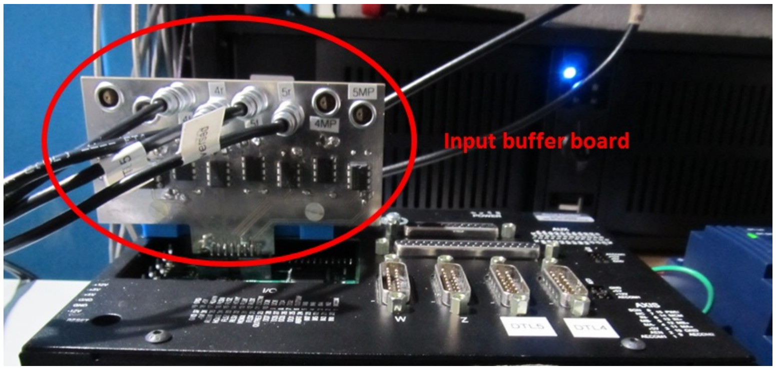

Figure 7.4: Printed circuit board for signal input buffer, front view.

Figure 7.5 shows the back view of the printed circuit board. The blue plastic piece was printed with a 3D printer and mounted to the controller and the input buffer board to assure stable connection to the input header.

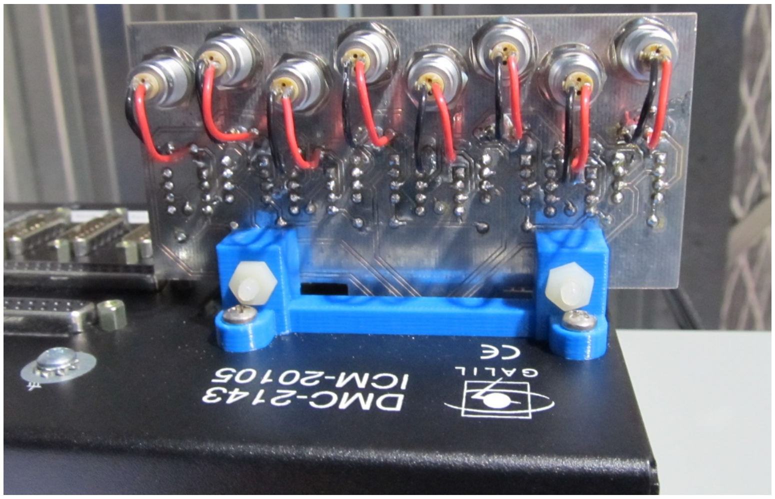

Figure 7.5: Printed circuit board for signal input buffer, back view, and mounting to controller board.

The motor driver output from the controller is directly connected to the stepper motor of both individual DTL tanks. Figure 7.6 shows the copper DTL tank 4 with a connected tuning motor. Figure 7.7 shows the inside of the tuning motor setup, consisting of a stepper motor and a lead screw, which translates the rotational movement into a linear displacement of the tuner plate inside the cavity. The ruler is used to obtain a rough estimate of the cavity sensitivity in terms of resonance frequency shift versus motor position displacement.

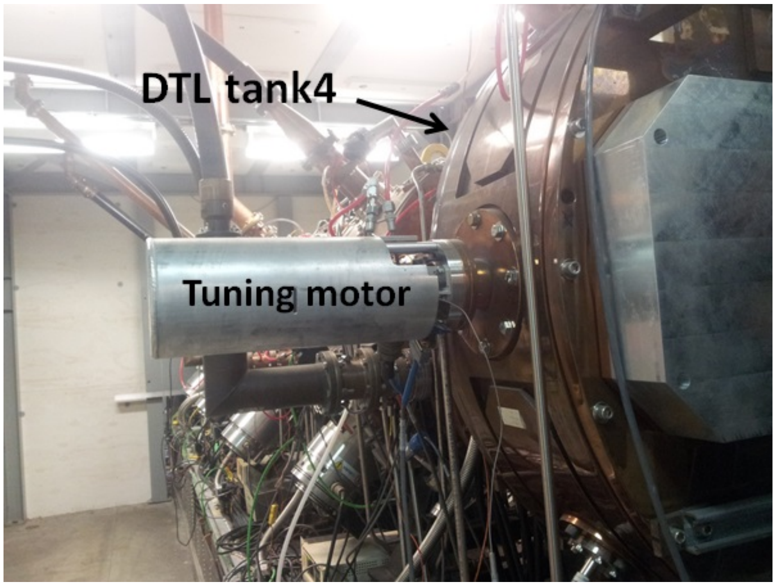

Figure 7.6: DTL tank 4 with connected tuning motor.

,

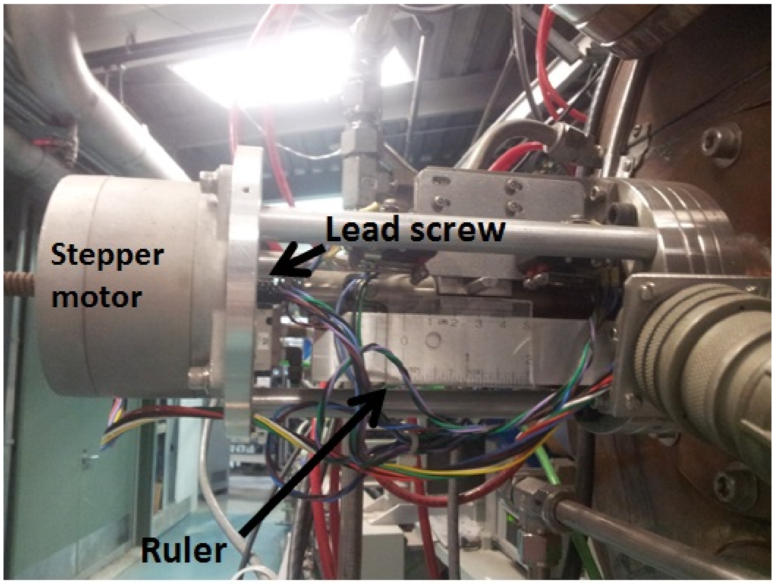

Figure 7.7: Inside view of tuning motor setup.

7.3 DTL Tuning Results

The DTL tuning results are obtained in the same way as for the quarter wave test bench setup. The driving frequency is set to 106 MHz. The cavity is started with low input power and then gradually increased to its desired operation power. The forward power, the reflected power and the readback of the tuner position are monitored.

7.3.1 DTL Tank 5

Figure 7.8 presents the tuning results of tank 5 over the first 500 seconds of operation. The forward power (red line) is increased in steps over the first 400 seconds to the desired power value of roughly 20 kW. It can be observed that with each step of increased input power the reflected power (blue line) increases as well. The effect of increasing reflected power is explained through RF heating. Due to the resistance of the resonator walls, they heat up with increasing input power. This leads to an expansion of the resonator which in turn changes the resonance frequency of the tank. After each step of increased input power the reflected power is driven towards zero as the motor position changes to track the driving frequency while the tanks resonance frequency changes. Shortly before 400 seconds of operation the reflected power reached zero, the input power is at its desired point but the measured reflected power starts to increase while the readback of the tuner position (green line) starts to decrease. The DTL tanks are equipped with a water cooling systems.

As RF heating and water cooling are slow processes it can take several hours until the tank temperature and the connected tuner position are not changing anymore.

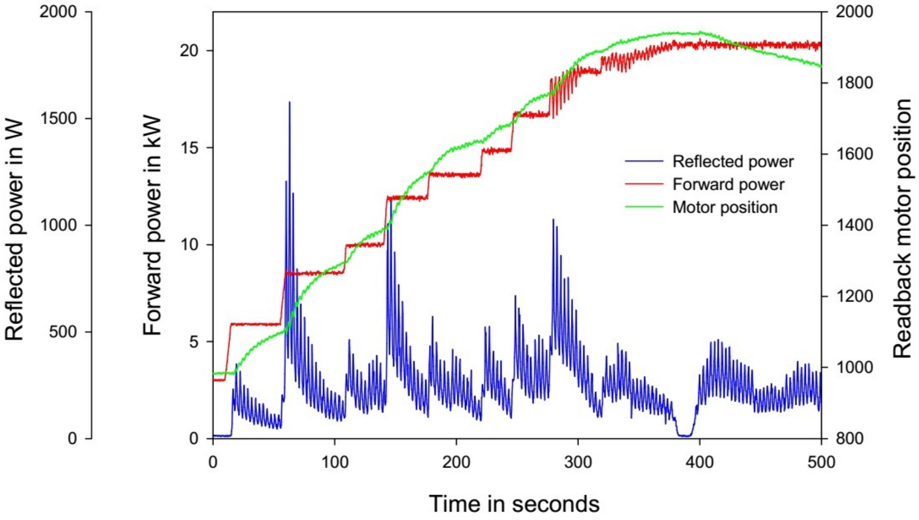

Figure 7.8: DTL tank 5 short term tuning results.

Figure 7.9 shows the monitored reflected power, forward power and tuning motor position over 5 hours of operation. In this case, the forward power was increased to 16kW during the first 10 minutes of operation. The reflected power increases and the tuner position changes as the algorithm minimizes the reflected power and counteracts the temperature induced frequency shift. The plot shows that the RF heating process lasts roughly two hours. When the resonator temperature does not change anymore and the optimum tuning position is reached, the reflected power is minimized and the tuner position stays constant. DTL tank 5 is a great example of an ideally critical coupled resonator as the reflected power decreases to zero when the optimum operating point it reached.

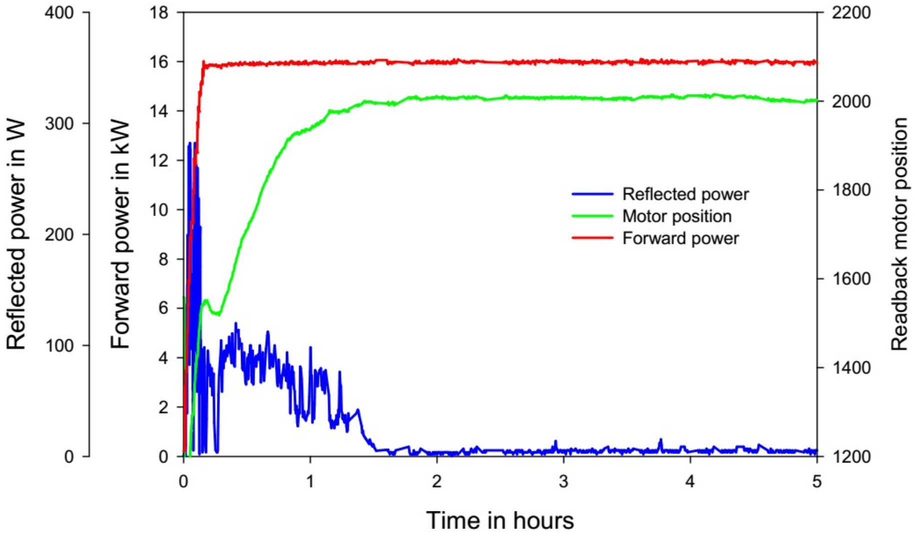

Figure 7.9: DTL tank 5 long term tuning results.

7.3.2 DTL Tank 4

As both tanks have the same resonator characteristics, sensitivity, quality factor, and operating frequency, the controller parameters were chosen to be equal to the ones for tank 5 as well. Figure 7.10 shows a long term measurement of tank 4. It is illustrated that the reflected power does not converge to zero. From multiple measurements on tank 4, it could be concluded that depending on the input power and the accompanied resonator temperature, the coupling factor of the resonator changes. With an input or forward power of roughly 16 kW, the coupling factor changes over the first 4 hours of operation. After the temperature has settled, a minimum reflected power of 500 W is reached, as depicted in Figure 7.10. Since the minimum reflected power does not reach zero, oscillations of the tuner position are shown.

Section 6.2.1 presented the effect of system initialization for over or under coupled cavities on the quarter wave resonator test bench. Since the coupling factor of tank 4 changes over time and also changes with the amount of input power, system initialization is not very effective or the system has to be re-initialized every time the amount of forward power changes. To decrease the oscillation amplitude of the tuning motor movement around the optimum operating point the controller parameter k_θ and ϵ where reduced. Figure 7.11 shows the tuning result for reduced controller parameters k_θ and ϵ. Although the oscillations of the motor movement are not completely eliminated it can be observe that they are reduced significantly.

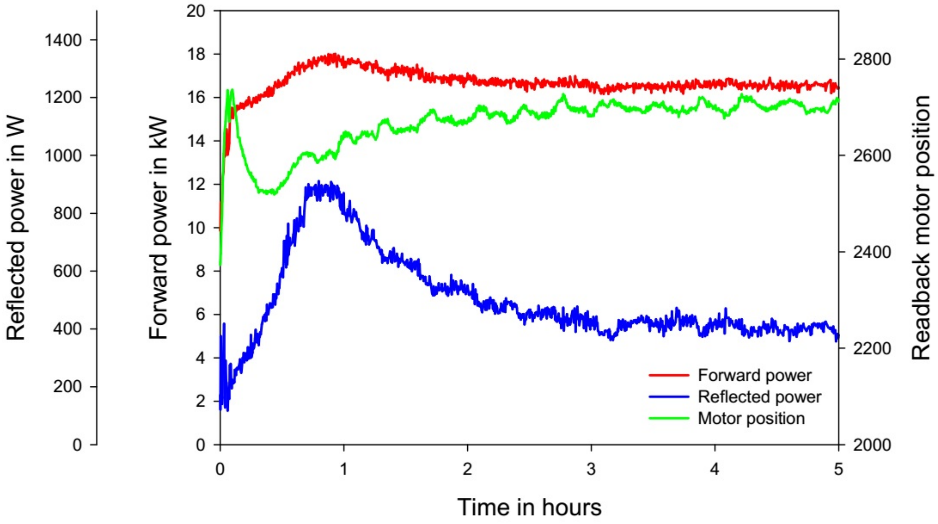

Figure 7.10: DTL tank 4 tuning results, controller parameter are equal to tank 5 tuning parameter.

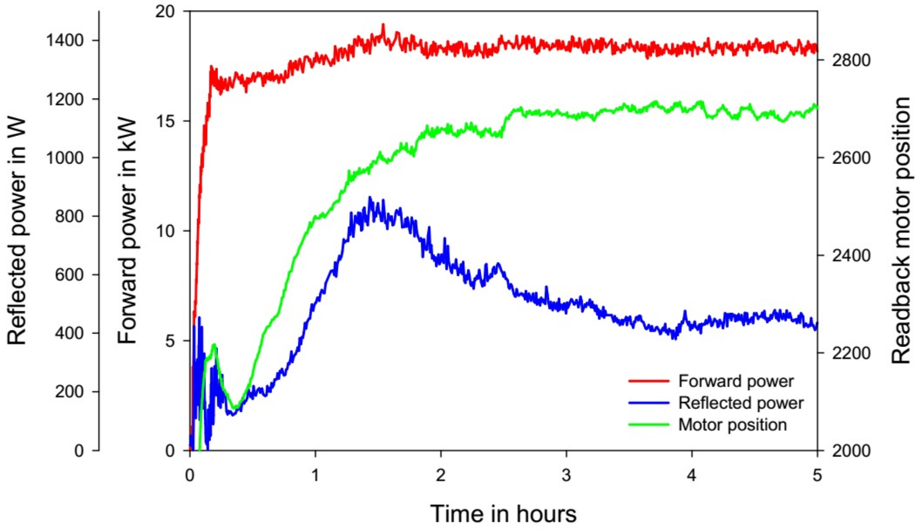

Figure 7.11: DTL tank 4 tuning results with reduced values for the controller parameter k_θ and ϵ.

7.3.3 Environmental Temperature Influence

Figure 7.12 shows the influence of environmental temperature changes on TRIUMF's room temperature DTL tanks. The plot illustrates the forward power, the motor position of tank 5 and the environmental temperature over 35 days of operation. Note, the temperature is measured outside the facility. The resonance frequency is tuned using the sliding mode control approach equations (4.53) and (4.55). From Figure 7.3.3 it can be observed that the motor tuner position varies over the course of a day with respect to the environmental temperature. Figure 7.13 presents a zoomed view of 4 days of operation. The forward power (red line) is increased at day 30 due to different beam requirements for a different experiment. It can be observed that the oscillation amplitude of the tuner movement also depends on the operational power of the cavity. During the first two days (Figure 7.13, day 28-30) tank 5 is operated at constant low power of 8kW. The influence of environmental temperature is shown as low amplitude oscillations with a peak motor position during the hottest time of the day. At day 30, the forward power was increased to 23 kW. Although the environmental temperature variations are equal to the time frame of low power operation, the oscillation amplitude of the tuner position is shown to be greater than at low power operation. These results lead to the conclusion that the water cooling system of the DTL tanks is not sufficient enough to eliminate the environmental temperature variations.

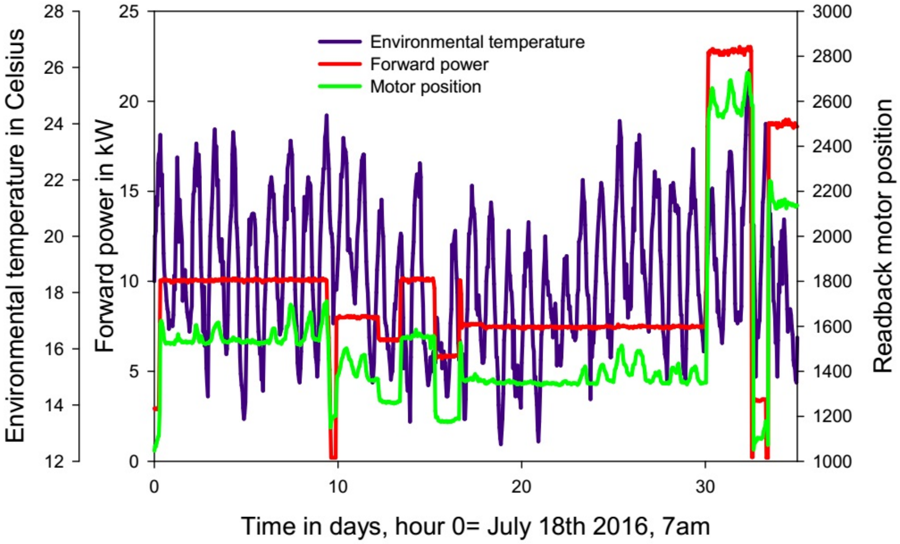

Figure 7.12: Influence of environmental temperature variations on TRIUMF's DTL tank 5.

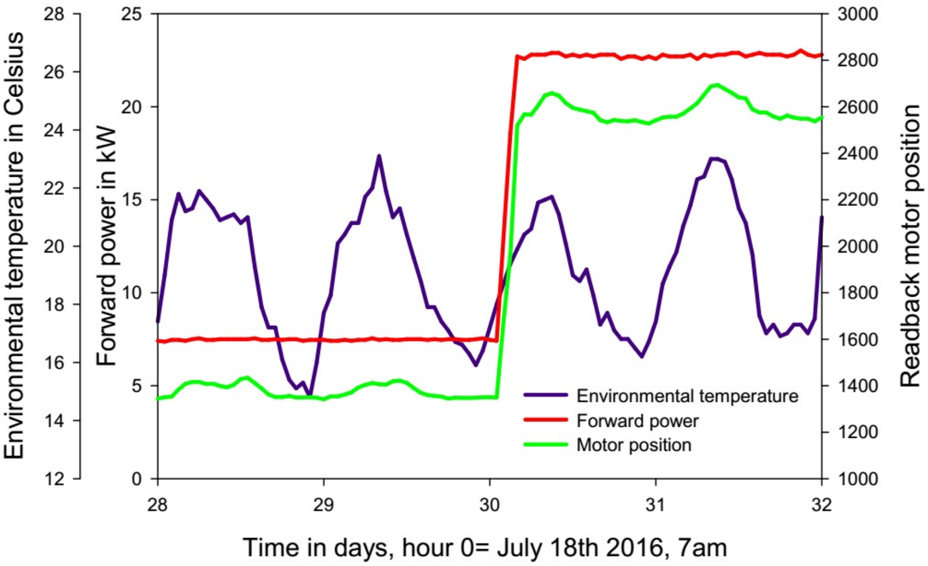

Figure 7.13: Zoom of environmental temperature variations on DTL tank 5 over the course of 4 days.

7.4 Tuning Results Discussion

The results in section 7.3.1 and 7.3.2 showed that the resonance frequency is tuned such that it is equal to the operating frequency as the reflected power reaches its minimum. Resonance frequency drifts caused by RF heating are counteracted. For a critically coupled resonator, oscillations around the optimum operating point are eliminated as the reflected power reaches zero (section 7.3.1). Section 7.3.2 shows the tuning performance for a resonator with a varying coupling factor. Although motor movement oscillations around the optimum operating point are not completely eliminated they were reduced to a minimal amount by adjustment of the controller parameters.

Section 7.3.3 showed the influence of environmental temperature changes on the resonator. The resonance frequency changes caused by environmental temperature variations were counteracted through the tuning system. It is important to note that the environmental temperature variations also affect the signal transportation cables and the signal amplifiers. For a DC signal, as the measured reflected power, the influence of environmental temperature changes is negligible. However, if using the measured (high frequency) phase lag of the resonator as control variable, environmental temperature variations affect the measurement significantly.

The temperature (section 7.3.3) was measured outside the facility. The actual temperature variations, influencing the resonator and the cables, are greater than depicted in Figure 7.12, as the control station is located under the ceiling of the facility. Temperature variations on hot days inside TRIUMF's ISAC I facility are normally in the range of 25°

Celsius with a maximum of 40° Celsius. Czuba and Sikora [3] analysed the temperature stability of different coaxial cables. They measured a phase delay of roughly 9 picoseconds for the coaxial cable MRC200-TCOM of 1 meter length, a temperature difference of $24°C$ (maximum $38°C$) and a signal frequency of $216.6MHz$. The coaxial cable used for signal transportation for TRIUMF's DTL tanks is the MRC200-TCOM cable with a length of roughly 50 meter, from the control station to the tank and back. Assuming that the temperature influence is in the similar range for a $106MHz$ signal, a phase error of roughly 17° can be calculated for TRIUMF's DTL tanks and a temperature variation of $24°C$ between day and night. As the total phase error is the sum of all phase errors within the measurement, the amplifier caused unknown phase error has to be added. The total phase error increases the power requirements and is occasionally out of the limited controllable bandwidth of ±45°, necessitating frequent manual adjust of the phase set point.

As the reflected power measurement is not significantly affected by environmental temperature variations, it increases the accuracy, reduces power requirements as well as the human oversight significantly compared to the traditional phase measurement based frequency tuning system.

Chapter 8

Summary, Conclusions, and Suggestions for Future Work

8.1 Summary and Conclusion

In this thesis, two novel control schemes to tune the resonance frequency of an RF cavity based on reflected power measurements were presented. Most operational cavities are tuned using the phase lag measurement as controller input. The phase measurement accompanied uncertainties and required human oversight motivated the investigation of a control system based on reflected power measurements. Based on the standard model describing the acceleration field of a single mode of an RF cavity (an electromagnetic parallel resonant circuit), an analytical expression for the reflected power function was developed and represents a minimum function. Hence, the resonance frequency tuning problem of an RF cavity could be reformulated as an extremum seeking problem. The key contributions of the present dissertation can be summarized as follows:

- A gradient calculation based extremum seeking tuning approach was developed through the method of Lyapunov stability. A rigorous stability analysis provided conditions for the controller parameters to guarantee stable system operation for frequency deviations up to twice the cavity bandwidth.

- A sliding mode based extremum seeking tuning approach was developed and analyzed. The analysis included three steps: reaching a sliding mode, entering the vicinity of optimum operating point, and parameter determination guaranteeing stable operation of frequency deviations up to twice the cavity bandwidth.

- The developed control laws for resonance frequency tuning were simulated to validate the analytical results. As the simulations were conducted under perfect conditions, it could be concluded that both tuning approaches are suitable for cavities in operation.

- To test both tuning algorithms, a test bench based on a quarter wave room temperature cavity was built. Although the test results showed similar tuning performances for both control approaches, the sliding mode based control law showed a higher tuning accuracy.
- The sliding mode based frequency tuning approach was implemented on two of TRIUMF's room temperature resonators which were commissioned in April 2016. The system performance was monitored and the results were compared to experiences with the traditional phase measurement based tuning system which was used previously.

The outcomes of this dissertation show the advantages of reflected power measurement versus phase measurement based resonance frequency control. A high tuning accuracy, independent of environmental temperature changes, was achieved and human oversight was reduced significantly.

8.2 Suggestions for Future Research

Based on the experience gained and results obtained in the course of this research, the following activities may be considered for future work.

8.2.1 Qualitative Comparison between Reflected Power and Phase Measurement Based Tuning Approaches

Within section 7.4 the monitored tuning results of the commissioned sliding mode extremum seeking system on TRIUMF's DTL were compared to experiences with the phase measurement based system which was previously used. The comparison does not allow an exact comparison in terms of the tuning accuracy. Due to the high demand of beam delivery for different experiments it was not possible to test both tuning systems on the same cavity and under the same conditions.

A qualitative comparison, in terms of the accuracy, is of interested as it allows a conclusion of the required power to operate a cavity. The phase and amplitude tuning system of a cavity assures a stable acceleration field. If the resonance frequency deviates from the operating frequency, the input power is increased to overcome the loss due to impedance mismatch. The reflected power measurement itself is not affected by environmental temperature variations and thus assures a higher accuracy versus phase measurements. To obtain a qualitative comparison in terms of accuracy and required operational power, a study comparing the cavity performance results for both systems under the same conditions should be conducted.

8.2.2 Oscillation Elimination for Resonators with Varying Coupling Factor

In section 7.3.2, tuning results for a cavity with varying coupling factor were presented. Motor tuner oscillations caused by coupling factor variations could be reduced by controller parameter adjustment, yet they could not be eliminated. A coupling factor diverging from 1, critical coupling, increases the amount of reflected power. If the coupling factor is unknown and the sliding mode control algorithm (equations (4.55) and (4.53)) is employed for resonance frequency tuning, oscillations around the optimum operating point depend on the value of minimum power reflection. For cavities with strong coupling factor changes, these motor tuner oscillations can be outside the tolerable range. To minimize coupling factor change induced oscillations, the investigation of a tuning algorithm which incorporates the coupling factor is of interest.

8.2.3 Resonance Frequency Tuning Based on Reflected Power Measurements for Superconducting Cavities

As superconducting cavities become more and more important due to their high quality factors, it is of interest to study if the resonance frequency of those cavities can also be regulated by tuning the reflected power component. Superconducting cavities are normally operated under or over coupled to broaden their bandwidth. The main reason for over or under coupling is the small bandwidth of those cavities. Superconducting cavities are strongly influenced by Lorentz force de-tuning and microphonics. While Lorentz force de-tuning is the main contribution for pulsed machines, microphincs dominate the disturbances for CW machines. Disturbances (resonance frequency fluctuations) caused by microphincs or Lorentz force de-tuning, are often outside the cavity bandwidth. To allow resonance frequency control based on phase measurement and the accompanied small controllable range, the cavities are operated under or over coupled, to minimize resonance frequency fluctuations outside the controllable bandwidth. Superconducting cavities are typically over or under coupled such that roughly 96% of the forward power is reflected.

As presented within this dissertation, the controllable range of a tuning system based on reflected power measurements is increased by a factor of two. For a broader controllable range it can be concluded that the cavity could be operated such that less than 96% are reflected, which in turn lowers the operational costs. The main challenges for such a tuning system are the signal to noise ratio of the reflected power signal and the convergence time of the tuning system. The presented results showed a convergence time of roughly two seconds. Microphonics cause fluctuations in the range of milliseconds which requires a much improved convergence time.

Bibliography

[1] Thomas P Wangler. *RF Linear accelerators.* John Wiley & Sons, 2008.

[2] K Fong, M Laverty, QW Zheng, et al. Adaptive tuner control in triumf isac 2 superconducting linac using kalman filter. In *Proc. Linac*, volume 6, page 592, 2006.

[3] K Czuba and D Sikora. Temperature stability of coaxial cables. *Acta Phys. Pol. A*, 119(EuCARD-PUB-2011-001):553, 2011.

[4] Ramona Leewe, M Moallem, and Ken Fong. System modeling and control of resonance frequency for an rf cavity using reflected power measurements. In *2014 IEEE/ASME International Conference on Advanced Intelligent Mechatronics*, pages 703–708. IEEE, 2014.

[5] AK Mitra, PJ Bricault, IV Bylinskii, K Fong, G Dutto, RE Laxdal, RL Poirier, et al. Rf test and commissioning of the radio frequency structures of the triumf isac i facility. In *Proceedings of LINAC*, page 106, 2002.

[6] RL Poirier, R Baartman, P Bricault, K Fong, S Koscielniak, R Laxdal, AK Mitra, L Root, G Stanford, and D Pearce. Cw performance of the triumf 8 meter long rfq for exotic ions. *arXiv preprint physics/0008210*, 2000.

[7] RE Laxdal, PG Bricault, T Reis, and DV Gorelov. A separated function drift-tube linac for the isac project at triumf. In *Particle Accelerator Conference, 1997. Proceedings of the 1997*, volume 1, pages 1194–1196. IEEE, 1997.

[8] S Simrock. State of the art in rf control. Technical report, 2004.

[9] RA Jameson, TF Turner, and NA Lindsay. Design of the rf phase and amplitude control system for a proton linear accelerator. Technical report, Los Alamos Scientific Lab., Univ. of California, N. Mex., 1965.

[10] Larry R Suelzle. Rf amplitude and phase stabilization for a superconducting linear acclerator by feedback stabilization techniques. Technical report, DTIC Document, 1968.

[11] Jean Roger Delayen. *Phase and amplitude stabilization of superconducting resonators.* PhD thesis, California Institute of Technology, 1978.

[12] T Allison, J Delayen, C Hovater, J Musson, and T Plawski. A digital self excited loop for accelerating cavity field control. In *2007 IEEE Particle Accelerator Conference (PAC)*, pages 2481–2483. IEEE, 2007.

[13] SN Simrock. Achieving phase and amplitude stability in pulsed superconducting cavities. In *Particle Accelerator Conference, 2001. PAC 2001. Proceedings of the 2001*, volume 1, pages 473–477. IEEE, 2001.

[14] D Sauerland, W Hillert, A Roth, M Schedler, and D Teytelman. Amplitude, phase and temperature stabilization of the elsa rf system. In *IPACâĂŹ13 Conf. Proc.(2013)*, volume 2717, 2014.

[15] T Schilcher. Vector sum control of pulsed accelerating fields in lorentz force detuned superconducting cavities. Technical report, DESY, 1998.

[16] Z Fang, T Kobayashi, Y Fukui, K Futatsukawa, S Michizono, S Yamaguchi, S Anami, H Suzuki, F Sato, S Shinozaki, et al. Auto-tuning systems for j-parc linac rf cavities. *Nuclear Instruments and Methods in Physics Research Section A: Accelerators, Spectrometers, Detectors and Associated Equipment*, 767:135–145, 2014.

[17] K Fong, M Laverty, and S Fang. Rf control systems for the triumf isac rf structures. In *Particle Accelerator Conference, 2001. PAC 2001. Proceedings of the 2001*, volume 2, pages 948–950. IEEE, 2001.

[18] Lutz Lilje, Stefan Simrock, Denis Kostin, M Fouaidy, et al. Characteristics of a fast piezo-tuning mechanism for superconducting cavities. In *Proceedings of EPAC*, pages 2256–2258, 2002.

[19] Axel Neumann, Wolfgang Anders, Sascha Klauke, Jens Knobloch, Oliver Kugeler, and Michael Schuster. Characterization of a piezo-based microphonics compensation system at hobicat. *Proc. of the 10th EPAC (2006)*, 2006.

[20] Oliver Kugeler, Axel Neumann, Wolfgang Anders, Jens Knobloch, et al. Measurement and compensation of microphonics in cw-operated tesla-type cavities. In *Proc. of the 41st Advanced ICFA beam dynamics workshop on Energy Recovery Linacs (ERL 2007)*, 2007.

[21] A Neumann, W Anders, O Kugeler, and J Knobloch. Analysis and active compensation of microphonics in continuous wave narrow-bandwidth superconducting cavities. *Physical Review Special Topics-Accelerators and Beams*, 13(8):082001, 2010.

[22] VA Goryashko, V Ziemann, R Yogi, R Ruber, et al. Amplitude and phase control of the accelerating field in the ess spoke cavity. In *Procc. of LINAC12 conf., TUPB107*, 2012.

[23] Kenneth Fong, S Fang, M Laverty, and Q Zheng. Rf control system for isac ii superconducting cavities. In *Particle Accelerator Conference, 2003. PAC 2003. Proceedings of the*, volume 2, pages 1404–1406. IEEE, 2003.

[24] K Fong. New technologies in the design of rf controls for accelerators [c]. In *International Conference on Cyclotrons and Their Applications*, pages 449–454, 2007.

[25] H Imsieke, A Kholdyni, and SN Simrock. Time delay compensation for the digital rf control at the tesla test facility. LINAC, 1988.

[26] Ruben Carcagno, D Orris, T Berenc, Helen Edwards, Leo Bellantoni, and A Rowe. Microphonics detuning compensation in 3.9 ghz superconducting rf cavities. Technical report, 2003.

[27] Harald Klingbeil. Ferrite cavities. *arXiv preprint arXiv:1201.1154*, 2012.

[28] Marinos N Vouvakis, Constantine A Balanis, Craig R Birtcher, and Anastasis C Polycarpou. Ferrite-loaded cavity-backed antennas including nonuniform and nonlinear magnetization effects. *IEEE Transactions on Antennas and Propagation*, 51(5):1000–1010, 2003.

[29] H. Kinley. *The Radioman's Manual of RF devices, Principles and Practices.* Noble Publishing Cooperation, 2004.

[30] Chad Joshi, Bruce Bent, Michael Drury, Joseph Preble, and Viet Nguyen. A magnetostrictive tuning mechanism for srf cavities. In *Particle Accelerator Conference, 1999. Proceedings of the 1999*, volume 2, pages 931–933. IEEE, 1999.

[31] A Mavanur, C-Y Tai, CH Joshi, and T Grimm. Magnetostrictive tuners for srf cavities. In *Particle Accelerator Conference, 2003. PAC 2003. Proceedings of the*, volume 2, pages 1407–1409. IEEE, 2003.

[32] Angelo Bosotti, Carlo Pagani, Nicola Panzeri, Rocco Paparella, Jens Knobloch, Oliver Kugeler, Axel Neumann, Clemens Albrecht, Kay Jensch, Rolf Lange, et al. Full characterization of the piezo blade tuner for superconducting rf cavities. *Proceedings of EPAC08, Genova, Italy*, page 838, 2008.

[33] Ramona Leewe, M Moallem, and K Fong. Control of rf cavity resonance frequency using reflected power measurements. In *Industrial Electronics Society, IECON 2013-39th Annual Conference of the IEEE*, pages 3428–3432. IEEE, 2013.

[34] Ramona Leewe, M Moallem, Ken Fong, and Shahriari. Z. Novel scheme to tune rf cavities using reflected power. In *2016 Linear Particale Accelerator Conference*, 2016.

[35] Stefan Simrock, Wojciech Cichalewski, MK Grecki, GW Jablonski, and WJ Jalmuzna. Universal controller for digital rf control. In *Proc. EPAC 2006*, pages 1459–61, 2006.

[36] Y Tan, WH Moase, C Manzie, D Nešić, and IMY Mareels. Extremum seeking from 1922 to 2010. In *Proceedings of the 29th Chinese control conference*, pages 14–26. IEEE, 2010.

[37] Xiao Li, Yaoyu Li, John E Seem, and Peng Lei. Detection of internal resistance change for photovoltaic arrays using extremum-seeking control mppt signals. *IEEE Transactions on Control Systems Technology*, 24(1):325–333, 2016.

[38] Azad Ghaffari, Miroslav Krstić, and Sridhar Seshagiri. Power optimization for photovoltaic microconverters using multivariable newton-based extremum seeking. *IEEE Transactions on Control Systems Technology*, 22(6):2141–2149, 2014.

[39] Azad Ghaffari, Miroslav Krstić, and Sridhar Seshagiri. Power optimization and control in wind energy conversion systems using extremum seeking. *IEEE Transactions on Control Systems Technology*, 22(5):1684–1695, 2014.

[40] Her-Terng Yau and Chen-Han Wu. Comparison of extremum-seeking control techniques for maximum power point tracking in photovoltaic systems. *Energies*, 4(12):2180–2195, 2011.

[41] Carlos Olalla, Maria Isabel Arteaga, Ramon Leyva, and Abdelali El Aroudi. Analysis and comparison of extremum seeking control techniques. In *IEEE ISIE Conf*, pages 72–6, 2007.

[42] Berk Calli, Wouter Caarls, Pieter Jonker, and Martijn Wisse. Comparison of extremum seeking control algorithms for robotic applications. In *2012 IEEE/RSJ International Conference on Intelligent Robots and Systems*, pages 3195–3202. IEEE, 2012.

[43] Kartik B Ariyur and Miroslav Krstic. *Real-time optimization by extremum-seeking control.* John Wiley & Sons, 2003.

[44] Miroslav Krstić and Hsin-Hsiung Wang. Stability of extremum seeking feedback for general nonlinear dynamic systems. *Automatica*, 36(4):595–601, 2000.

[45] SK Korovin and VI Utkin. Using sliding modes in static optimization and nonlinear programming. *Automatica*, 10(5):525–532, 1974.

[46] Vadim I Utkin. *Sliding modes in control and optimization.* Springer Science & Business Media, 2013.

[47] Vadim Utkin. *Sliding mode estimation and optimization methods in nonlinear control problems.* PhD thesis, The Ohio State University, 1999.

[48] Ibrahim Haskara, Ümit Özgüner, and Jim Winkelman. Extremum control for optimal operating point determination and set point optimization via sliding modes. *Journal of Dynamic Systems, Measurement, and Control*, 122(4):719–724, 2000.

[49] Yaodong Pan, Ümit Özgüner, and Tankut Acarman. Stability and performance improvement of extremum seeking control with sliding mode. *International Journal of Control*, 76(9-10):968–985, 2003.

[50] Hai Yu and Umit Ozguner. Extremum-seeking control via sliding mode with periodic search signals. In *Decision and control, 2002, proceedings of the 41st IEEE conference on*, volume 1, pages 323–328. IEEE, 2002.

[51] Hai Yu and Umit Ozguner. Extremum-seeking control strategy for abs system with time delay. In *Proceedings of the 2002 American Control Conference (IEEE Cat. No. CH37301)*, volume 5, pages 3753–3758. IEEE, 2002.

[52] Arie Levant. Higher-order sliding modes, differentiation and output-feedback control. *International journal of Control*, 76(9-10):924–941, 2003.

[53] Yigeng Huangfu, Salah Laghrouche, Weiguo Liu, and Abdellatif Miraoui. A chattering avoidance sliding mode control for pmsm drive. In *IEEE ICCA 2010.* 2010.

[54] Hai Yu and Umit Ozguner. Smooth extremum-seeking control via second order sliding mode. In *American Control Conference, 2003. Proceedings of the 2003*, volume 4, pages 3248–3253. IEEE, 2003.

[55] Yaodong Pan, Krishna Dev Kumar, and Guangjun Liu. Extremum seeking control with second-order sliding mode. *SIAM Journal on Control and Optimization*, 50(6):3292–3309, 2012.

[56] Arie Levant. Sliding order and sliding accuracy in sliding mode control. *International journal of control*, 58(6):1247–1263, 1993.

[57] Arie Levant. Principles of 2-sliding mode design. *Automatica*, 43(4):576–586, 2007.

[58] Tiago Roux Oliveira, Liu Hsu, and Alessandro Jacoud Peixoto. Output-feedback global tracking for unknown control direction plants with application to extremum-seeking control. *Automatica*, 47(9):2029–2038, 2011.

[59] Tiago Roux Oliveira, Alessandro Jacoud Peixoto, and Liu Hsu. Global real-time optimization by output-feedback extremum-seeking control with sliding modes. *Journal of the Franklin Institute*, 349(4):1397–1415, 2012.

[60] Chun Yin, Brandon Stark, Shou-ming Zhong, and YangQuan Chen. Global extremum seeking control with sliding modes for output-feedback global tracking of nonlinear systems. In *2012 IEEE 51st IEEE Conference on Decision and Control (CDC)*, pages 7113–7118. IEEE, 2012.

[61] Jean-Jacques Slotine and S Shankar Sastry. Tracking control of non-linear systems using sliding surfaces, with application to robot manipulatorsâĂă. *International journal of control*, 38(2):465–492, 1983.

[62] Chun Yin, YangQuan Chen, and Shou-ming Zhong. Fractional-order sliding mode based extremum seeking control of a class of nonlinear systems. *Automatica*, 50(12):3173–3181, 2014.

[63] Lina Fu. *Model-Based Extremum Seeking Control for a Class of Nonlinear Systems*. PhD thesis, The Ohio State University, 2010.

[64] Lina Fu and Umit Ozguner. Variable structure extremum seeking control based on sliding mode gradient estimation for a class of nonlinear systems. In *2009 American control conference*, pages 8–13. IEEE, 2009.

[65] Lina Fu and Ümit Özgüner. Extremum seeking with sliding mode gradient estimation and asymptotic regulation for a class of nonlinear systems. *Automatica*, 47(12):2595–2603, 2011.

[66] Nazmi A Mahmoud and Hassan K Khalil. Asymptotic regulation of minimum phase nonlinear systems using output feedback. *IEEE Transactions on Automatic Control*, 41(10):1402–1412, 1996.

[67] Yuen-Kwok Chin, William C Lin, David M Sidlosky, David S Rule, and Mark S Sparschu. Sliding-mode abs wheel-slip control. In *American Control Conference, 1992*, pages 1–8. IEEE, 1992.

[68] Sergey Drakunov, Umit Ozguner, Peter Dix, and Behrouz Ashrafi. Abs control using optimum search via sliding modes. *IEEE Transactions on Control Systems Technology*, 3(1):79–85, 1995.

[69] Ibrahim Haskara, Ümit Özgüner, and Jim Winkelman. Wheel slip control for antispin acceleration via dynamic spark advance. *Control Engineering Practice*, 8(10):1135–1148, 2000.

[70] Alessandro Jacoud Peixoto, Tiago Roux Oliveira, and Liu Hsu. Periodic switching function based sliding mode control applied to output-feedback extremum-seeking problem. In *2010 11th International Workshop on Variable Structure Systems (VSS)*, pages 124–129. IEEE, 2010.

[71] Ayman A Aly, El-Shafei Zeidan, Ahmed Hamed, Farhan Salem, et al. An antilock-braking systems (abs) control: A technical review. *Intelligent Control and Automation*, 2(03):186, 2011.

[72] Imad Matraji, Fayez S Ahmed, Salah Laghrouche, and Maxime Wack. Extremum seeking control for net power output maximization of a pem fuel cell using second order sliding mode. In *Variable Structure Systems (VSS), 2012 12th International Workshop on*, pages 331–336. IEEE, 2012.

[73] Tinglong Pan, Zhicheng Ji, and Zhenhua Jiang. Maximum power point tracking of wind energy conversion systems based on sliding mode extremum seeking control. In *Energy 2030 Conference, 2008. ENERGY 2008. IEEE*, pages 1–5. IEEE, 2008.

[74] Jui-Ho Chen, Her-Terng Yau, and Weir Hung. Design and study on sliding mode extremum seeking control of the chaos embedded particle swarm optimization for maximum power point tracking in wind power systems. *Energies*, 7(3):1706–1720, 2014.

[75] Her-Terng Yau and Chen-Han Wu. Experimental investigations of mppt in a small scale photovoltaic energy system based on extremum seeking control. *Transactions of the Canadian Society for Mechanical Engineering*, 37(3):1001–1012, 2013.

[76] Her-Terng Yau, Chih-Jer Lin, and Chen-Han Wu. Sliding mode extremum seeking control scheme based on pso for maximum power point tracking in photovoltaic systems. *International Journal of Photoenergy*, 2013, 2013.

[77] Alessandro J Peixoto and Tiago Roux Oliveira. Extremum seeking control via sliding mode and periodic switching function applied to raman optical amplifiers. In *2012 American Control Conference (ACC)*, pages 5377–5382. IEEE, 2012.

[78] Chun Yin, Brandon Stark, YangQuan Chen, and Shou-ming Zhong. Adaptive minimum energy cognitive lighting control: Integer order vs fractional order strategies in sliding mode based extremum seeking. *Mechatronics*, 23(7):863–872, 2013.

[79] Hassan K Khalil and JW Grizzle. *Nonlinear systems*, volume 3. Prentice hall New Jersey, 1996.

[80] Jean-Jacques E Slotine, Weiping Li, et al. *Applied nonlinear control*, volume 199. prentice-Hall Englewood Cliffs, NJ, 1991.

[81] Paul HC Eilers. A perfect smoother. *Analytical chemistry*, 75(14):3631–3636, 2003.

[82] Jin Chen, Per Jönsson, Masayuki Tamura, Zhihui Gu, Bunkei Matsushita, and Lars Eklundh. A simple method for reconstructing a high-quality ndvi time-series data set based on the savitzky–golay filter. *Remote sensing of Environment*, 91(3):332–344, 2004.

[83] H Madden. Comments on smoothing and differentiation of data by simplified least square procedure. *Analytical Chemistry*, 50(9):1383–86, 1978.

[84] Shirin Fartash Toloue and Mehrdad Moallem. A multi-surface sliding-mode extremum seeking controller for alternator maximum power point tracking. In *Industrial Electronics Society, IECON 2015-41st Annual Conference of the IEEE*, pages 001501–001506. IEEE, 2015.

[85] RE Laxdal, K Fong, M Laverty, A Mitra, R Poirier, I Sekachev, and V Zvyagintsev. Recent progress in the superconducting rf program at triumf/isac. *Physica C: Superconductivity*, 441(1):13–20, 2006.

[86] M Marchetto, J Berring, and RE Laxdal. Upgrade of the isac dtl tuning procedure at triumf. *EPAC08, Genoa*, page 3440, 2008.